Germanium on Silicon Near-Infrared Photodetectors

Nonlinear Optics and Optoelectronics Lab

Vito Sorianello

Department of Electronic Engineering

University of Rome 'Roma Tre'

A thesis submitted in partial fulfilment
of the requirements for the degree of

Doctor of Philosophy (PhD)

February 2010

Tutor: Dr. Lorenzo Colace

Coordinator: Prof. Giuseppe Schirripa Spagnolo

Abstract

In recent years, the of Germanium on Silicon approach has been recognized as the best alternative to the well-established III-V technology for the fabrication of high performance near-infrared photodetectors. Recent results demonstrate that Ge heteroepitaxy on Si is by now mature to compete with standard III-V devices. Unfortunately, the integration of Ge-on-Si technology in standard CMOS process flows is still an open challenge due to the sophisticated growth techniques as well as the high thermal budget involved. This work proposes an alternative approach to the growth of Ge on Si for NIR optoelectronics applications.

The first chapter introduces NIR detection for optical communication systems, with particular emphasis on Ge as a suitable material for the monolithic integration into NIR photodetectors on a Si platform.

In the second chapter, the deposition process is described. Ge is deposited on Si by thermal evaporation, a very simple and low temperature ($300°C$) technique suitable for both streamline process and back-end monolithic integration of Ge on Si CMOS electronics. Material characterization, both morphological and electrical, is also discussed. Raman and X-Ray analysis, as well as Transmission Electron Microscopy evidenced that Ge is epitaxially grown in a monocrystalline form with a high dislocation density. Hall measurements demonstrated high unintentional p-type doping ($10^{17} \div 10^{18}$ cm^{-3}) associated to the acceptor-like levels due to the large defect density. The transport and detection properties of evaporated Ge on Si heterojunctions are presented in the third chapter. Results demonstrated a trap-assisted conduction mechanism explained by energy band pinning at the Ge/Si interface. The NIR detection properties were also investigated by illumination at normal incidence. The high doping together with the short diffusion length were found to drastically limit the responsivity of normal

incidence devices.

The last part of this work is dedicated to the design and fabrication of optimized NIR photodetector and their integration on SOI optical chips. Waveguide photodetectors (WPD) were fabricated to take advantage from the distributed absorption of light in guiding structures. WPD exhibit very promising performance with typical responsivities exceeding 0.2 A/W at 1 V reverse bias and 1.55 μm wavelength. These devices were monolithically integrated on SOI optical chips for the realization of channel monitors. The integrated devices exhibit very promising performance, with sensitivity of 10 nW and good linearity over about four orders of magnitude.

Acknowledgements

Contents

List of Figures

1

Introduction

1.1 Near Infrared Detection

Applied research in optoelectronics has invested a lot towards Near Infrared (NIR) light detection. The NIR spectral region covers the range of wavelengths from 750 to 2000 nm and it is of remarkable importance for a large number of applications. From communications to medicine, including remote sensing in satellite applications, as well as environmental and industrial monitoring, researchers from all over the world obtained excellent results in this area. Above all, optical communications represent the workhorse for the development of a high level technology in NIR detection.

The essence of optical communications is the exploitation of light signals for data transfer, allowing low losses, high speed and high data capacity with respect to electric links. The communication channel is represented by the optical fiber, a cylindrical dielectric waveguide made by low-loss materials such as silica glass where light can be confined and guided through 1 Km with attenuation lower than 0.2 dB ($\approx 3.6\%$). The principal limitations to the performance of optical fibers as transmission channel are attenuation and dispersion: the first limits the magnitude of the optical power transmitted, the second limits the transmission data rate by affecting the temporal spreading of the optical signals. These limitations allowed to determine the most suitable wavelengths in the NIR, defining some transmission windows. The first window is at 850 nm, not associated to the above limitations but determined by the first semiconductor sources in Gallium Arsenide (GaAs). The second window at 1.3 μm corresponds to the zero dispersion wavelength as well as to one of the two attenuation minima in

silica glass fibers. The third transmission window, located at 1.55 μm, corresponds to the absolute loss minimum for silica glass fibers. At this wavelength it is possible to design links over one hundred Km with attenuation as low as 0.2 dB/Km. Recently, the demand for high capacity links encouraged the adoption of multiplexing techniques such as the WDM (wavelength division multiplexing), exploiting the whole range of wavelengths between 1.3 and 1.6 μm (S, C and L bands). Fig. 1.1 shows the optical attenuation in silica fibers versus wavelength, the transmission windows as well as S,C and L bands.
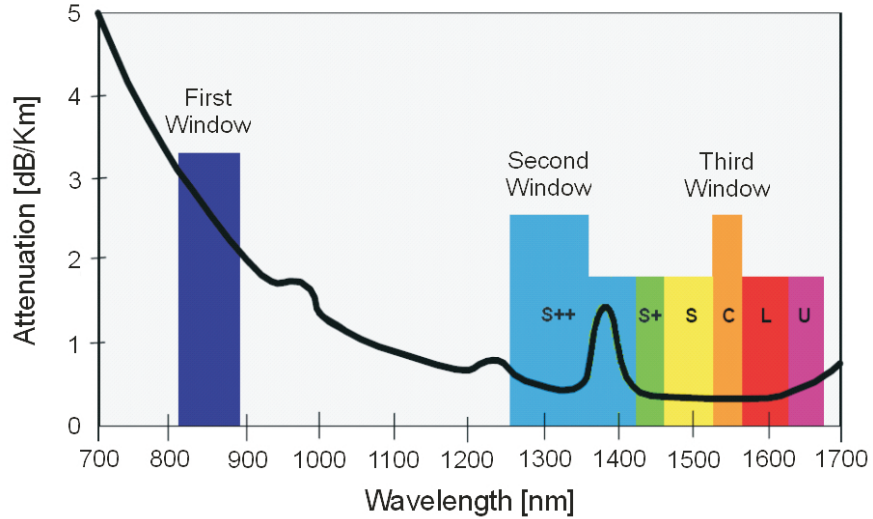
Figure 1.1: Optical attenuation - Optical attenuation in silica fibers with emphasis on the transmission windows and S,C and L bands

Although much effort has been devoted to all-optical communication systems, in optical fiber communications signals are not processed in the optical form, but require conversion to electric signals to be processed by electronics circuitry.

The main subject of this PhD thesis is the conversion of NIR optical signals into electric signals, in particular innovative approaches to integrate low cost photodetectors with standard CMOS electronics as alternative and cheaper viable ways towards commercial solutions for the fabrication of optical transceiver modules.

In the next sections I will briefly summarize the standard techniques for light detection with particular reference to semiconductor photodetectors: basic physics, main figures of merit and limitations. Then, I will focus on NIR photodetectors: suitable

materials for NIR detection, technology and state of the art.

1.1.1 Photodetectors

The basic principle ruling photodetection is the internal photoelectric effect. In a semiconductor material of bandgap E_g illuminated by an optical beam of wavelength λ, if the energy of the incident photons $E_{ph} = hc/\lambda$ (where h is the Plank constant and c the speed of light) exceeds the energy bandgap of the material, one electron is promoted to the conduction band for each photon absorbed. Every time this happens an electron-hole couple is generated and, applying an external electric field, it is possible to collect the photo-carriers in an external circuit and convert the optical into an electric signal.

The main figure of merit indicating how efficiently light is converted in photocurrent is the responsivity R, the ratio between the photocurrent I_{ph} flowing in the photodetector versus the incident optical power P_{in}:

$$R = \frac{I_{ph}}{P_{in}} \tag{1.1}$$

Expressing the photocurrent and the incident light power in terms of the photocarrier generation rate G and the photon flux Φ, we obtain:

$$R = \frac{Gq}{\Phi_{in}h\nu} = \frac{G}{\Phi_{in}}\frac{q\lambda}{hc} = \eta\frac{\lambda}{1.24} \tag{1.2}$$

where q is the electron charge, $\nu = \frac{hc}{\lambda}$ the frequency of the light, η the *quantum efficiency*; λ is expressed in micrometers. The quantum efficiency is an important parameter representing the capability of the photodetector to convert a photon in an electron-hole pair; if η is 1, every single photon generates a carrier pair. If we consider a photoconductor of thickness d, neglecting reflections at the interface, the quantum efficiency can be expressed in function of the absorption coefficient α as:

$$\eta = \eta_c \left(1 - e^{-\alpha d}\right) \tag{1.3}$$

where η_c is the collection efficiency, i.e. the percentage of carriers generated and contributing to the photocurrent; it depends on how defected the material is and generally can be considered close to 1. Fig. 1.2 shows the wavelength dependence of the absorption coefficient in several semiconductors. The bandgap defines the characteristic cutoff wavelength λ_c for each semiconductor, i.e. the wavelength at which the absorption coefficient as well as the responsivity vanish. This parameter determines which materials are suitable for signals satisfying the condition $\lambda < \lambda_c$.
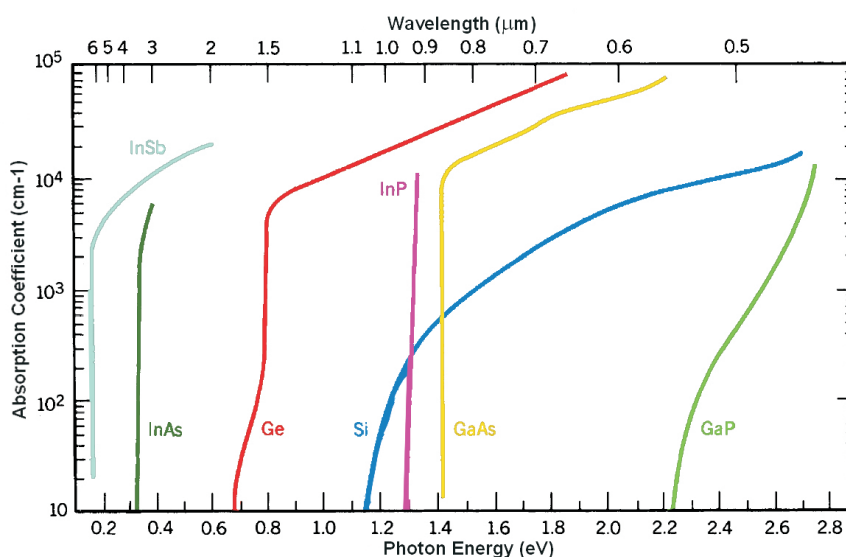
Figure 1.2: Absorption Coefficient - Wavelength dependence of the absorption coefficient in several semiconductors

1.1.2 Junction Photodetectors

In this section I briefly introduce junction photodetectors, suggesting Ref. (1) for more details. The simplest junction photodetector shown in fig. 1.3 consists of a *p-n* diode whose internal electric field is used to collect the photocarriers generated by light. The photocurrent is associated to two fundamental mechanisms: drift and diffusion.

The main contribution is the drift current associated to the carriers generated in the space-charge region. There the generated electrons and holes are swept and transported by the electric field to the neutral regions where they recombine with majority carriers from the electrodes. As the drift current depends on the generation in the

depletion region, applying a reverse bias to the diode helps to increase both the absorption efficiency and the collection efficiency. By consequence the photocurrent in the drift regime increases with reverse voltage.

Photons absorbed in the neutral regions generate photocarriers that partially contribute to the photocurrent. In fact, the absence of electric field allows the generated carriers to recombine without affecting the charge neutrality. Only the photocarriers generated in the proximity of the space charge region can contribute to the photocurrent. Defining the diffusion length $L_{n,p}$ as the average distance covered by an electron (hole) before recombining, if the photocarrier is generated within a diffusion length from the space charge region it can reach it by diffusion and collected by the electric field. This current represents the diffusion contribution to the photocurrent and, as it is not affected by the electric field, it is constant with the reverse bias. The different absorption regions and the associated collection mechanisms (drift and diffusion) are pointed out in fig. 1.3.
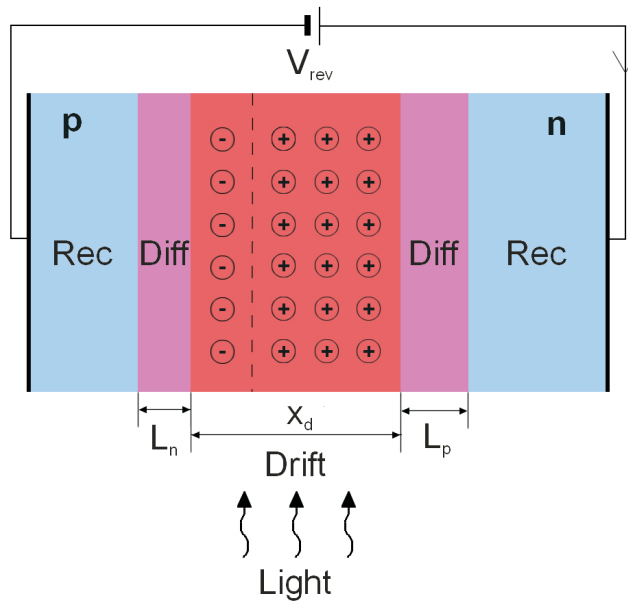
Figure 1.3: p-n junction - Absorption regions in a p-n photodiode. Only photocarriers generated in the depletion region (x_d) and within a diffusion length (L_n, L_p) contribute to the total photocurrent

Although drift and diffusion currents contribute jointly to the opto-electrical con-

version, to design a high performance photodetector it is important to minimize the diffusion current. The detector bandwidth in fact is directly affected by the the detection mechanism: while the drift response depends on the high carrier velocity in the electric field region ($v_{n,p} = \mu_{n,p}E$), the diffusion response is limited by the large diffusion time constants ($\tau_{D_{n,p}} = L_{n,p}^2/D_{n,p}$). Typical diffusion time constants are of the order of microseconds, while the drift time response, known as transit time, depends on the depletion layer width $\tau_{tr} = x_d/v_{n,p}$ if we consider carriers moving at the saturation velocity ($\sim 10^7 cm/s$ for Si). For example, in a 10 μm depletion width the estimated transit time is as low as 100 ps. To minimize the diffusion limitations it is important to increase the drift contribution by properly designing the detector geometry and avoiding generation in the neutral regions.

A simple way to increase the electric field region is to insert a very low doped (intrinsic) layer between p and n regions: the result is the p-i-n geometry. In such structures the depletion regions of p-i and i-n junctions extend entirely in the intrinsic region and result limited by the i-layer thickness w. In these conditions the electric field area is limited to the i region, where it remains almost constant. Therefore, the diffusion limitations on device bandwidth can be overcome when w is properly designed, i.e. if $w >> L_{n,p}$. Fig. 1.4 shows the operation of a normal incidence p-i-n photodetector: the optical power profile as well as the electric field distribution are shown. The active region corresponds to w, i.e. the main design parameter of such devices.In fact, responsivity and bandwidth can be optimized according to:

$$R \propto \left(1 - e^{-\alpha w}\right) \tag{1.4}$$

$$B \propto \frac{1}{\tau_{tr}} = \frac{2V_{rev}\mu^*}{w^2} \tag{1.5}$$

where B is the bandwidth, V_{rev} is the applied reverse bias and μ^* the effective mobility.

While transit and diffusion time rule the intrinsic time response of these devices, it is important to point out that the bandwidth is also limited by the parasitic components determining the extrinsic response.
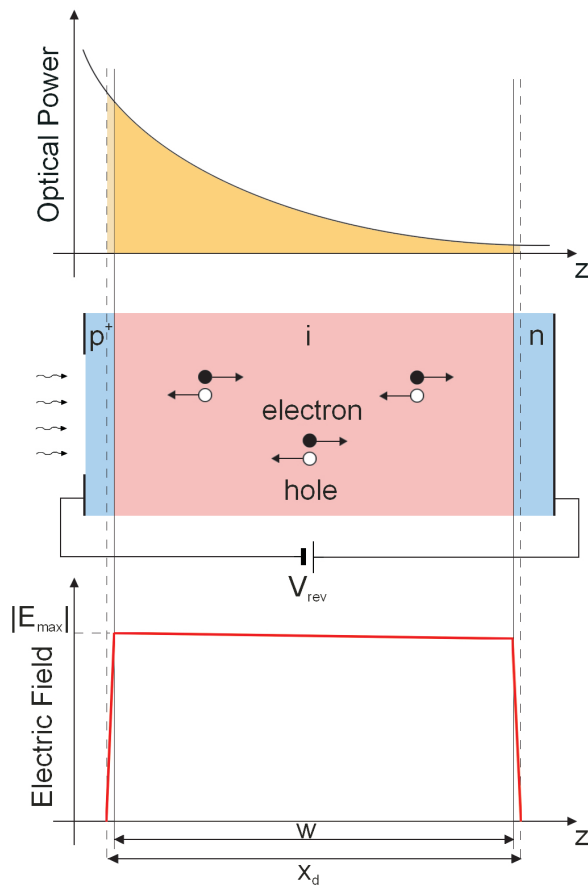
Figure 1.4: p-i-n junction - Illustration of a p-i-n device with optical power and the electric field distribution. Acting on the intrinsic layer width it is possible to optimize the optical absorption and the time response.

Fig. 1.5 shows the equivalent small-signal circuit of a junction photodetector. The photocurrent I_{ph} flows in an equivalent low-pass circuit characterized by a single pole; the latter is due to the diode junction capacitance C_j and the resistor network formed by the shunt resistance R_{sh} and the series resistance R_s. The junction capacitance of a p-n photodiode depends on the space charge region. Referring to the well-known expression for the depletion region width (2):

$$x_d = \sqrt{\frac{2\epsilon_0\epsilon_r}{q}(\frac{1}{N_a} + \frac{1}{N_d})(\phi_b + V_{rev})} \tag{1.6}$$

while ϵ_0 and ϵ_r the vacuum and the relative static permittivities, ϕ_b the junction built-in potential, N_a and N_d the impurity concentrations in p and in n regions, respectively.. The junction capacitance C_j is (per unit area):

$$C_j = \frac{\epsilon_0\epsilon_r}{x_d} = \sqrt{\frac{q\epsilon_0\epsilon_r}{2(\phi_b + V_{rev})}\frac{N_a N_d}{N_a + N_d}} \tag{1.7}$$

For a p-i-n photodiode the capacitance has a simpler expression, mainly dependent on the i-layer width w:

$$C_j = \frac{\epsilon_0\epsilon_r}{w} \tag{1.8}$$

The shunt resistance R_p takes into account the finite value of the derivative $\frac{dI}{dV}$ both in forward and in reverse bias. In fact, even if the ideal inverse current is constant with the applied voltage, actual diodes exhibit non-zero slope dark currents. Moreover, R_p decreases under illumination and can vary with both the signal level I_{ph} and the incident wavelength λ, with a generally high value (1-100 $M\Omega$). The series resistance R_s depends on two main factors: the first is related to the resistance of the neutral regions, the second is the contact resistance of the metal/semiconductor contacts. Since at increasing reverse biases the depletion region widens, the contribution of the neutral regions becomes less important at higher reverse voltages, approaching zero when the punch through condition is reached. Typical values of R_s are of the order of a few Ohms.

The extrinsic response of a photodiode as in the equivalent small signal circuit of fig. 1.5 is characterized by a single pole function with cutoff frequency:

$$f_L = \left(2\pi \left(R_s + R_{load}\right) C_j\right)^{-1} \tag{1.9}$$

where R_{load} is the input resistance of the back-end circuitry. R_p does not appear in eq. 1.9 because is typically negligible with respect to $(R_s + R_{load})$.
p-i-n photodiodes exhibit better performance with respect to the p-n ones. In fact in p-n photodetectors it is very important to properly tune the doping levels to achieve a better trade-off between neutral region resistivity and depletion region width. In p-i-n photodiodes this is less crucial because it is possible to act on p and n doping without affecting the depletion region restricted to the i-layer width.

Hitherto we have dealt with the optimization of the photodiode structure in terms of temporal response without being concerned by the responsivity. Let us consider a normal incidence p-i-n photodiode as in fig. 1.4. From eq. 1.5 and eq. 1.8 we have to minimize w in order to optimize the overall bandwidth; however, if the material absorption at the incident wavelength is not high enough, we could have a fast photodiode with a very low responsivity.
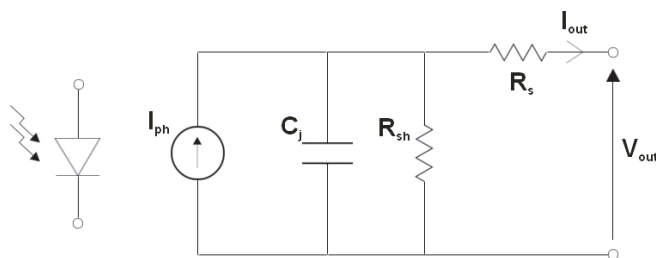
Figure 1.5: Junction photodetector small signal circuit - Equivalent small-signal circuit of a junction photodetector.

Unfortunately, this is unavoidable when photodetectors operate near the absorption cutoff wavelength. In such conditions it would be crucial to treat the photon absorption and the photocarrier collection independently. The solution is represented by distributed absorption in guiding structures where photocarriers are collected normally to the propagation direction. Let us consider a p-i-n structure forming a ridge waveguide with the junction plane parallel to the propagation direction, as in fig. 1.6;

if the wavelength of the propagating wave is shorter than λ_c, the waveguide mode undergoes distributed absorption during propagation in the direction parallel to the junction, with the photogenerated carriers collected normally to it. Properly designing the length of the device it is possible to maximize the responsivity without affecting the bandwidth that depends only on the depletion layer width. Such devices are waveguide photodetectors (WPD).
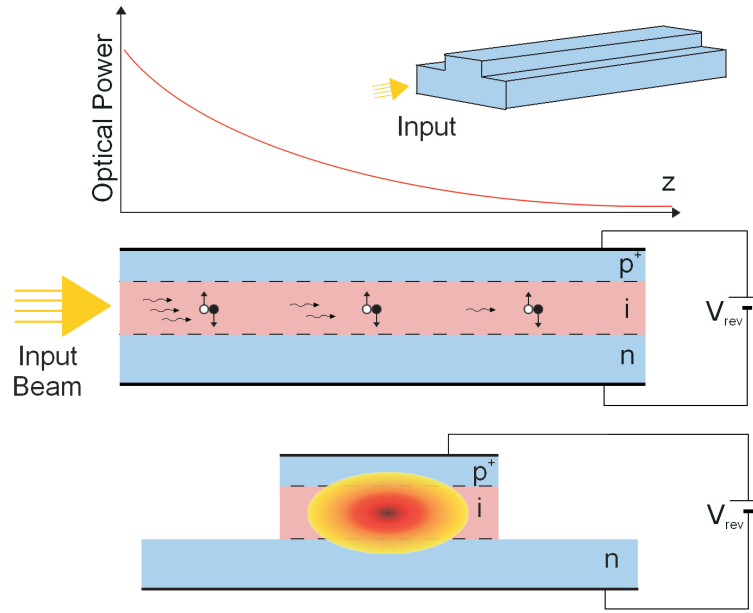
Figure 1.6: Waveguide photodetector - WPD. From the top: the optical power distribution along the waveguide, the side-view and the input cross-section of the WPD.

1.1.3 Heterojunction Photodetectors

A very important aspect of photodetectors is the material used in the fabrication. Homojunction photodetectors are semiconductor devices characterized by only single energy gap E_g. Heterojunction photodetectors are photodiodes with different materials in the junction, i.e. characterized by two different E_g.

The adoption of heterojunction configurations allows more design flexibility and better performance. For example, consider a normal incidence p-n detector in which the top layer has $E_{g1} > E_{g2}$, photons with energy $E_{g1} > h\nu > E_{g2}$ can pass through the top layer without absorption while are absorbed in the bottom material drastically

reducing the diffusion photocurrent from the top neutral region, improving the temporal response. Another important advantage is the possibility to realize photodetectors at certain wavelengths even on substrates not able to absorb in that spectrum. An important example is the object of this thesis, that is the realization of NIR photodetectors on Silicon (Si) substrates, transparent at wavelength longer than 1 μm.

The main technique for the realization of heterostructures is thin film growth on bulk substrates. Even though in principle it could be possible to deposit any material on any semiconductor, a successful heteroepitaxy (in terms of crystal quality) can be accomplished if two materials have the same crystal structure and lattice parameters. With reference to fig. 1.7, consider a substrate of lattice constant a_s and a depositing material of lattice constant $a_d > a_s$.
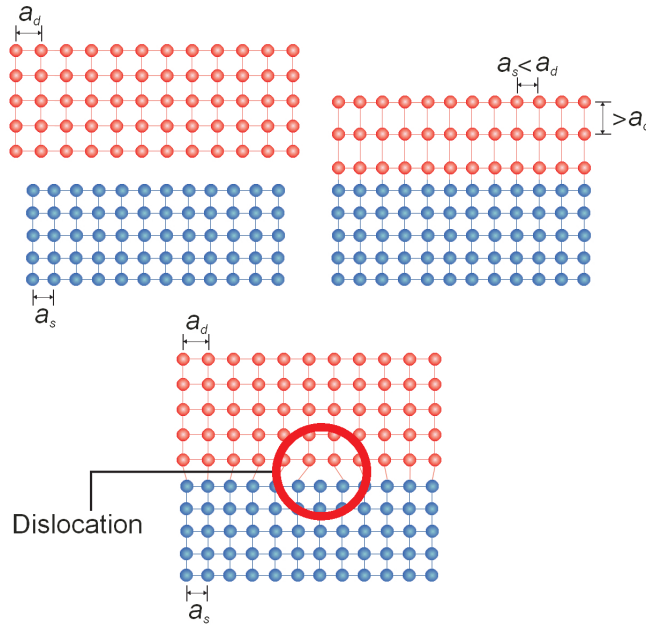
Figure 1.7: Lattice mismatch - A thin film growth on a substrate with different lattice constant first causes the lattice adjustment of the former on the latter with consequent strain accumulation; then, relaxation occurs with the deposited material restoring its own lattice constant and with the formation of defects.

When the deposition starts, atoms find energetically convenient to adjust the lattice through compression in the growth plane and tensile strain along its normal, whereas the substrate remains substantially undistorted. As the growth proceeds further, the

strained lattice tends to relax and the deposited film restores its own lattice spacing.

Relaxation occurs when the energy accumulated by the large strain exceeds the energy associated to the relaxed lattice: this happens when the film exceeds a threshold called "critical thickness" t_c. Relaxation is always associated with the generation of a large amount of defects, both in the growth plane (misfit dislocations) and perpendicularly to it(threading dislocations); their concentration strictly depends on the lattice mismatch. To realize thick epitaxial films with very low dislocation densities it is very important to use materials whose lattice mismatch does not exceed 0.1%. Fig. 1.8 shows the lattice constants of the most relevant semiconductors used for photodetection versus bandgap energy and cutoff wavelength.
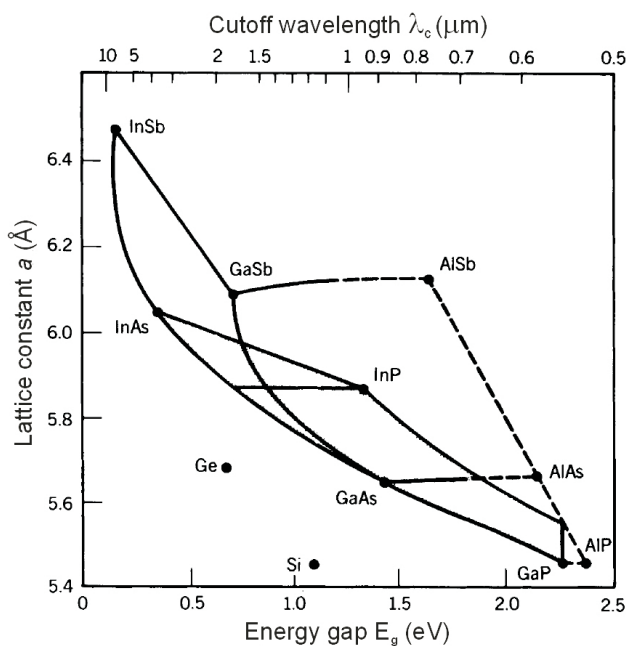
Figure 1.8: Lattice constants - Lattice constants of some semiconductors versus energy bandgap and cutoff wavelength. Dots refer to elementary materials and curves to compounds, where solid and dashed lines indicate direct and indirect bandgap compounds respectively

The main rule for realizing thick films on substrates with mismatched E_g is to move horizontally on the diagram in fig. 1.8 to find the proper material pair. It is important to consider that only few materials are available as substrates, mainly silicon, germanium, gallium arsenide and indium phosphide. Depending on the specific

application it is necessary to choose the less mismatched material to obtain the least defected hetero-epitaxial layer. In fact, the crystalline quality directly affects electric and optical properties of the heterostructure.

Several applications, such as photodetection, do not necessarily require thick films; in these cases we can work with strained layers and tolerate larger lattice mismatches, typically some %. Strain is of particular interest because it is always associated to variations in the electric properties of the material as we will discuss later.

1.2   Materials for Near Infrared Detection

As mentioned before, optical communications represent the main market for NIR light detection with particular emphasis in the range of wavelengths from 1.3 to 1.6 μm. With reference to fig. 1.2, it is apparent that suitable materials for this spectral range are ternary and quaternary compounds based on III-V semiconductors such as Gallium Arsenide (GaAs), Indium Arsenide (InAs) and Indium Phosphide (InP). Alloy such as $In_xGa_{1-x}As_yP_{1-y}$ allow extreme flexibility with variable cutoff wavelengths in the range 1 - 1.8 μm depending on composition. For third-window applications, the best solution is represented by lattice matched $In_xGa_{1-x}As$ on InP heterojunctions with λ_c well above 1.6 μm. III-V photodetectors exhibit high performance in terms of both responsivity and speed; today they dominate the area of NIR photodetection. Unfortunately, the lattice mismatch prevents the deposition of III-V thin films on Si substrates, therefore it is necessary to use the more expensive InP substrates. This incompatibility prevents the monolithic integration of III-V devices with standard Si electronics. Thus, signal processing requires either the monolithic integration of detectors on expensive III-V electronics, or the hybrid integration of III-V devices on Si electronics by means of sophisticated techniques like for example, wafer bonding. Despite the fact that several hybrid optoelectronic integrated circuits (OEICs) were demonstrated, it is believed that monolithic integration on Si would sensibly reduce costs of NIR optoelectronics taking advantage of the well-established Si CMOS technology.

1.2.1   Germanium on Silicon

In the context of optical communications, the common requirement is to reduce the costs of NIR III-V optoelectronic technology, mainly developing Silicon (Si) compatible

technologies (3). As Si is transparent to wavelengths longer than 1.1 μm ($E_g = 1.12$ eV), several solutions have been investigated to integrate NIR absorbing semiconductors with Si in order to realize integrated Si-based NIR systems. The main candidate for Si based NIR photodetectors has been recognized in Germanium (Ge) (4; 5) thanks to its lower bandgap (0.66 eV) with absorption up to 1.6 μm (fig. 1.8). Despite the limitations due to the indirect nature of Ge versus the better performance of III-V compounds, competitive results have been obtained with Ge-on-Si NIR photodetectors, with the significant bonus of a Si-based technology. The first relevant results were reported in 1999 (6; 7) when Ge-on-Si heterojunction photodetectors were fabricated by UHV-CVD with responsivities of 0.55 A/W at 1.32 μm and 0.25 A/W at 1.55 μm and time responses shorter than 850 ps. Further increases in responsivity were demonstrated later (8), with 0.89 A/W and 0.75 A/W at 1.32 μm and 1.55 μm respectively, and 200 ps response time. Improvements in bandwidth up to 12 GHz were obtained by Dosunmu and collaborators (9) by embedding p-i-n photodiodes in resonant cavities; Jutzi $et.$ al (10) fabricated normal incidence Ge-on-Si photodetectors by molecular beam epitaxy (MBE) with responsivity as high as 0.73 A/W at 1.55 μm and a remarkable bandwidth of 39 GHz. Berroth and coworkers (11) recently demonstrated normal-incidence Ge-on-Si p-i-n photodetectors with a record cutoff frequency of 49 GHz at 1.55 μm, even though the dark current density was high (100 mA/cm^2 at 1 V reverse bias) and the responsivity low. Responsivity approaching the theoretical limits were obtained by Yin et $al.$ (12) exploiting guided-wave structures. They demonstrated Ge-on-Si n-i-p waveguide photodetectors with responsivity as high as 1.16 A/W at 1.55 μm (from eq. 1.2 $R_{max} = 1.25$ A/W) operating at 30 GHz. Ge-on-Si avalanche photodetectors were also investigated with remarkable results. In 2009 Kang et $al.$ reported Ge-on-Si avalanche photodetectors operating at 1.3 μm, with an excellent gain-bandwidth product of 340 GHz and a sensitivity as good as -28 dBm at 10 Gb/s (13).

In the next section I will briefly review Ge thin film technology.

1.2.2 Germanium technology

Ge and Si are in the fourth group of the periodic table of the elements; furthermore, the two semiconductors share the same orbitals (four tetragonal sp3 hybrids) and crystal structure (diamond fcc). The lattice mismatch between the two materials is about 4.2

%, large enough to cause strain, relaxation and all the related consequences. Their chemical and structural similarities have suggested to reduce the lattice mismatch by adopting $Si_{1-x}Ge_x$ alloys instead of pure Ge to extend the Si capabilities towards the Ge performance. The first attempt to realize SiGe-on-Si heterostructures was performed in 1975 by Kasper *et al.* (14); they succeded in the realization of the first $Si_{1-x}Ge_x$ thin film on Si by Chemical Vapour Deposition (CVD). Thanks to the development of new techniques such as Molecular Beam Epitaxy (MBE) and Ultra High Vacuum Chemical Vapour Deposition (UHV-CVD), SiGe epitaxy experienced a considerable improvement.

For NIR photodetection it is important to grow films thick enough to provide a quantum efficiency close to 1. With reference to eq. 1.3, fig. 1.9 plots the factor $(1 - e^{-\alpha d})$ as a function of the film thickness d for some values of α between 1 and 10^5 cm^{-1}, a typical range of values for semiconductor materials in the NIR spectrum.
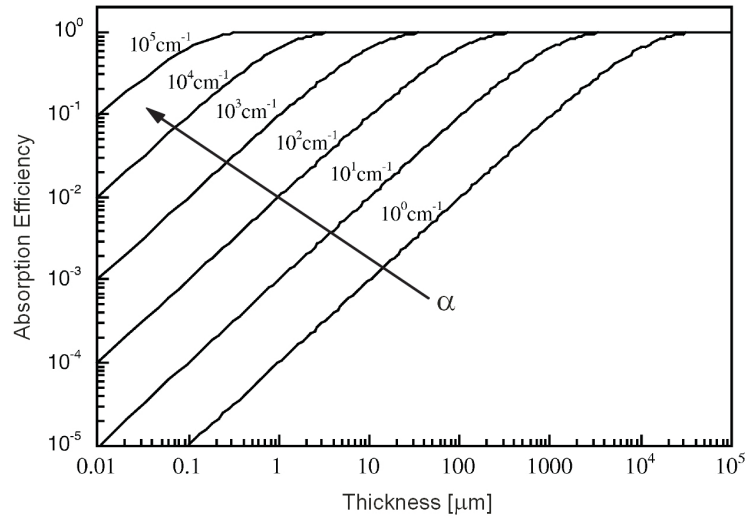
Figure 1.9: Absorption efficiency - Absorption efficiency $(1 - e^{-\alpha d})$ versus absorbing thickness for increasing absorption coefficient α

The absorption efficiency is equal to unity for a minimum extension of the active layer of 300 nm, corresponding to an absorption coefficient of 10^5 cm^{-1}. Comparing the plot of fig. 1.9 with fig. 1.10, which shows the absorption coefficient of bulk SiGe alloys for various Ge contents, the unity absorption efficiency is satisfied by pure Ge at wavelengths below 800 nm and shorter for SiGe alloys. If we consider wavelengths

longer than 1300 nm, the absorption coefficient decreases to 10^4 cm^{-1} and a unitary absorption efficiency can be achieved with 3 μm of pure Ge or more for SiGe alloys. Fig. 1.11 shows the critical thickness for SiGe epilayers versus Ge content. In order to obtain strained SiGe films below the critical thickness but above 300 nm we need to work with SiGe alloys with Ge content below 20 %. Unfortunately, from fig. 1.10 it is clear that this constraint does not allow to use such strained alloys for fiber optic communication purposes.
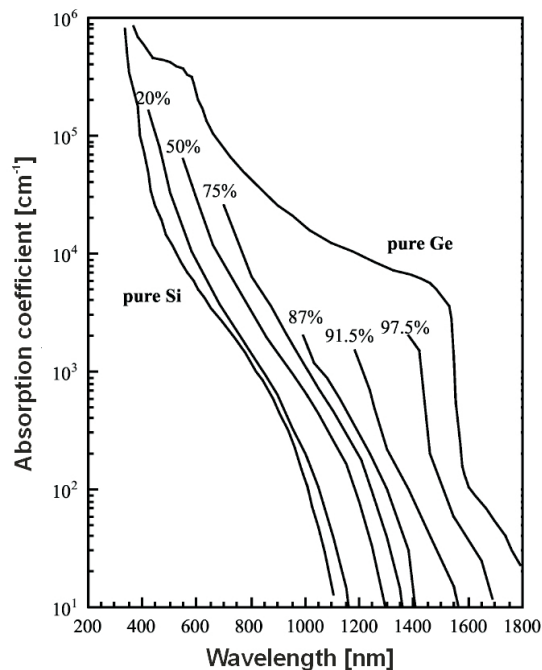
Figure 1.10: SiGe absorption coefficient - Absorption coefficient versus wavelength for $Si_{1-x}Ge_x$ bulk alloys with different Ge content (pure Ge and Si (2), 25-50-75% (15), 87-91.5-97.5% (16)).

Great effort has been invested in growing relaxed pure-Ge thin films to take full advantage of the Ge properties. The first attempts date back to 1968, when Ito and Takahashi demonstrated the epitaxial growth of Ge layers on Si substrates by vacuum evaporation (17). Another attempt consisted in growing an amorphous Ge film on Si in high vacuum at room temperature, followed by re-crystallization annealing at temperatures above $650°C$ (18). The same researchers were able to obtain similar results without recrystallization by a proper choice of substrate temperature (19). Kuech and co-workers demonstrated the heteroepitaxial growth of Ge-on-Si by simple CVD (20)

and performed a comparison between epilayers grown by CVD and by physical vapor deposition (PVD) (21). PVD was carried out in high vacuum on substrates heated up to $500°C$, while CVD layers were grown at atmospheric pressure with substrate temperatures in the $500/900°C$ range. The best films had analogous characteristics with a minimum dislocation density of $4 \cdot 10^9 \ cm^{-2}$. The resultant Ge films were highly p-doped in all cases, with concentrations above $10^{18} \ cm^{-3}$ and resistivities close to 10^{-2} Ωcm.
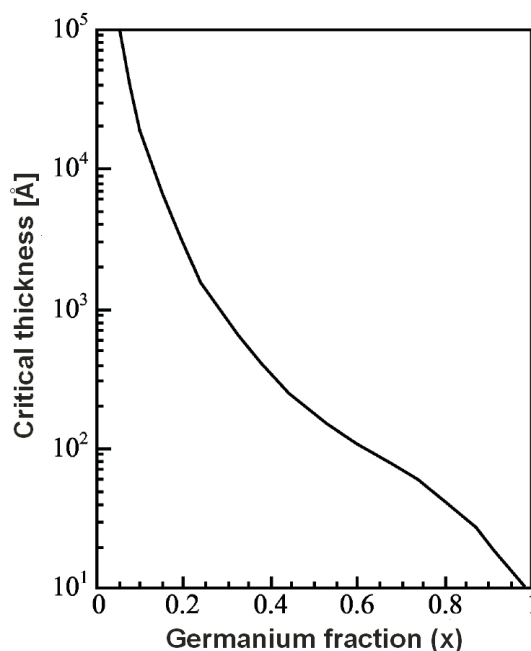
Figure 1.11: SiGe critical thickness - Critical thickness of a $Si_{1-x}Ge_x$/Si epilayer versus x (22)

The average Hall mobility increased with layer thickness from 100 to 300 $cm^2/(Vs)$, whereas the hole concentration remained constant. Remarkable improvements in crystal quality were obtained with MBE and UHV-CVD. In 1988 Baribeau *et al.* reported one of the first MBE grown pure-Ge epilayers, succeeding in lowering the threading dislocation densities to $10^7 - 10^8 \ cm^{-2}$ (23); a few years later Cunningham *et al.* reported the first UHV-CVD epitaxial growth of pure Ge on Si (24).

Recently, UHV-CVD has been the most widespread growth technique for pure-Ge, especially for optoelectronic purposes thanks to the advantage of *in-situ* doping allowing to directly realize *p-n* or *p-i-n* heterostructures. Nevertheless, the main limitation of Ge

in device applications remains the high threading dislocation density of relaxed films. In the last decades several groups focused their attention to minimizing the dislocation density. The adoption of techniques such as graded SiGe buffers (25), low-temperature thin Ge layers (26), buffers combined with thermal annealing (6) and virtual substrates (27), have permitted to lower the threading dislocation density of Ge thin films from 10^9 cm^{-2} of the first direct growth (20) to the last record of about $5 \cdot 10^5$ cm^{-2} (28).

Despite the remarkable successes obtained in both high quality crystal growth and device technology, the integration of Ge on Si technology with standard VLSI process flows is still complex and hardly feasible. The main reason is the sophisticated techniques as well as the high thermal budget required to obtain low-defect Ge layers. At the moment, only two groups have demonstrated a full monolithic integration of Ge-on-Si NIR-detectors with standard Si electronics adopting two different approaches. The first example was reported by our group: we demonstrated a NIR digital camera consisting of an array of Ge-on-Si photodetectors integrated with standard CMOS electronics for analog and digital signal processing. We deposited Ge thin films by low temperature PVD on the pre-existing Si electronics, demonstrating the feasibility of a low cost and low impact technology for the integration of Ge optoelectronics with Si electronics (29). The second example, demonstrated by Luxtera Inc., is a monolithic optical receiver at 1.55 μm operating at 10 $Gbit/s$ and based on single-crystal Ge waveguide photodetectors, with responsivity of 0.6 A/W and dark current of 10 μA at 1 V reverse bias. The receiver is fabricated by a low-temperature CVD growth of Ge, in-line with the standard Si process flow of a 130 nm CMOS foundry (30).

I focused my attention on Ge growth by thermal evaporation. The aim of this work is to investigate the properties of evaporated Ge and demonstrate monolithic integration of Ge NIR photodectors on Si chips by means of a simple and low-cost technology. This dissertation is organized in three main sections. In the next chapter I will present the growth technique and an accurate characterization of structural and electrical material properties. In the third chapter I will discuss the fabrication and characterization of simple pn Ge-on-Si heterojunctions, with particular emphasis on the conduction mechanisms at the heterointerface. In chapter four I will describe Ge-on-Si waveguide NIR detectors fabricated on Silicon on Insulator (SOI) substrates. I will demonstrate the realization and characterization of stand-alone photodectors and their integration on SOI optical chips for channel monitor applications. In the last section of chapter four, I

will discuss the effective monolithic integration of Ge-on-Si power monitors on Si-based optical chips. The performance of such devices is very promising and confirms the feasibility of this technique for monolithic integration with the standard Si technology.

2

Growth and Characterization of Germanium thin films

Many researchers have succeeded in growing low-defect, high quality Ge-on-Si heterostructures. Nevertheless, high quality Ge layers require sophisticated techniques hardly compatible with the standard process flow of Si CMOS technology. In my research I have been mainly interested in the development of PVD of Ge as a suitable alternative to UHV-CVD and MBE towards monolithic integration on Si platforms.

In this chapter I introduce thermal evaporation of Ge carried at low temperature on Si substrates. The morphological properties of evaporated Ge thin films were studied by Raman and X-Ray spectroscopy versus growth parameters; by Hall measurements we could analyze the majority carrier type, the equivalent doping density as well as resistivity and mobility.

2.1 Growth Technique

Physical Vapor Deposition, or simply PVD, consists in transferring atoms from a solid or molten source to a substrate. The main characteristic of PVD is the *physical* mechanisms by which atoms enter the gas phase before deposition, without any chemical reaction (with the exception of reactive PVD processes). PVD can be accomplished by two main mechanisms: *thermal evaporation*, whereby the source material is heated at temperatures at which it either evaporates or sublimates; *sputtering*, where the material is bombarded at room temperature by gaseous heavy ions producing the ejection of

atoms. In this work I will focus on thermal evaporation. For more information about sputtering please refer to more exhaustive publications (31).

Thermal evaporation dates back to 1857, when Faraday experimented on the first thin film deposition (32). Progress in vacuum pumping systems as well as the development of stable heating sources gave rise to a steady improvement in thermal evaporation, so that nowadays it is widespread for the deposition of optical thin films, as well as large-area coatings for numerous applications. This deposition process consists of vaporising a solid material and recondensing it onto a cooler substrate. Atoms are thermally excited by sources electrically heated by resistances, inductors or electron-beams. The simplest sources rely on the Joule effect: such heaters must reach the evaporation temperature of the material but, at the same time, should neither contaminate, nor react or alloy with the evaporant, nor release gases. These requirements have led to develop and use resistance-heated sources such as refractory metal sources and crucibles.

Refractory metals are high melting point materials characterized by exceptional physical properties; in particular, they can tolerate very high temperatures and thermal shocks without reactions. Typical refractory metals are tungsten, tantalum and molybdenum with the first mostly diffused, even if for PVD the choice depends also on the depositing material. In general, sources are fabricated in various shapes, from wire filaments to boats, with the common property of a very low resistance requiring low-voltage, high-current supplies. Crucibles consist of cylindrical baskets composed of oxides, boron nitride, graphite, or refractory metals and heated by external tungsten filaments wound around them. Fig. 2.1 displays a few examples of sources for PVD.

(a)   **(b)**   **(c)**
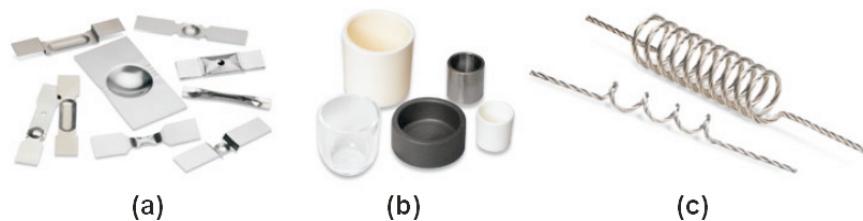
Figure 2.1: Evaporation sources - Examples of sources for PVD. (a) Refractory metal boats. (b) Crucibles (c) Refractory metal filaments

2.2   Thermal Evaporation of Germanium

As anticipated in the previous chapter, the first thermal evaporation of Germanium on Silicon was demonstrated in 1968 (17). In the early 80's Ge thin films on Si appealed strong interest as buffer layers for the integration of III-V semiconductors in photovoltaics applications. Studies on PVD of Ge were carried out in 1982 when Evangelisti *et al.* studied the influence of the evaporation parameters on the crystal quality (33; 34). In 1998 Colace *et al.* investigated PVD of Ge to realize the first evaporated Ge-on-Si photodiodes (35), followed by several devices fabricated with the same technology (29; 36; 37; 38; 39). These achievements are the background of this PhD.

Fig. 2.2 represents the evaporation system used in this work: it consists of a vacuum chamber in which a reduced pressure is obtained by two different pumping systems: a rotary pump allowing to reduce the ambient pressure to 10^{-3} $Torr$ and a cryogenic pump further reducing it to 10^{-8} $Torr$.
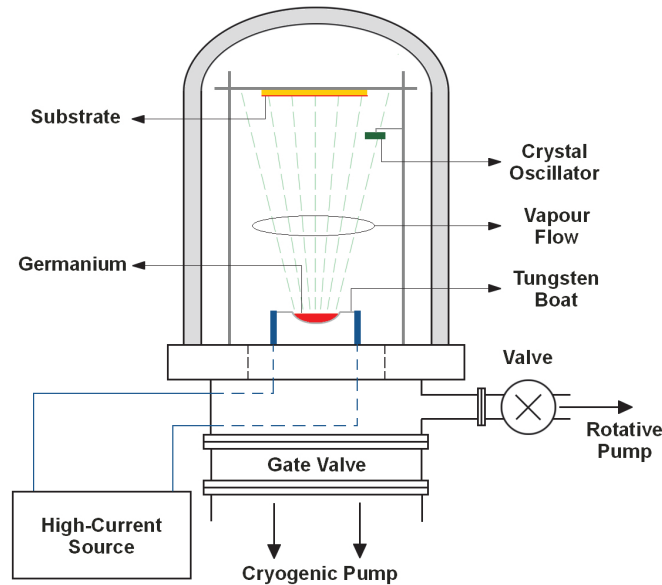
Figure 2.2: PVD system - Scheme of the evaporation system used to deposit Ge thin films on Si

The evaporation source consists of a tungsten boat fed by a low-voltage high-current power supply controlled by a Variac. The deposited material is pure Ge (99,999%) in

small grains: it melts at about $938°C$ and evaporates when the current reaches about 50 A. During evaporation the vacuum is maintained at about $10^{-7} Torr$. The film growth is controlled by a quartz microscale, an electronic circuit that uses the resonance of a vibrating crystal of piezoelectric material (quartz) to create an electrical signal with a precise frequency. During evaporation the material deposits on the crystal, varying the crystal oscillation frequency so that, with a proper controller, it is possible to extract information about the growth rate and film thickness.

The process flow began with the treatment of the substrate, typically Si or Silicon On Insulator (SOI). I adopted a standard procedure to prepare the specimens. As the substrates are standard 4" wafers and I worked with small samples, the first step consisted in wafer cleaving. The cleaved samples underwent a cleaning step in order to remove all the organic residues and other contaminants from the Si surface. This phase was conducted with a pre-cleaning with Acetone and Isopropanol followed by a complete RCA cleaning procedure. RCA is a standard set of wafer cleaning steps typically performed in semiconductor manufacture (Werner Kern developed the basic procedure in 1965 while working for RCA (Radio Corporation of America) - hence the name (40)). The basic procedure involves the following: removal of the organic contaminants (organic clean) performed with a slow oxidizing solution of NH_4OH:H_2O_2:H_2O at $75°C$; removal of the thin oxide layer (oxide strip) resulting from the previous step, consisting in a short dip in a diluted solution of HF:H_2O at room temperature; the last step is the removal of metallic contamination (ionic clean) with a solution of HCl:H_2O_2:H_2O at $75°C$. After RCA, the Si surface tends to easily oxidize in air forming a very thin film of native oxide film (SiO_2); it is important to remove this film before the deposition and, at the same time, to passivate the Si surface to prevent oxidation. This is quite relevant, as the presence of SiO_2 at the interface between Si and Ge dramatically affects the crystalline structure of Ge as well as the conduction properties of the heterojunction. Passivation consists of wet chemical etching of SiO_2, obtained by dipping the samples in a diluted buffered oxide etch (BOE, consisting of ammonium fluoride NH_4F and hydrofluoric acid HF). Besides removing the native oxide, BOE has also the important role of passivating the Si surface by terminating the dangling bonds of the Si surface with H ions. The hydrogen-passivated surface is chemically robust and resistant to oxidization, allowing to handle the specimens in air for the time necessary to place them in the vacuum chamber (41; 42).

Other important parameters affecting the deposition process are the substrate temperature T_s and the deposition rate D_r ($\mathring{A}/s$). As discussed in (31), these parameters strongly affect the crystal structure: for high T_s and low D_r large crystallite or even monocrystal formation occurs, while for low T_s and high D_r a polycrystalline or amorphous growth takes place. Substrate temperature was monitored by a control system heating the substrate holder via the Joule effect, a constant temperature was maintained by a feedback system with a thermocouple. This simple system allowed to heat the substrate up to $500°C$ with a $±1°C$ accuracy.

2.3 Material Characterization

The morphological and electrical properties of evaporated Ge thin films were characterized versus deposition parameters aiming at the optimization of the film quality. Raman and X-Ray spectroscopy were performed in order to investigate the effects of substrate temperature and deposition rate on the crystalline structure of the deposited films. Hall measurements allowed to asses the type of majority carriers, the equivalent doping density as well as resistivity and mobility. The electrical properties were confirmed by other characterization techniques such as Van Der Pauw and Transfer Length Measurement (TLM).

2.3.1 Raman Analysis

The investigation of the crystalline structure was first performed by Raman spectroscopy (43). This optical technique is based on the spectral analysis of light backscattered from a sample. Raman scattering stems from the interaction of light with matter: when light is scattered from the surface of a sample, it contains not only the incident wavelengths (*Raleigh* scattering), but also the wavelengths resulting from the interaction of photons with phonons in the material. In semiconductor analysis we study the interaction of light with the lattice vibrational modes (phonons) associated to the crystalline structure. If a photon interacts with a phonon it can release/absorb energy to/from it, so the back-scattered light contains photons with smaller/higher energy forming the *Stokes* or *anti-Stokes* modes (fig. 2.3). As the energy shift results from the interaction with the lattice, each material exhibits a specific response and can

be identified matching the measured shift to known Raman frequencies.
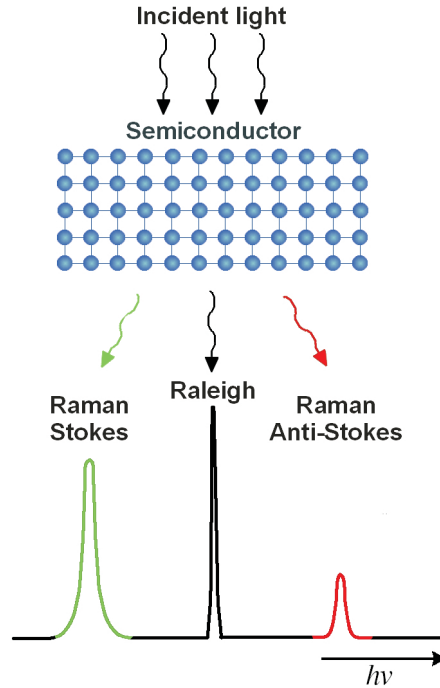
Figure 2.3: Raman scattering schematic - Schematic of the distribution of Raman scattered light

Stokes and anti-Stokes are very weak in intensity, about 1 part in 10^8 with respect to the Raleigh scattering, and exhibit only a small shift in frequency because of the energy associated to phonons. This is why, in Raman spectroscopy, an intense laser beam, typically He-Ne or Ar, is focused on the sample and the back-scattered light is collected and filtered to remove the intense Raleigh scattering and monitor the Stokes modes (statistically more intense and carrying the same informations of anti-Stokes). I performed a *micro*-Raman analysis using a HeNe laser source at 632.8 nm, controlling the intensity to prevent lattice deformation via local heating. The incident light was focused on the sample by a 100× microscope objective which also collected the back-scattered light filtered out by a notch and acquired by a CCD camera.

The Analysis of the Raman spectra gives informations on the overall crystal structure, as well as defects, stress and strain (44). The useful parameters in semiconductor characterization are: central frequency, shift, symmetry and width of the Raman peak.

The Raman frequency is a function of the interatomic forces within the crystal lattice: if the lattice spacing is altered, the Raman frequency shows a shift to lower or higher values. A Raman peak shift is mainly observed in lattices affected by residual stress; in particular compressive stress causes an up-shift, while a tensile strain gives rise to a down-shift. Other important information can be obtained by the symmetry of the Raman peak: in the presence of damaged or disordered crystals the Raman peak broadens, as result from the superposition of Raman peaks at shifted frequencies. While in amorphous semiconductors we can not observe a Raman peak due to the lack of lattice order, in polycrystalline semiconductors we observe asymmetric peaks broadened and shifted to lower frequencies: the smaller are due to the crystallites, the higher are associated to broadening and shift. This has been theoretically studied for Si with the phonon-confinement model (45) and experimentally observed in several other semiconductors. However, even if it is quite easy to discern a polycrystalline material, it is quite difficult to define if a sharp and symmetric peak is associated to a monocrystalline or a mono-oriented polycrystalline material; to make this distinction it is necessary to resort to other techniques, such as x-ray analysis.

Diamond-type materials, like Ge and Si, exhibit a first-order Stokes spectrum characterized by a sharp single peak corresponding to triply degenerate optical phonons (44). Bulk Ge and Si Raman spectra were accurately studied in the past (46; 47) giving important guidelines for correct measurements and their interpretation. Ge thin films were also investigated by Campbell *et al.* (48), who analyzed the changes in crystallinity of amorphous Ge-on-Insulator after re-crystallization. In this section I will discuss the Raman scattering of Ge thin films grown on different substrates including Si, silicon oxide and glass. Fig. 2.4 shows the typical Raman spectrum of a p-type lightly doped Ge (100) wafer. It consists of a single sharp peak centered at 302.6 cm^{-1} with a full width at half maximum (FWHM) of 3.3 cm^{-1}; the measured frequency is in good agreement with that reported in literature. Starting from this measurement, I characterized several samples of Ge evaporated on Si as a function of growth parameters.

The first analysis regarded the crystalline structure of Ge evaporated on Si kept at different temperatures. All the Si samples underwent the same cleaning and passivating treatments previously described. Ge films were grown at the same rate (about 2

$Å/s$) and vacuum (10^{-7} $Torr$) with a final thickness of 250 nm, while the substrate temperature was varied in the range 200-500°C.
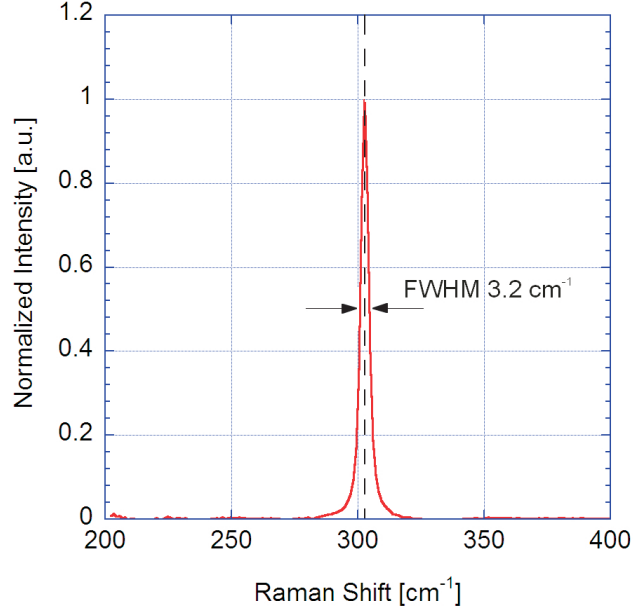
Figure 2.4: Germanium Raman spectrum - Raman Spectrum of a p-type bulk Germanium wafer

As expected, the substrate temperature was of paramount importance for the crystalline structure, as the evaporated Ge exhibits a crystalline structure only for substrate temperatures above a threshold between 225 and 250°C, consistently with analyses reported by other authors (34). Fig. 2.5 shows the normalized Raman spectra of the fabricated samples. For temperatures below threshold, the Raman spectrum is very weak, broadened and downshifted. From 250°C samples exhibit a sharp symmetric peak centered at 303 cm^{-1} (as the Ge wafer peak) demonstrating a mono-oriented crystalline phase fully relaxed back to the Ge lattice, without any stress or strain. For substrate temperature of 500°C the spectrum exhibits a slight asymmetric broadening towards low frequencies, suggesting a poly-oriented crystalline structure. This interpretation is supported by a comparison with Raman spectra of Ge evaporated on amorphous substrates such as SiO_2 or glass that necessarily refers to polycrystalline films.

Fig. 2.6 shows this comparison: the red line represents the Raman spectrum of Ge evaporated on Si at 500°C, while blue and black lines refer to Ge on SiO_2 at 300°C and
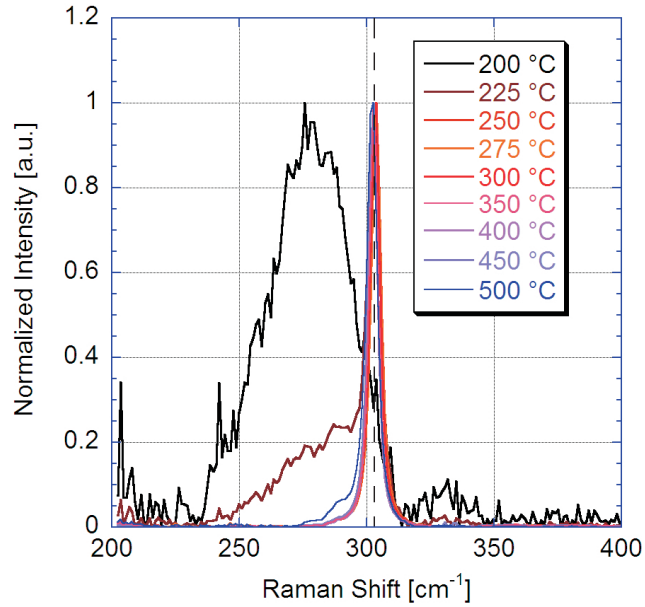
Figure 2.5: Ge on Si Raman spectra - Normalized Raman spectra of Ge evaporated on substrates kept at different temperatures from $200°C$ to $500°C$. For temperatures below $250°C$ is in the amorphous phase.
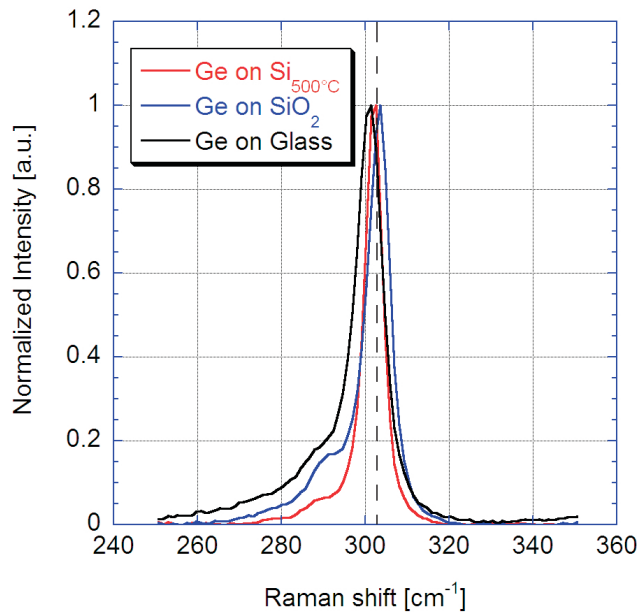
Figure 2.6: Raman spectra of Ge grown on different substrates - Normalized Raman spectra of Ge evaporated on various substrates. The dashed line represents the Raman frequency of Ge wafer.

to Ge on glass at $400°C$ (this temperature is higher to compensate the weaker thermal conductivity of glass), respectively. The figure shows the similarity of the three curves with a little bump at low frequency typical of a disordered crystalline structure.

The transition from amorphous to crystalline is gradual and goes through the formation of crystallites of increasing dimensions in a dominant amorphous structure. To observe this phenomenon I performed a deposition on a substrate subject to a temperature gradient along the surface. This was obtained by fixing one side of the the substrate at one side on the sample holder kept at a controlled temperature of $300°C$, while the rest of the sample remained at the ambient temperature of the vacuum chamber. Fig. 2.7 displays the spectra obtained from different points along the direction of the temperature gradient, from $300°C$ downward.
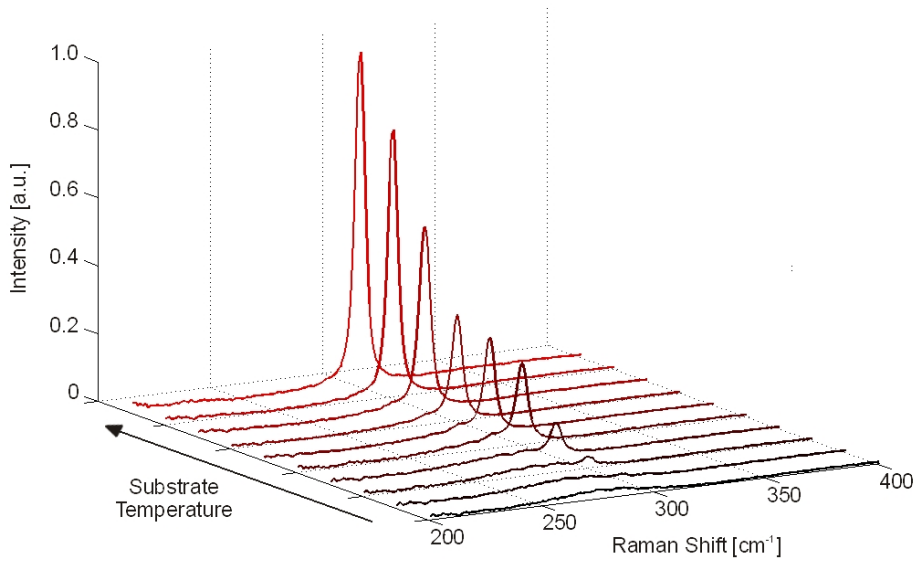
Figure 2.7: Amorphous-crystalline transition - Raman spectra of Ge evaporated on Si substrate subjected to a temperature gradient along the deposition surface starting from a controlled temperature of $300°C$ to the ambient temperature inside the vacuum chamber.

Starting from the very weak broadened spectrum of the amorphous phase, as the temperature of the substrate increases small crystallites begin to grow in the amorphous matrix, until the material reaches a fully crystalline structure, as pointed out by the small peaks emerging in the broad spectra.

As mentioned earlier, at temperatures above threshold Ge exhibits a mono-oriented crystalline structure, although from the FWHM emerges a certain defectivity of the crystal which is difficult to ascribe to either a mono-oriented polycrystal or to a defected monocrystal. The FWHM of Raman spectra obtained by Lorentzian interpolation are plotted versus substrate temperature in fig. 2.8.
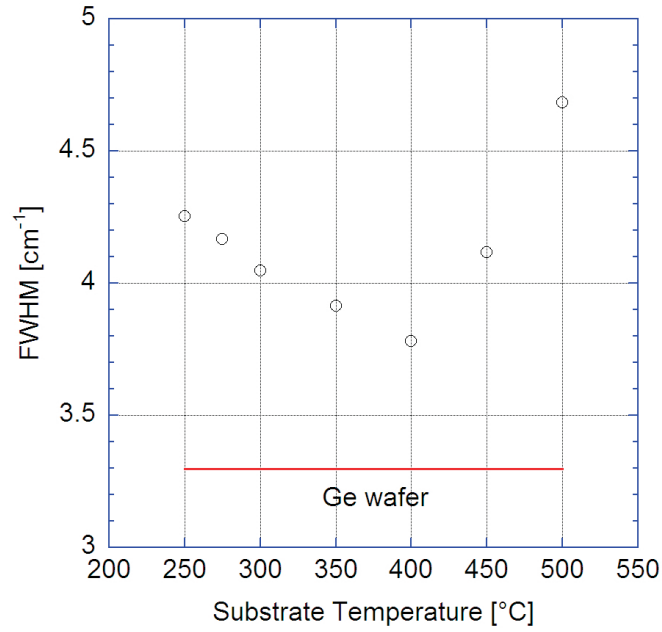
Figure 2.8: Full Width at Half Maximum of Raman spectra versus substrate temperature - FWHM of Raman spectra versus substrate temperature obtained by fit with Lorentzian functions.

The red-line represents the FWHM of a Ge wafer. The analysis shows an improvement in crystal quality as the temperature increases up to $400°C$, while for higher temperatures the quality worsens as pointed out by the asymmetric spectrum at $500°C$. The difference in FWHM compared with bulk Ge was expected for this kind of heterostructures and is attributed to misfit and threading dislocations. The improvement in crystal quality from low to high temperatures is explained by nucleation theory (31), whereby better crystalline structures are expected at higher temperatures. The worsening at temperatures above $400°C$ was unexpected. This can be explained keeping in mind that in PVD the crystalline structure is closely related to surface dynamics. In particular, the equilibrium between adsorption and desorption phenomena is

crucial for a uniform growth. Probably, at temperatures above $400°C$ adsorption is favored on some sites and desorption on other sites. In such conditions the formation of adatom clusters occurs via enhanced surface diffusion (31). This may explain the worsen crystalline properties at temperatures above $400°C$. As accurate analysis of these phenomena goes beyond the scope of this work.

The growth rate dependence was also studied by Raman spectroscopy. I prepared three samples with Ge deposited at 0.2 $Å/s$, 2.5 $Å/s$ and 20 $Å/s$ at a fixed temperature of $300°C$. The three spectra exhibited a sharp symmetric peak centered at the same frequency of bulk Ge, indicating a relaxed mono-oriented crystal. Fig. 2.9 shows the FWHM versus growth rate compared with the best FWHM obtained by varying the substrate temperature and the FWHM of bulk Ge.
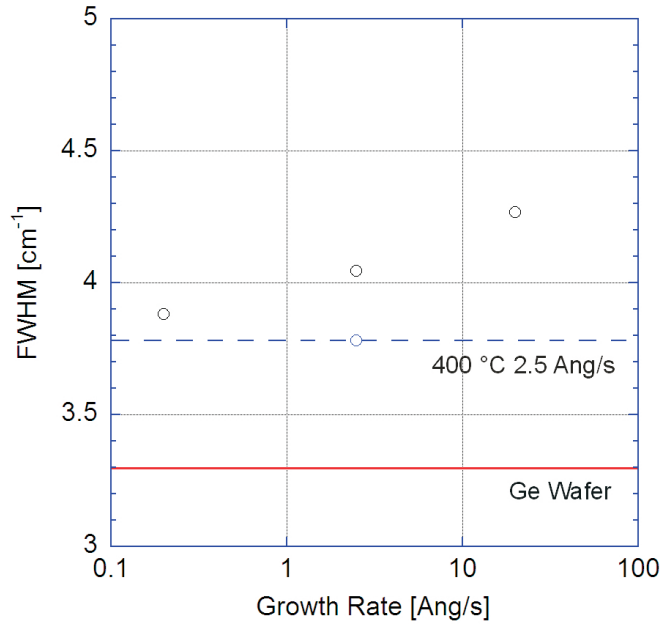
Figure 2.9: Full Width at Half Maximum of Raman spectra versus growth rate - FWHM of Raman spectra versus growth rate, obtained by fit with Lorentzian functions.

As predicted by theory (31), at lower growth rates the crystal quality improves. Moreover at $300°C$ and 0.2 $Å/s$ the Raman peak is almost as sharp as at $400°C$ and 2.5 $Å/s$, indicating that it is possible to improve the quality without increasing the temperature but only acting on the growth rate.

In conclusion, the micro-Raman analysis produced very interesting results concerning the deposition parameters. Ge evaporated on substrates at various temperatures allowed to determine a threshold over which the material had a good crystalline quality, with a trend showing a maximum for temperatures around $400°C$. Further increasing the substrate temperature worsens the crystalline structure and promotes the formation of a polycrystalline film. It is therefore convenient to perform evaporations in the range $300\text{-}400°C$. In this interval, the evaporated Ge lattice appears fully relaxed and mono-oriented. However, the FWHM of Raman peaks indicates the presence of crystalline defects that can be associated to both dislocations and mono-oriented polycrystals.

2.3.2   X-Ray Analysis

X-ray Diffraction (XRD) is a powerful non-destructive technique used to investigate the structural properties of crystalline materials. In particular, XRD analysis is an important tool in semiconductor applications, as it requires little sample preparation but gives important structural information over large-area samples. Strain, crystalline phase, grain size as well as defect structure and preferred orientation can be accurately identified by this technique, providing a complete characterization of the semiconductor structure. I will briefly introduce the fundamentals of X-Ray techniques; a more rigorous treatment can be found in specific textbooks (49; 50; 51).

XRD techniques are based on the elastic scattering of X-rays from long-range order structures like crystals. Crystalline materials consist of atomic planes *(hkl)* spaced by d_{hkl} (*h,k,l* being the Miller indices) depending on the crystallographic direction of interest. X-rays incident on the crystal are scattered by the atomic planes: when the scattered X-rays undergo constructive interference, a diffraction peak can be observed and analyzed. Constructive interference arises when the angle between the incident beam and the atomic planes satisfies the Bragg condition:

$$\lambda = 2d_{hkl}sin\left(\Theta_B\right) \tag{2.1}$$

where λ is the X-Ray wavelength, typically in the range 0.7-2 Å. The diffracted beam is collected by a detector held at twice the Bragg angle. Nevertheless, due to the finite dimensions of the crystal, the diffracted beam emerges with a finite angular range centered at the Bragg angle where a diffraction occurs. When the lattice spacing or the lattice plane orientation is locally distorted by structural defects, the angular spectra change both position and width.

The characterization of epitaxial layers is generally performed by High-Resolution X-Ray Diffraction (HR-XRD). This requires a monochromatic highly-collimated beam to achieve high angular resolution by means of double-crystal diffraction from a couple of perfect single crystals. The detector is fixed near the diffraction angle for the *(hkl)* planes of interest, and the receiving slits are open to accept large angular spectra. This technique ensures the measurement of narrow diffraction peaks, enabling the accurate determination of very small deviations in d-spacing. Double-crystal diffraction can be

extended to three and four crystals to further collimate the X-ray beam and obtain a higher resolution.

The double-crystal technique is used for determining *rocking curves*. Rocking curves are diffraction profiles obtained by slowly rotating or "rocking" the specimen about an axis normal to the diffraction plane. The scattered intensity is recorded as a function of the angle in the proximity of the chosen Bragg angle. Rocking curves provides information about epitaxial layers, the high resolution allowing to carefully measure the lattice mismatch by measuring the angular distance between epitaxial layer and substrate peaks. The curve width can be associated to the defect density in the material: the narrower the curve, the more perfect is the material.

The crystalline quality of evaporated Ge was characterized by HR-XRD. The samples were investigated with a high resolution diffractometer with a Cu X-ray tube as the source; the CuKα line was selected by means of a Ge (220) crystal "channel-cut" monochromator in the Bartels configuration (52). The measurements were performed on the (400) planes of both Si and Ge with a wavelength resolution $\Delta\lambda/\lambda = 10^{-4}$. The Bragg angles of (400) planes of Ge and Si are $\Theta_B = 33.00°$ and $\Theta_B = 34.56°$, respectively; therefore the relaxed Ge layer on Si was expected to exhibit an angular separation of 1.56°. The first characterization was performed on Ge evaporated on Si at substrate temperatures ranging form $200°C$ to $500°C$, grown at a constant rate of 2.5 $\mathring{A}/s$. Fig. 2.10 shows the normalized rocking curves with the Si diffraction peak aligned to zero. As observed by Raman characterization, the Ge exhibited a crystalline structure for temperatures above $250°C$. Samples at $200°C$ did not exhibit any peak, owing to the amorphous structure already diagnosed by Raman analysis; at $225°C$ a weak diffraction peak was observed. For substrate temperatures in the range $300\text{-}400°C$ the material exhibited peaks of maximum intensity, suggesting a better crystalline quality confirmed by fig. 2.11 displaying the FWHM versus temperature. At higher temperatures the peak intensity decreased and was drastically reduced at $500°C$, probably due to a poly-oriented structure dispersing the X-Ray scattering to different Bragg directions. This is in agreement with the Raman spectra (fig. 2.6) where the $500°C$ peak exhibited a similar shape of Raman peaks for polycrystalline Ge grown on glass.

Although Ge films appeared fully relaxed to the Ge lattice ($\Delta\Theta \approx 1.56°$), a small deviation of the angular distance between Si and Ge peaks was observed, suggesting a little amount of lattice stress probably associated to the different thermal expansion
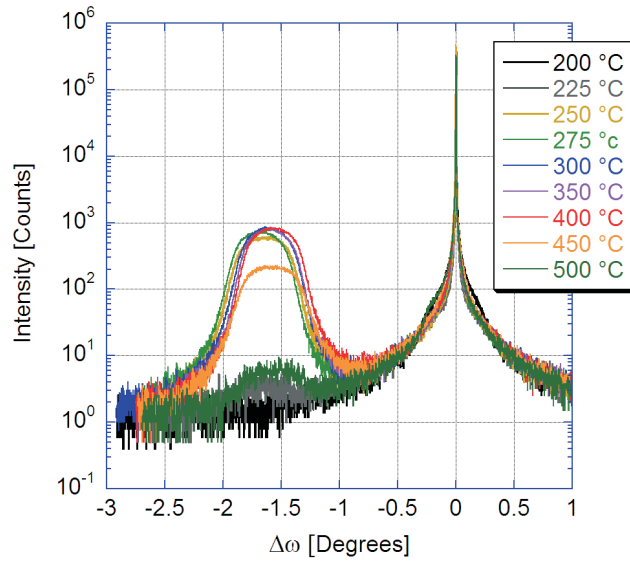
Figure 2.10: HR-XRD analysis of evaporated Ge versus substrate temperature - Rocking curves of Ge evaporated on Si at substrate temperatures ranging from 200 to $500°C$
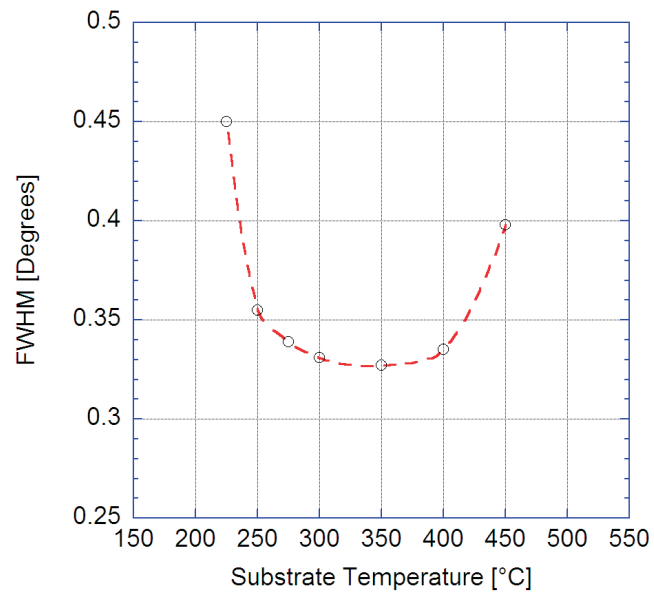
Figure 2.11: Rocking curve FWHM - FWHM of Ge rocking curves versus substrate temperatures.

coefficients of Ge and Si. In particular, the Ge peaks appeared rather broadened with FWHM $\approx 0.35°$, the latter associated to highly defected structures. HR-XRD analysis was also performed on samples grown at different rates (0.2, 2.5, 20 $\mathring{A}/s$) at a fixed temperature of $300°C$. The results are plotted in a linear scale in fig. 2.12. All samples exhibited good quality, with crystallinity improving at lower rates as already observed by Raman analysis.
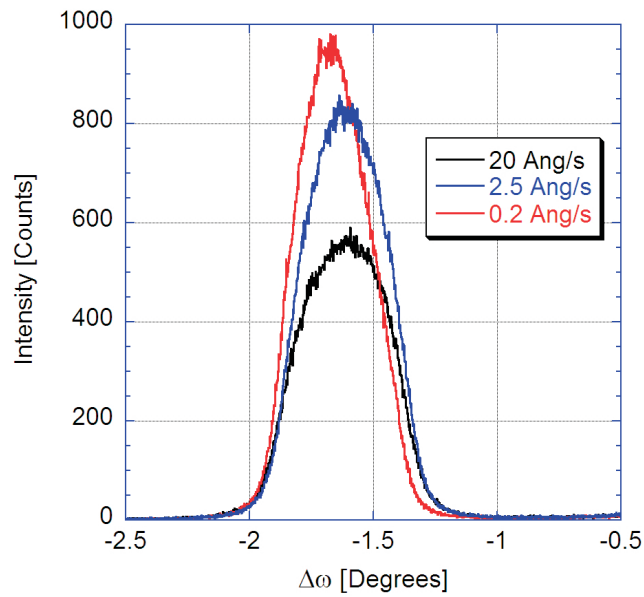
Figure 2.12: HR-XRD analysis of evaporated Ge versus growth rate - Rocking curves of Ge evaporated on Si at $300°C$ for different growth rates.

It is possible to conclude that, in the range 300-$400°C$, evaporated Ge exhibits a mono-oriented crystalline structure fully relaxed to the Ge lattice constant. The broad peaks suggest a mosaic-like texture of the films, probably caused by threading dislocations. Unfortunately, in general it is not possible to infer a threading dislocation density from the peak broadening, because of the effect of misfit dislocations at the interface between layer and substrate. This aspect was investigated by transmission electron microscopy.

2.3.3 Transmission Electron Microscopy

Transmission Electron Microscopy (TEM) is a major tool in material science. The extremely high lateral spatial resolution, approaching 0.08 nm, and the capability to provide both image and diffraction information from a single sample make TEM one of the best tools for material characterization. Unfortunately, this is a destructive technique and requires a careful preparation of the samples. A detailed description of the working principle can be found elsewhere (49; 50; 51), here I will discuss the results obtained by diffraction patterns as well as cross section images of the samples.

In the diffraction mode, information about the crystalline phase is obtained by studying the diffraction pattern. In fact, single crystals, poly-crystals and amorphous materials exhibit clearly different diffraction patterns. Monocrystalline materials provide patterns with aligned dots representing the reciprocal lattice projection on the observation plane; polycrystalline and amorphous materials exhibit diffraction patterns with a series of rings arising from random diffraction by the disordered structure. Fig. 2.13 shows a few examples (images from ref. (50)).

(a)   (b)   (c)
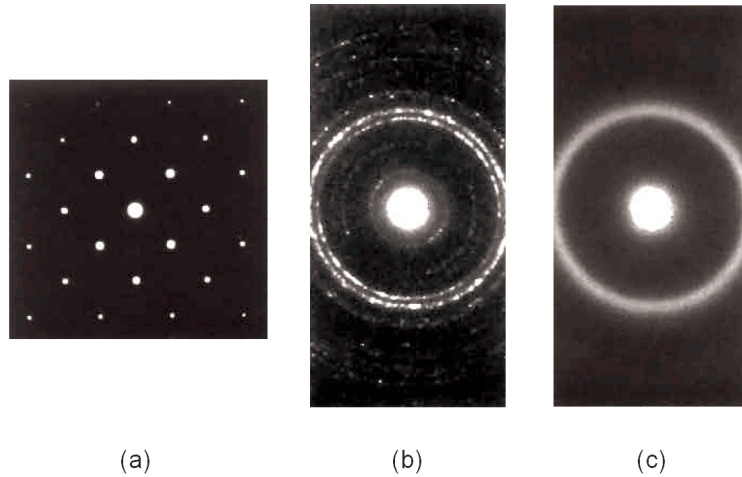
Figure 2.13: Diffraction pattern of crystalline phases - Diffraction patterns of: (a) single crystal, (b) polycrystalline thin film and (c) amorphous film. Images from ref. (50).

In order to determine whether the evaporated Ge was mono- or poly-crystalline, we studied the diffraction pattern of a sample grown on Si at $300°C$ and 2 $Å/s$. Fig.

2.14 shows the obtained pattern: two distinct sets of spots are clearly visible, the inner one corresponding to the Si lattice and the outer one to Ge lattice are clearly visible.
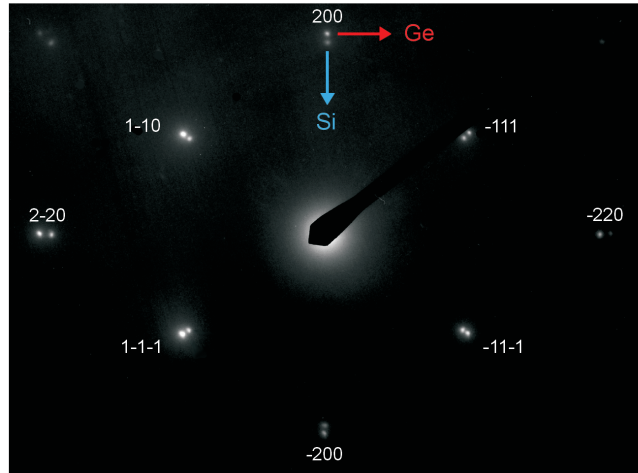
Figure 2.14: Diffraction pattern of Ge evaporated on Si - Diffraction pattern from a thin film of Ge evaporated on Si at $300°C$ at a growth rate of 2 $\mathring{A}/s$. The image indicates an epitaxial film of Ge.

The perfect alignment between the two sets indicated that the Ge film was epitaxial and mono-crystalline with the same orientation of the substrate, while the distance between spots confirmed the relaxation to the Ge typical lattice constant.

Combining the results obtained by Raman, XRD and TEM diffraction, it is possible to conclude that the Ge evaporated on Si is epitaxially grown with mono-crystalline structure. The observed texture can be ascribed to dislocations affecting the crystal. This aspect was investigated performing cross sectional TEM (X-TEM). Fig. 2.15 shows an X-TEM acquisition of the Ge-on-Si specimen. The Ge film was affected by a high threading dislocation density originating from misfit dislocations at the hetero-interface and moving through the Ge film towards the surface. The film was also affected by planar defects nucleating at the Ge/Si interface and moving along the {111} direction, as shown in the inset of fig. 2.15 (a 2X magnification of the selected area).

In conclusion, Ge grown at $300°C$ and 2 $\mathring{A}/s$ on Si had a mono-crystalline structure co-oriented with the Si substrate, suggesting the epitaxial nature of the film. The similarities in Raman spectra and XRD rocking curves in the range 300-400° allow to assume mono-crystallinity of those temperature with variations in dislocation density.

It would be interesting to asses the role of thermal treatments on the material, but rapid thermal annealing (RTA) would make less appealing the low-cost and low-temperature character of PVD as a suitable technique for Ge on CMOS.
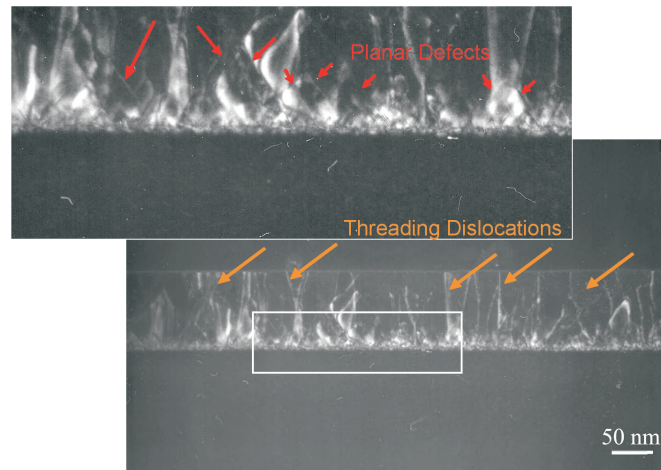
Figure 2.15: Cross sectional TEM images of evaporated Ge - TEM cross section of Ge evaporated on Si at $300°C$ at a growth rate of $2 \, \AA/s$. The image shows high dislocation as well as planar defect densities. The top photo is a magnification of the selected area.

2.3.4 Electrical Characterization

Since the final aim of this dissertation work was the realization of Ge-on-Si optoelectronic devices, it was important to study the electrical properties of the material and investigate their relationship with structural characteristics. The analysis included resistivity and Hall measurements to identify the majority carrier type, concentration and mobility. As the characterization involved the fabrication of specific samples with metal/semiconductor contacts, a preliminary study on the realization of ohmic contacts on Ge was carried out.

TLM measurements

Without detailing the theory of metal-semiconductor contacts, I will briefly introduce to ohmic contacts and their characterization. Ohmic contacts exhibit a linear current-voltage characteristic, regardless a small voltage drop across the contact. In this case, the contact must be able to supply the necessary device current, the voltage drop of the contact should be small compared to the voltage drops in the active regions of the device, the contact should not inject minority carriers (51). The ohmic characteristic is governed by the contact resistance, including all the conduction effects at the metal-semiconductor interface: interface resistance (*specific interfacial resistivity*(51)), current crowding, oxide or other layers at the interface, etc. The contact resistance is characterized by the *specific contact resistivity* ρ_c ($\Omega \cdot cm^2$), independent of contact area and useful when comparing different contact geometries. In a planar geometry, in which contacts are on the surface of the thin film and the current flows parallel to it as in fig. 2.16, the contact resistance distribution along the contact length depends on the sheet resistance R_{sh} of the semiconductor and on ρ_c, according to (51; 53):

$$R(x) = \frac{\sqrt{R_{sh}\rho_c}}{Z} \frac{cosh\left[(L-x)/L_T\right]}{sinh\left(L/L_T\right)} \tag{2.2}$$

where L and Z are the contact length and width, respectively.

$R(x)$ decreases nearly exponentially with the distance from the contact edge. L_T is defined *transfer length* and represents the active length under the contact, i.e. the distance over which most of the current flow takes place between metal and semiconductor; its analytical expression is:
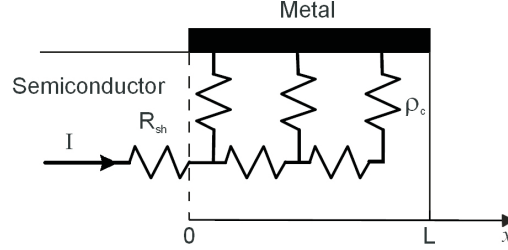
Figure 2.16: Contact resistance schematic - The contact resistance is represented by the $\rho_c - R_{sh}$ equivalent circuit. Current transfers from metal to semiconductor along the least resistance path defined by the transfer length L_T

$$L_T = \sqrt{\frac{\rho_c}{R_{sh}}} \tag{2.3}$$

For good ohmic contacts, typical transfer lengths are on the order of 1 μm or less. Eq. 2.2 at $x = 0$ gives the contact *front* resistance, usually referred to as the contact resistance R_c; substituting eq. 2.3 in eq. 2.2 we have:

$$R_c = \frac{\rho_c}{L_T Z} coth \left(\frac{L}{L_T} \right) \tag{2.4}$$

and, assuming $L >> L_T$, $coth \left(L/L_T \right) \approx 1$:

$$R_c \approx \frac{\rho_c}{L_T Z} \tag{2.5}$$

In this work ohmic contacts on evaporated Ge were characterized by the *transfer length method* (TLM). This method allows extracting ρ_c and R_{sh} by simple resistance measurements. The TLM test structure is reported in fig. 2.17 (top): it consists of a rectangular mesa provided with several contacts of identical dimensions and increasing spacings d. By imposing a constant current between contacts A and E, and then measuring the voltage drop across adjacent contact pairs (A-B,B-C,C-D,D-E), it is possible to extract the total resistances R_T of the single segments. The total resistance between any contact pair is:

$$R_T = \frac{R_{sh}d}{Z} + 2R_c \approx \frac{R_{sh}}{Z}(d + 2L_T) \tag{2.6}$$

Plotting the measured R_T versus d it is possible to extract R_{sh}, R_c and L_T by simply fitting the experimental data with eq. 2.6, as shown in fig. 2.17.
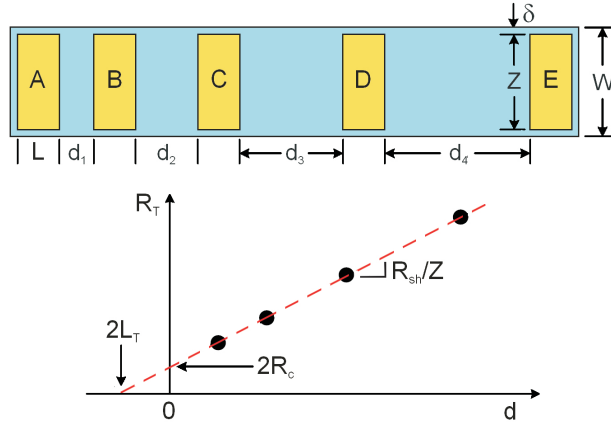
Figure 2.17: Transfer length method - TLM test structure and plot for the parameter extraction according to eq. 2.6. It is necessary a mesa etching of the structure to ensure a one-dimensional voltage distribution between the contacts. The difference δ between mesa and contact height $(W - L)$ should be as small as possible to avoid shunt effects in the measured resistance.

The intercepts with the R_T-axis and the d-axis give the contact resistance R_c and the transfer length L_T, respectively, while the slope is proportional to the sheet resistance R_{sh} of the semiconductor. Although this method is commonly used in contact characterization, it is important to check the validity of some assumptions. First, the model assumes that the potential distribution is one-dimensional, i.e., in a structure in which the difference between the mesa and the contact heights is the least possible $(W \approx Z)$ to avoid current flowing on paths different form the d direction. Second, the extraction of parameters depends on eq. 2.6 that holds only for $L \gg L_T$.

In thin film electric characterization a complication arises from the influence of the substrate. If a proper isolation between the thin film and the substrate is not assured, the measurements will be affected by shunt effects preventing the correct interpretation of results. A common approach to isolate the two layers is to adopt a highly resistive

substrate of opposite majority-carrier type, to take advantage of the depletion region totally extending in the substrate. As evaporated Ge films are generally highly doped p-type (4)(Hall measurement confirmed this assumption, as I will discuss later in this section), I used very low doped n-type Silicon on Insulator (Si 220 nm - $10 \div 30$ Ωcm) for the substrates. SOI was chosen to fabricate TLM mesa structures etched down to the SiO$_2$ underlayer, in order to avoid any undesired current path in the Si underlayer, even if unavoidable leakage could arise from a non-perfect interface of the pn junction. The samples consisted of 850×200 μm^2 mesas with 100×200 μm^2 contact pads spaced as: $10 - 20 - 40 - 80 - 100$ μm. The metal selected to form ohmic contacts on the p-type Ge was a thin bi-layer of 50 nm Chromium (Cr) and 50 nm Gold (Au) without any annealing: the electric contact was provided by Cr while oxidation of Cr was prevented by the Au thin layer.

Fig. 2.18 shows a typical TLM fit obtained with AuCr contacts on evaporated Ge on SOI: the total resistances R_T were extracted by linear fitting the V-I characteristics of the single contact pairs; the extracted transfer lengths, less than 1 μm, and specific contact resistances, about 10^{-6} Ωcm^2, demonstrate optimal ohmicity of these contacts.
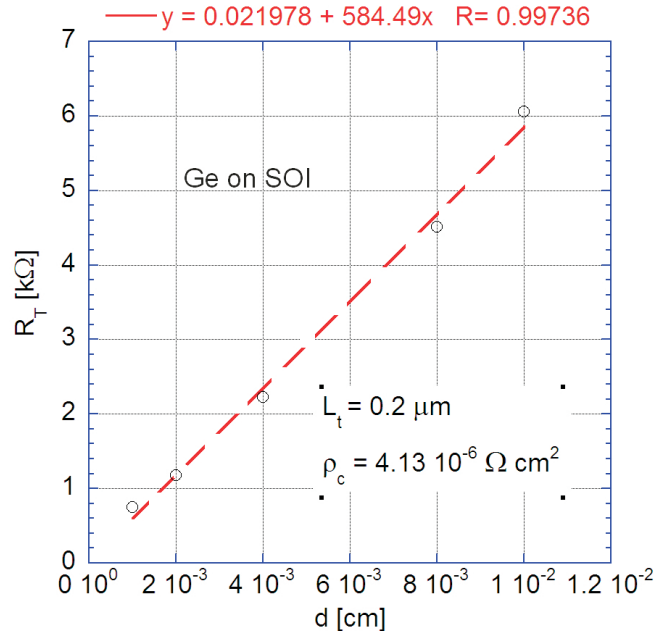
Figure 2.18: TLM measurement of Ge on SOI - Typical TLM plot of AuCr contacts on Ge evaporated on SOI at $300°C$ and 2 $Å/s$.

The same measurements were performed on Ge evaporated on SiO_2. Although the material exhibited a different crystalline structure, it was interesting to investigate how the electric characteristics changed in the two cases, so it was important to verify if also the AuCr on polycrystalline Ge exhibited the same ohmic behavior. Fig. 2.19 shows a typical result for an AuCr-poly Ge interface: L_T is still in the order of 1 μm but almost 10 times larger, as reflected on the contact resistance that is two order of magnitude higher.
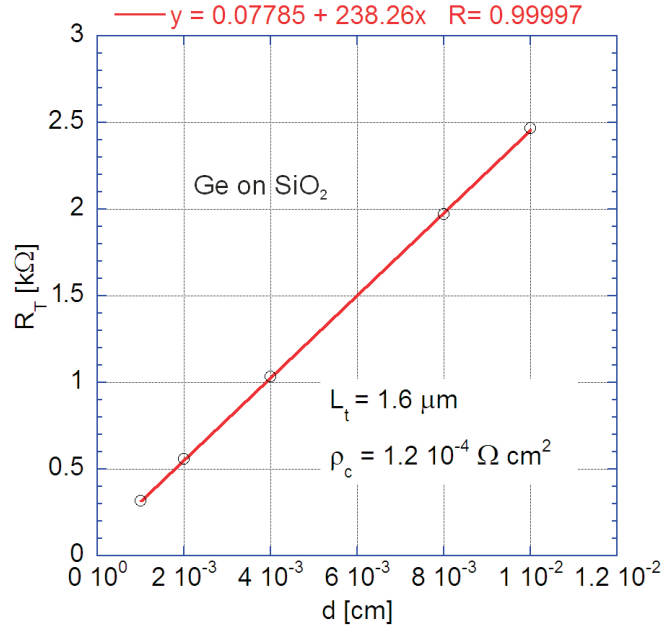
Figure 2.19: TLM measurement oF Ge on SiO_2 - Typical TLM plot of AuCr contacts on Ge evaporated on SiO_2 at $300°C$ and 2 $\mathring{A}/s$.

It is possible two conclude that in both cases the AuCr-Ge system provided a good ohmic contact without any annealing, an important result because simplifies the fabrication avoiding thermal treatments. Tab. 2.1 summarizes the typical results of TLM characterization.

Parameter	Ge on Si	Ge on SiO$_2$
R$_{sh}$	11 $k\Omega/\square$	5 $k\Omega/\square$
R$_c$	11 Ω	33 Ω
L$_T$	0.2 μm	1.6 μm
ρ_c	$4 \cdot 10^{-6}$ Ωcm^2	$1.2 \cdot 10^{-4}$ Ωcm^2

Table 2.1: TLM parameters - Typical results of TLM measurements for AuCr/Ge contacts

Hall measurement: resistivity and mobility

The Hall effect was discovered in 1879 by Edwin H. Hall (54): when he observed that a small transverse voltage appeared across a thin gold strip carrying current in an applied magnetic field. Since then, the Hall-effect technique became a widely diffused tool in semiconductor characterization, because it allows extracting resistivity, carrier density and mobility. The Hall effect is extensively discussed in physics books; here I will report the basics about the electric properties derived from Hall measurements.

Fig. 2.20 shows a bridge-type sample with four lateral arms, the typical bar geometry used in Hall measurements.
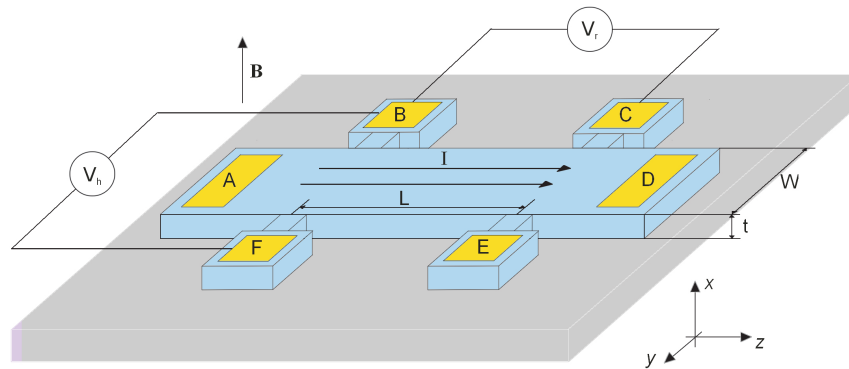
Figure 2.20: Hall bar - A typical Hall bar sample. The Hall voltage is measured between terminals B and F in the presence of a magnetic field, while the resistivity is extracted in the absence of magnetic field from the voltage drop between terminals B and C.

A constant current I flows from terminal A to terminal D along the z direction. Applying a constant magnetic field B in the x direction, carriers are deflected in the y direction by the Lorentz force, according to the vector expression:

$$\vec{F} = q\left(\vec{E} + \vec{v} \times \vec{B}\right) \tag{2.7}$$

where q is the electron charge, $\vec{E}$ the electric field causing the current flow, $\vec{v}$ the carrier velocity and $\vec{B}$ the applied magnetic field. As no current can flow along y, the force deflecting the carriers is compensated by an induced electric field in that direction, causing a voltage drop between terminals B and F (as well as C and E): this is the Hall voltage V_h. If we are testing a p-type material, the majority carriers (i.e. holes) flow in the positive z direction, therefore they are deflected towards E and F contacts and $V_h = V_B - V_F$ is negative; while for n-type materials electrons flow in the opposite direction resulting in a positive V_h. The Hall voltage expression for a p-type material is:

$$|V_h| = \frac{BI}{t}\left|\frac{1}{qp}\right| = \frac{BI}{t}|R_h| \tag{2.8}$$

where t is the bar thickness and p the hole concentration. R_h is the Hall coefficient. For n-type materials the hole concentration is substituted by the electron concentration. Measuring V_h versus I, R_h can be evaluated from the slope of the linear fit of the V_h-I characteristic according to eq. 2.8. The carrier type is extracted from the sign of the slope ($R_h > 0$ electrons, $R_h < 0$ holes), while the carrier concentration is:

$$n, p = \frac{1}{q|R_h|} = \frac{B}{qt}\left|\frac{I}{V_h}\right| \tag{2.9}$$

The material resistivity can be obtained by a simple four point measurement on the same Hall sample when the magnetic field is turned off; in particular, when a constant current I flows between terminals A and D, the voltage drop $V_r = V_B - V_C$ is:

$$V_r = \rho\frac{LI}{tW} \tag{2.10}$$

with L the distance between terminals B and C, W the bar width. Usual Hall bars have $L = 2W$. The semiconductor resistivity can be inferred by fitting the slope of V_r versus I:

$$\rho = \frac{t}{2} \frac{V_r}{I} \tag{2.11}$$

Combining the Hall coefficient and resistivity it is possible to derive the Hall mobility μ_h, defined as:

$$\mu_h = \frac{|R_h|}{\rho} \tag{2.12}$$

The Hall mobility does not necessarily correspond to the conduction mobility. The uncertainty arises from a simplification in the Hall coefficient formulation of eq. 2.8, where no scattering mechanisms are involved. Actually, two scattering mechanisms are present in the Hall technique, lattice scattering and impurity scattering. If we take scattering into account, eq. 2.9 becomes:

$$n, p = \frac{r}{q\,|R_h|} \tag{2.13}$$

where r is the Hall scattering factor, generally between 1 and 2. The scattering factor is a function of both temperature and magnetic field and it approaches unity when the condition $\mu B >> 1$ is satisfied, i.e. in the high field regime. This condition is difficult to achieve in common measurement systems, because of the high magnetic fields required, about 10 T (typical magnetic fields lie between 0.05 and 1 T, so $r > 1$ for most Hall measurement). A dissertation about the Hall scattering factor can be found in *Blood and Orton* (55). I studied the Hall mobility as I was mainly interested in growth-parameter dependence.

The Hall measurements were performed on thin films of Ge evaporated on low doped n-type SOI substrates to prevent shunt effects, as explained in the previous section. The Hall bars were fabricated by standard lithography with $W = 400\mu m$ and $L = 200$ μm (see fig. 2.20). The Si underlayer was patterned as the Ge bar by selective etch down to the SiO_2. This prevent alternative current paths from leakage current between Ge and the substrate. The contacts were made in AuCr defined by the lift-off technique. Fig. 2.21 and 2.22 show typical results for a thin film of 250 nm of Ge grown

at $300°C$ on SOI.
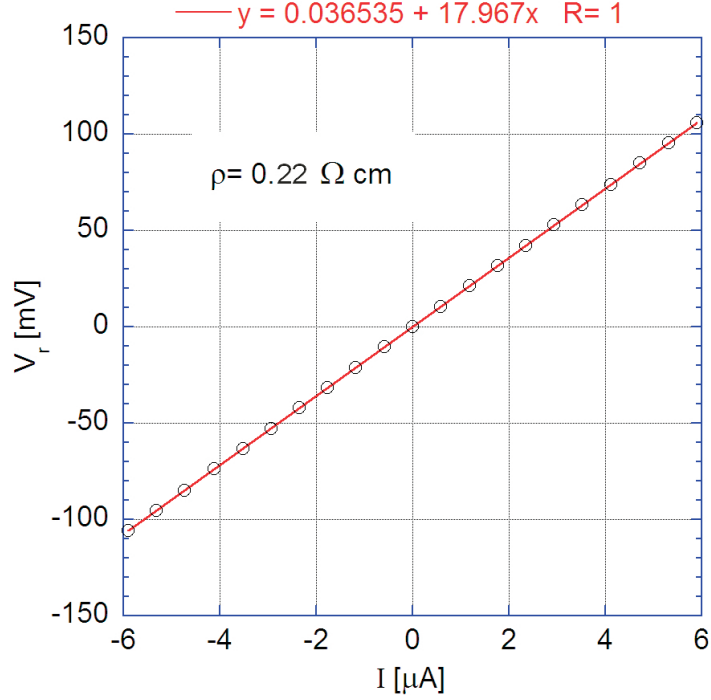
Figure 2.21: Four probe measurement of resistivity - Four probe measurement on
Ge evaporated on SOI.

The linear fit of V_r versus I in fig. 2.21 allows estimating a material resistivity of
about $0.2\ \Omega cm$.

Fig. 2.22 plots the fit of V_h versus I: the negative slope demonstrates that the evapo-
rated Ge is a p-type material, even without intentional doping. The typical majority
carrier concentration, evaluated by eq. 2.9, is $p = 4 \cdot 10^{17}\ cm^{-3}$. According to eq.
2.12, the typical Hall mobility for Ge evaporated on SOI at $300°C$ is about $85\ cm^2/Vs$,
five times lower than in bulk Ge for the same hole concentration. p-type unintentional
doping was already observed in the past (34), and commonly associated to the defects
affecting the material crystalline structure. As studied by Raman and X-Ray analysis,
Ge evaporated on Si suffers from high threading and misfit dislocation density; some
of these defects probably act as traps for electrons, producing active levels near the
edge of the valence band. An in-depth analysis on how structural defects influences
the electronic properties of the material is a challenge: its study is one of the future

developments of this work.
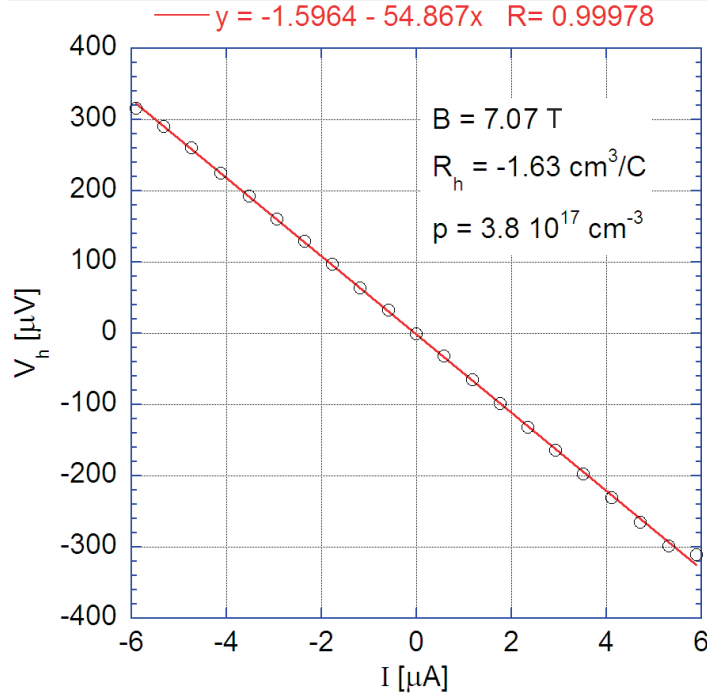
Figure 2.22: Hall measurement - Hall voltage measurement on Ge evaporated on SOI.

The electronic properties such as resistivity, hole concentration and Hall mobility were analyzed versus growth parameters. The same set of samples characterized by Raman and X-Ray spectroscopy were used to study the relationship between electronic properties and crystalline structure. The first set of measurements involved samples grown at different substrate temperatures, from $300°C$ to $500°C$ in $50°C$ steps and at a constant rate of $2.5 \mathring{A}/s$. Fig. 2.23 shows typical resistivities versus substrate temperature. As T_s increases, the material becomes more conductive, with a monotonic trend. The hole concentration versus substrate temperature is showed in fig. 2.24. The hole concentration increases by about one order of magnitude in the temperature range of interest. This is not clearly related to the crystal structure. In fact, both Raman and XRD analyses showed that the crystalline quality is first improved and then worsened by increasing temperatures, with best structure around $400°C$.
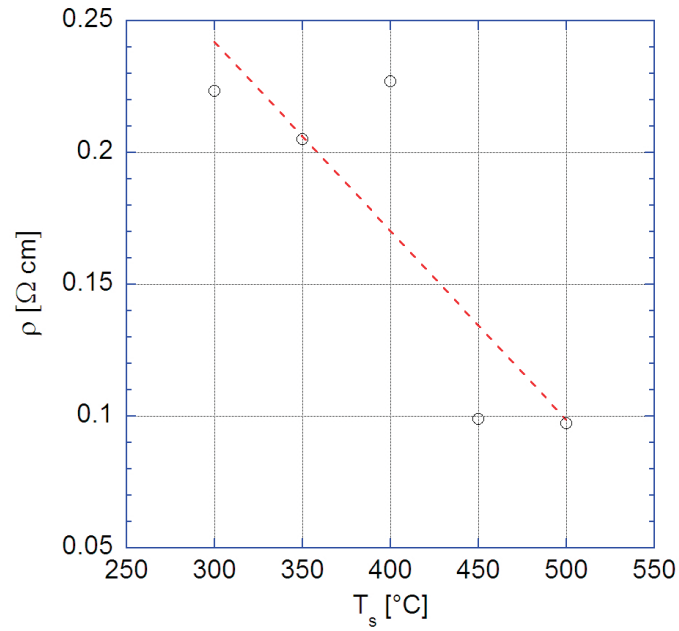
Figure 2.23: Resistivity versus substrate temperature - Resistivity of Ge evaporated on SOI versus substrate temperature
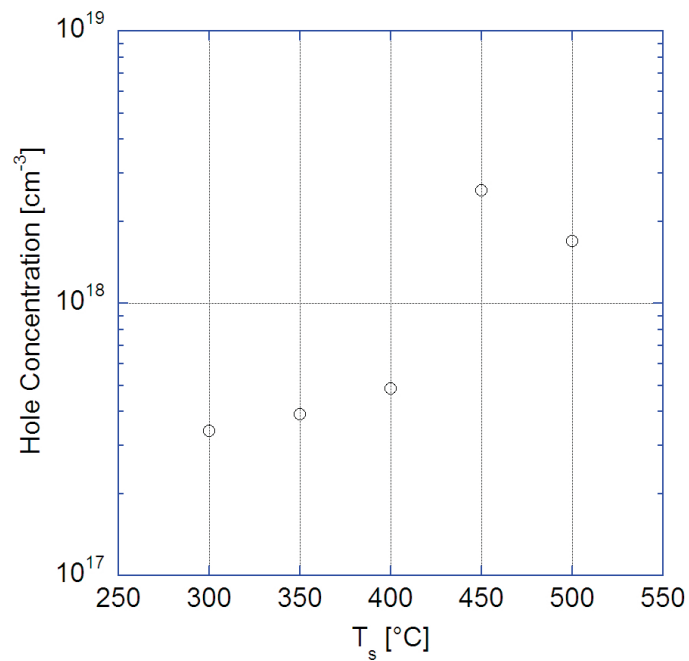
Figure 2.24: Hole concentration versus substrate temperature - Hall concentration of Ge evaporated on SOI versus substrate temperature

A correct interpretation of the results would require an extensive study of the conduction mechanisms in the thin film. In fact, if we take the unintentional doping as a direct consequence of acceptor-like defects, we have to consider a trap-assisted conduction model. In such conditions many complications arise. First, the Hall effect is based on the assumption of ohmic conduction in the sample; if this assumption is not validated, the derivation of carrier conduction properties is more involved. Second, it is not simple to assess whether the defects exhibit a magnetic behavior and how this can affect the Hall measurement. Finally, establishing a correct relationship between crystal structure and electric properties would require an extensive characterization of energy levels of defects in different crystals. The results in fig. 2.24 are probably associated not only to increasing defect concentrations (fig. 2.24 would show the same characteristic of fig. 2.8 and fig. 2.11) but also to different energy level distributions in the band gap (at different substrate temperatures). Regretfully, the investigation of these aspects involves extensive and more sophisticated characterization techniques such as Deep Level Transient Spectroscopy (DLTS) and/or Electron Beam Induced Current (EBIC), not available to me during my PhD.

Finally, fig. 2.25 shows the obtained values of mobilities versus T_s, where μ_h has a decreasing trend (as expected from the relationship with resistivity and carrier concentration). Despite the issues arising from the possible non-ohmic transport in the Ge film, the results of the Hall characterization provide some important information about the electric properties of Ge evaporated at different temperatures. Fig. 2.25 shows that the best transport properties are obtained for optimal substrate temperatures between 300 and 350°C. This is particularly interesting as the main aim of this growth technique is to minimize the thermal budget.

In conclusion, Ge evaporated on Si exhibits high p-type doping associated to acceptor levels due to the highly-defected crystal structure. Ge thin films exhibit low Hall mobilities, due to the high dislocation density in the evaporated material. The Hall characterization pointed out that the best growth conditions are realized for a substrate temperature of 300°C and a growth rate of 2.5 $\mathring{A}/s$: these growth parameters are compatible with post-process integration with Si CMOS integrated circuits.
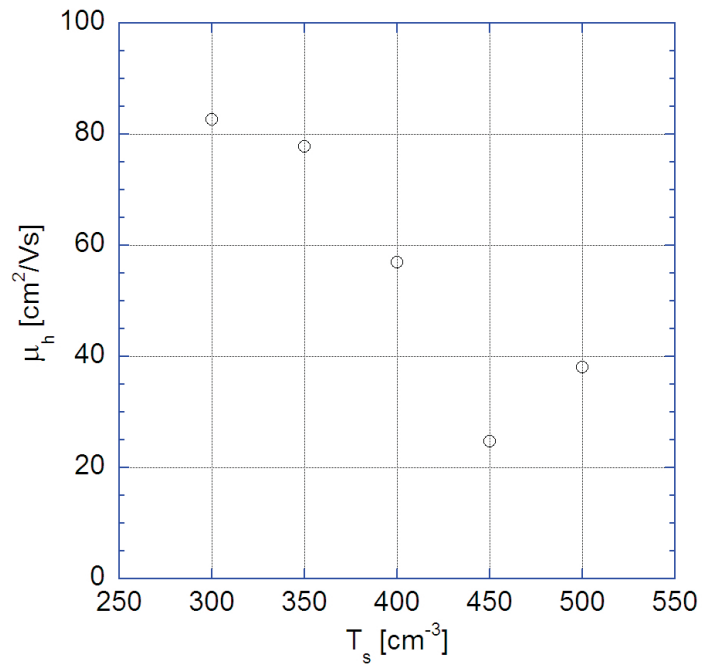
Figure 2.25: Mobility versus substrate temperature - Mobility of Ge evaporated on SOI versus substrate temperature

3

Germanium on Silicon Heterojunctions

This chapter is dedicated to the analysis of Germanium on Silicon heterojunctions. I report and discuss the conduction and collection properties of simple pn-junction devices for normal incidence NIR photodetection. In the first section I report the fabrication process of standard devices by optical lithography, Ge etching and contact definition. In the second section I address device characterization, the main parameters of photodetectors and the characterization set-up. Finally, I discuss the results obtained with evaporated Ge-on-Si devices, defining design strategies to exploit this material.

3.1   Fabrication

The realization of pn-junction devices begins with the evaporation of Ge on Si substrates, according to the process flow described in the previous chapter. The substrates are $< 100 >$ n-type Si wafers with resistivity of $1 - 3$ Ωcm. Small samples are cleaved from the wafer and subsequently cleaned with RCA and passivated with BOE solution. Ge is evaporated to the desired thickness, 200 nm in these devices, based on the optimal growth conditions identified in the previous chapter (substrate temperature $300°C$ and growth rate 2 $\mathring{A}/s$). The as-grown Ge-on-Si samples do not need polishing owing to the high smoothness revealed by AFM measurements.

The devices consist of simple square-mesas of six different areas, ranging from 60×60 μm^2 to 220×220 μm^2 in planar geometry, the top contacts provided with a wide window

to allow normal incidence illumination. The device geometries are defined by standard optical lithography. The photo masks were written on 4-inch Iron Oxide on glass photoplates produced by Towne Technologies Inc. The Iron Oxide is semi-transparent to visible light while completely opaque to UV, facilitating the alignment operations. The device fabrication starts with a photoresist coating on the samples: I used a general purpose positive photoresist of the *Megaposit SPR220* series. The coating is realized by spinning for $40s$ at 4000 rpm, aiming at a final thickness of 3 μm. A baking step for $90s$ on a hotplate held at $120°C$ follows. To transfer the geometry from the mask to the sample, I used the *Karl Suss MA6 Mask Aligner*, a top and bottom side contact printer used for fine lithography down to 1 μm or better. The *MA6* uses a Hg-bulb filtered to UV-wavelength of 365 nm, with typical exposure intensity of 25 mW/cm^2. Micrometric translation as well as rotational stages allow the exact alignment of the mask to the underlying sample. The exposure time ($20s$) varies depending on the applied photoresist. The photoresist development is performed by dipping the sample in an $NaOH$-based solution for a time depending on the thickness, about $40s$ for 3 μm. The developed photoresist is baked at $120°C$ for $90s$ to harden the leftover photoresist so it can withstand the subsequent etching of Ge. The mesas are defined by wet chemical etching of Germanium. Various etching recipes were tested, including standard hydrogen peroxide (H_2O_2) based solutions and standard metal etching as *Microposit Chrome Etch 18*. Finally, the best Ge etching in terms of repeatability and rate was a diluted solution of ortophosphoric acid, hydrogen peroxide and distilled water ($H_3PO_4 : H_2O_2 : H_2O$).

After Ge etching and photoresist removal, the metal is deposited on the samples by either thermal evaporation or sputtering. I adopted thermal evaporation. The contacts are defined by lift-off. Before placing the samples in the vacuum chamber, the contact pattern is defined on the *AZ5214*, a photoresist appropriately intended for this applications. This is a positive photoresist capable (under suitable conditions) of image reversal, resulting in a negative pattern of the mask. The image reversal capability is obtained by a special crosslinking agent in the composition; it becomes active above a threshold temperature around $110°C$ only in the exposed areas of the resist. The crosslinking agent together with an exposed photoactive compound lead to a nearly insoluble (in developer) and light insensitive substance, while the unexposed areas behave as a normal unexposed positive photoresist. After a flood exposure without mask, these areas are dissolved in a standard developer for positive photoresist. The overall

result is a negative image of the contact pattern. The contact pattern is defined by the following step. First, the photoresist is spun on the samples for $50s$ at 3000 rpm and baked before mask exposure for $210s$ at $90°C$. The samples are then loaded in the $MA6$ and, once the mesas and the contact pattern are aligned, the photoresist is exposed for only $2s$. At this point the image reversal is carried out by baking the photoresist for $90s$ at $120°C$ and exposing the sample to UV-light without mask for $20s$. The contact pattern is developed with the standard positive developer AZ 400 K.

The metal deposition consists in thermal evaporation of a double layer of chromium and gold. As discussed in the previous chapter, this metalization provides ohmic contacts on Ge, while chromium on n-type Si results in a Schottky barrier. Nevertheless, an ohmic-like behavior was observed, not affecting the device characteristics. During deposition, the sample is kept at ambient temperature in a vacuum atmosphere between 10^{-6} and 10^{-7} Torr, while the growth rate for both metals is of 2 $\mathring{A}/s$ up to a final thickness of 50 nm of Cr and 50 nm of Au. The lift-off consists in submerging the samples in Acetone till the photoresist removal was completed. Fig. 3.1 shows a micro photograph (a) and a schematic section (b) of the fabricated photodetectors. The cathode (on Si) is common to all devices while the anode (on Ge mesa) consists of a square frame, with one side wider than the others to allow electrical probing.
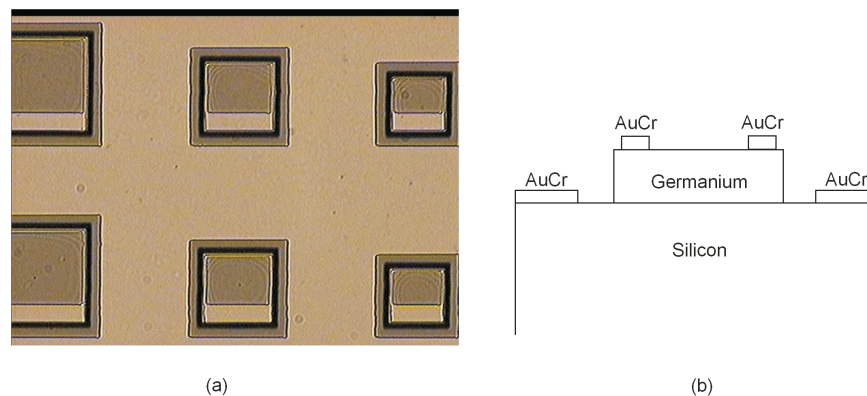

(a)   (b)

Figure 3.1: Ge-on-Si normal incidence photodetcors - (a) Optical microscope photo of normal incidence photodetectors. (b) Cross section of the devices

3.2 Device Characterization

The fabricated photodectors were characterized with the final aim of investigating the electronic properties of evaporated Ge-on-Si heterostructures as well as the incapabilities to operate as NIR photodectors. I was interested in understanding how much the quality of the material affects the optoelectronic properties of these heterojunctions and how this approach can be compared with others such as UH-CVD, MBE and so on.

As discussed in the first chapter, the main figures of merit for photodetectors are the dark current density, the responsivity and the dynamic properties affecting detection speed. The next sections will focus on these aspects.

3.2.1 Current-voltage characteristics

The theory of homojunction currents can be found in any book concerning electronics (2). Here I will briefly discuss the mechanisms involved in carrier transport across heterojunctions, defining the main contributions to Ge-on-Si dark currents.

Unlike the Schokley homojunction, no complete model is able to explain all the physical phenomena involved in heterojunction currents. This is mainly ascribed to hetero-interface properties varying with the fabrication as well as the materials. It is important to develop time by time the best model fitting the experimental data. Here I briefly summarize the most important transport models; an in-depth analysis can be found in (56).

The energy band model for ideal abrupt p-n heterojunction was proposed by Anderson (57). Based on his theory, the band profiles depend on the electron affinities χ, the energy band-gaps E_g and the work functions ϕ of the two materials and are classified into four main cases. The typical energy band profile of an abrupt p-Ge on n-Si heterojunction is shown in fig. 3.2 (56; 58). The main difference with a typical homojunction band profile consists in the discontinuity of the conduction band edge. The latter has an important role in the conduction mechanisms at the interface, with the *spike/notch* boundary acting as a barrier for electrons flowing from Ge to Si.

However, this model neglects the contribution arising from interface states due to the defected crystalline structure at the heterojunctions. If the effects of interface states is taken into consideration, then the band profiles are modified depending on the charge
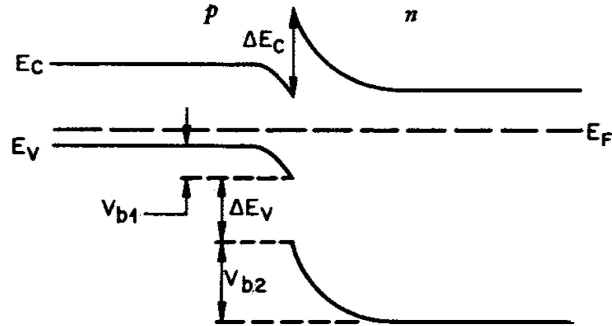
Figure 3.2: _pn_ heterojunction energy band profile - Typical energy band profile of _p_-type Ge on _n_-type Si

of the state. In evaporated Ge thin films, the defects exhibit an acceptor-like behavior, and the modified band diagram can be modeled as in fig. 3.3 (56), because of the high misfit-dislocation density at the interface.
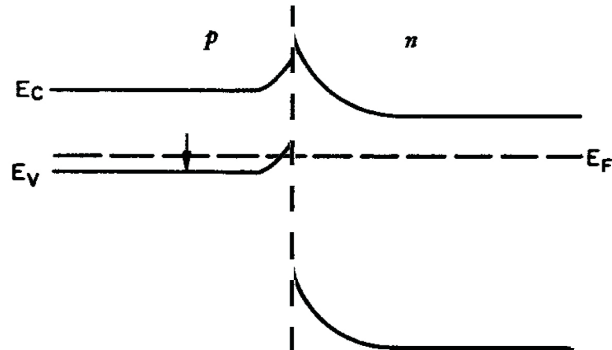
Figure 3.3: Modified _pn_ heterojunction energy band profile - Modified energy band profile of _p_-type Ge on _n_-type Si due to the presence of acceptor-like interface states

In this case the conduction band exhibits a barrier (spike) for electrons in both directions. This barrier can be effectively active, letting the junction current follow three possible models: the diffusion model neglecting the spike contribution (57), the emission model considering the spike as in Schottky junctions (59), the tunneling model threating the tunnel effect at the barrier (60). Despite these cited models, none of them can fully explain the experimental data from Ge-on-Si heterojunctions. In 1966

Donnelly and Milnes (61) studied this problem on Ge-on-Si *pn* heterojunctions and concluded that recombination and tunneling currents, related to the interface states, play a dominant role in this p-n heterojunctions. A complete investigation of the involved phenomena would require a more detailed theoretical and experimental engagement, and work is still in progress worldwide.

The current-voltage (*I-V*) measurement set-up is of an automatic acquisition system composed by a calculator GPIB interfaced with a voltage source and picoammeter, the *Hewlett-Packard HP4140B*. By means of internal switches it is possible to activate the voltage across the device and monitor the current flowing while sweeping the bias. A micro-probe is necessary to contact the small area devices: I used a GSG (*ground-signal-ground*) probe terminated by an SMA connector.

From the current-voltage characteristics it is possible to extract several important parameters affecting the photodetectors: dark current, ideality factor, series and shunt resistances. The dark current is crucial as it affects the sensitivity in terms of SNR (signal to noise ratio) and NEP (noise equivalent power). The most important noise source in photodectors is the shot-noise from currents flowing in them; because detectors work in reverse bias, the shot noise depends on the sum of photo and dark currents, according to:

$$\left\langle i_s^2 \right\rangle = 2q\Delta\nu \left(I_{ph} + I_d \right) \tag{3.1}$$

where $\left\langle i_s^2 \right\rangle$ is the shot-noise mean value, q the electron charge, $\Delta\nu$ the bandwidth, I_{ph} and I_d the currents flowing in the device. It is important to keep the dark current low in order to increase the sensitivity. The ideality factor is also an important figure. Although it is hard to associate a transport mechanism to the observed characteristic, the ideality factor gives an idea of the interface quality: the closest the ideality factor to unity the least the defects affect conduction. Finally, the series resistance is relevant for the small-signal circuit and the extrinsic temporal response, as discussed in the first chapter.

Dark current

Fig. 3.4(a) shows current densities versus reverse bias at room temperature. The devices (Ge grown at $300°C$ and 2 $\mathring{A}/s$) exhibit typical dark current densities in the

range 2-3 mA/cm^2 at $1V$ reverse bias. The observed density compares well with the best results reported in literature (62) for Ge-on-Si photodetectors. This reflects the high dislocation density of the material. Considering generation processes assisted by deep levels related to threading dislocations, a direct a correlation between dark current densities and threading dislocations was demonstrated in (63). Fig. 3.4(b) shows the linear scaling of dark current at 1 V reverse bias versus device area, suggesting negligible surface leakage with a dominant volume conduction. The dark current densities versus device temperature were studied to investigate the main conduction mechanism.
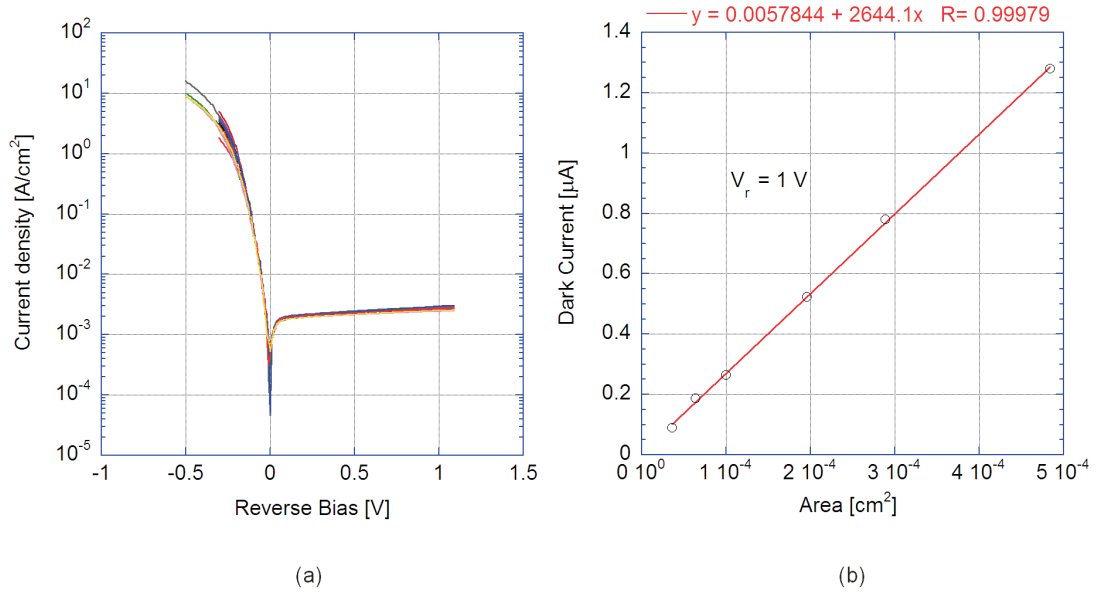
Figure 3.4: *J-V* **characteristics of Ge-on-Si *pn* junctions** - (a) Typical current densities of Ge-on-Si *pn* junctions versus reverse bias at room temperature. (b) Typical dark current versus device area at 1 V reverse bias

Fig. 3.5 graphs the current-voltage characteristics at temperature ranging from 200 to $310K$. The characteristics suggest different contributions to the dark current, its increase ascribed to a growing hole concentration at high temperatures. Fig. 3.6 displays the Arrhenius plot of the dark current densities at various reverse biases versus $1/kT$. The plot shows that the conduction mechanisms do not satisfy the simple generation/diffusion model.
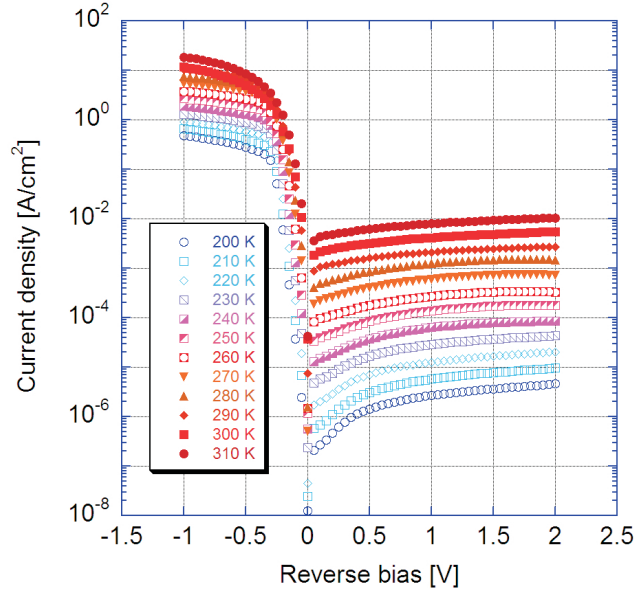
Figure 3.5: *J-V* versus temperature of Ge-on-Si *pn* junctions - Typical current-voltage characteristics at temperatures ranging from 200 to $310K$.
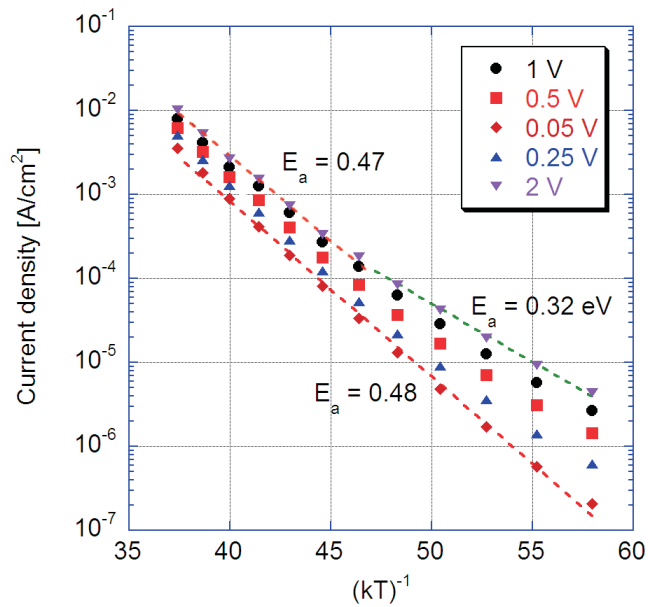
Figure 3.6: Arrhenius plot of dark current densities of Ge-on-Si *pn* junctions - Arrhenius plot of the dark current densities for different reverse biases

In fact, according to the diffusion model the dark current should be proportional to the intrinsic carrier concentration if dominated by generation in the space charge region, whereas it should scale with the square of the intrinsic concentration if diffusion prevails. In such conditions:

$$J_d \approx T^{\frac{3}{2}} e^{\frac{E_g}{2kT}} \tag{3.2}$$

for generation in the space charge region, and:

$$J_d \approx T^3 e^{\frac{E_g}{kT}} \tag{3.3}$$

for diffusion, where k is the Boltzmann constant, T the temperature in Kelvin and E_g the energy band-gap. Since the power dependence is negligible as compared to the exponential term, the analysis could be performed by fitting the experimental data in the Arrhenius plot with a single exponential function and studying the associated activation energy E_a. Fig. 3.6 shows that the activation energy depends on both applied voltage and temperature. In both cases the activation energy differs from the energy band-gap of Germanium and Silicon (0.67 eV and 1.12 eV), suggesting that no diffusion currents are involved at the interface. Nevertheless, the estimated activation energies (0.48 eV at high temperatures, 0.32 at low temperature and high bias) do not match either with the middle-gap energies of the two materials. This would also exclude the generation in the space-charge region. It is clear that the temperature dependence of dark currents is affected by phenomena with a more complicated temperature behavior. In such conditions, the correct interpretation of fig. 3.6 requires more exhaustive knowledges of the band profile and the defect states at the interface. At the moment, we can only conclude that the dark current is affected by defect-assisted conduction with activation related to both temperature and voltage. At high temperatures ($\geq 260K$ corresponding to about 45 in the Arrhenius plot) the activation energy is only slightly affected by the applied voltage, while at low temperature the activation energy is voltage dependent and varies by more than 30%. The change with reverse bias is consistent with an energy distribution of interface defects around the mid-gap of Ge and their voltage-dependent activation/deactivation, but the larger variation at

low temperatures is not clear. Accurate studies of these aspects are in progress.

The dark currents were also measured in different samples grown at various substrate temperatures (from $300°C$ to $500°C$) and growth rates (0.2, 2.5 and 20 $\mathring{A}/s$). Fig. 3.7 plots the observed results at $300K$.
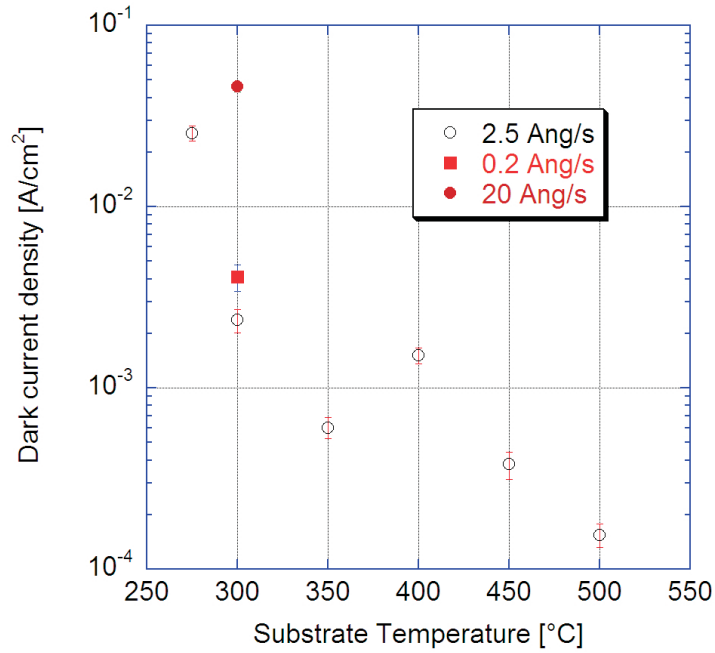
Figure 3.7: Dark current densities of Ge-on-Si *pn*-junctions versus growth parameters - Dark current densities at 1 V reverse bias versus substrate temperature and various growth rates

The dark current density decreases with increasing temperature, while increases for fast growth rates. It is worth to note that, even if a decreasing dark current should be desirable, this is not necessarily associated to a better performance of the photodiode. This reflects the results of the Hall characterization. In particular, as the device suffers from defect-assisted tunneling at the highly defected Ge/Si interface, the dark current is highly sensitive to defect properties in terms of: concentration, associated energy levels in the Ge bandgap and trapping-emission rate. From Raman and X-Ray analyses it emerged that Ge films have a non monotonic behavior (first decreasing, then increasing defect density with temperature). If the dark current, as well as the electronic properties, were to depend only on defect concentration, we would

expect the same trend in the electrical characteristics; this does not happen because the defect energy levels in the Ge band-gap are crucial. Unfortunately, as discussed about the Hall measurements, the correct interpretation of such phenomena requires an extensive material characterization by means of DLTS or EBIC techniques. Moreover, the high equivalent doping of evaporated Ge makes also difficult this kind of analysis. In fact, since DLTS is based on capacitance measurements, it is difficult to prepare *pn* or Schottky junction samples to perform such characterization. Future works involve a specific study on how to investigate defects in evaporated Ge thin film. I suggest (to be confirmed by experimental data,) that a migration of energy levels towards the mid-gap of Ge takes place at increasing temperatures which are also associated to a decreasing trapping-emission rate. This would explain the increasing trapping of defects which causes a worsening of the conduction properties.

Ideality factor and series resistance

As discussed earlier, various transport mechanisms affect the current-voltage characteristics of heterojunction diodes and it is not easy to define a single closed-form expression. All models exhibit a similar voltage-dependence in forward bias, as expressed by the diode expression:

$$I_f = I_0 e^{\left(\frac{V - R_s I_f}{\eta V_T}\right)} \tag{3.4}$$

where I_0 is a weak function of voltage depending on the conduction mechanisms, R_s is the series resistance, η is the ideality factor and V_T is the thermal voltage (25 mV at room temperature). R_s indirectly affects the forward current as it acts as a feedback on the diode operating point. Solving eq. 3.4 for the voltage bias yields:

$$V = R_s I_f + \eta V_T ln\left(\frac{I_f}{I_0}\right) \tag{3.5}$$

which can be used to fit the experimental data and calculate the series resistance and the ideality factor. The analysis of the fabricated samples provided an ideality factor close to unity, with typical values in the range 1-1.2. This is associated to a

dominant Si recombination current in the substrate, as already demonstrated by Donnelly and Milnes (61).

The series resistance of the devices versus mesa width is plotted in fig. 3.8.
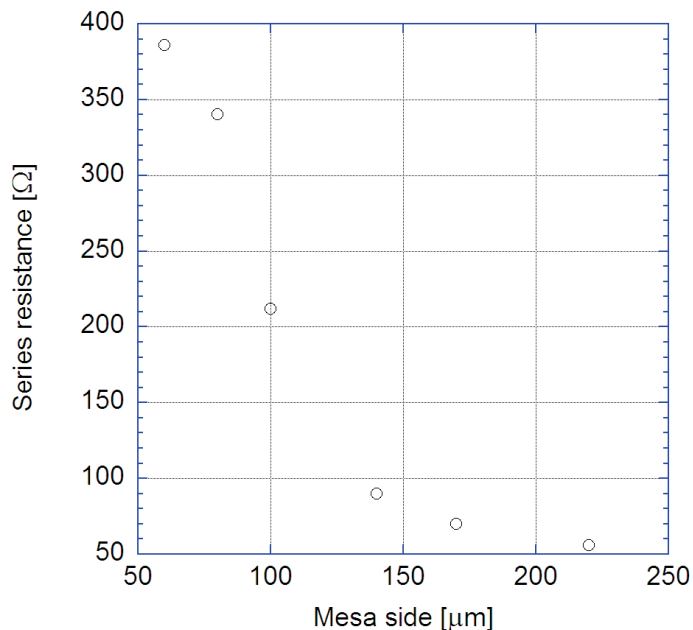
Figure 3.8: Series resistance of Ge-on-Si *pn* junctions - Series resistance versus mesa width

R_s arises from the higher resistivity of the Si layer (1-3 Ωcm with respect to 0.2 Ωcm in Ge). The resistance depends on two material regions: the Si volume interested by current flow under the Ge mesa and Si volume linking the Ge mesa with the cathode contacts. In both cases the series resistance is a function of the inverse of the mesa side, as pointed out by the experimental data ranging from 60 Ω of larger-area to 800 Ω of smaller-area devices.

From the reverse bias *I-V* characteristic we could calculate the shunt resistance R_{sh}, which is the derivative of the voltage drop versus current in reverse bias. This parameter depends on the conduction mechanisms involved in the reverse current, so it is area-dependent as visible in fig. 3.9 showing typical shunt resistances of devices versus the junction area. R_{sh} values are in the range 1-10 $M\Omega$ as expected from theory.
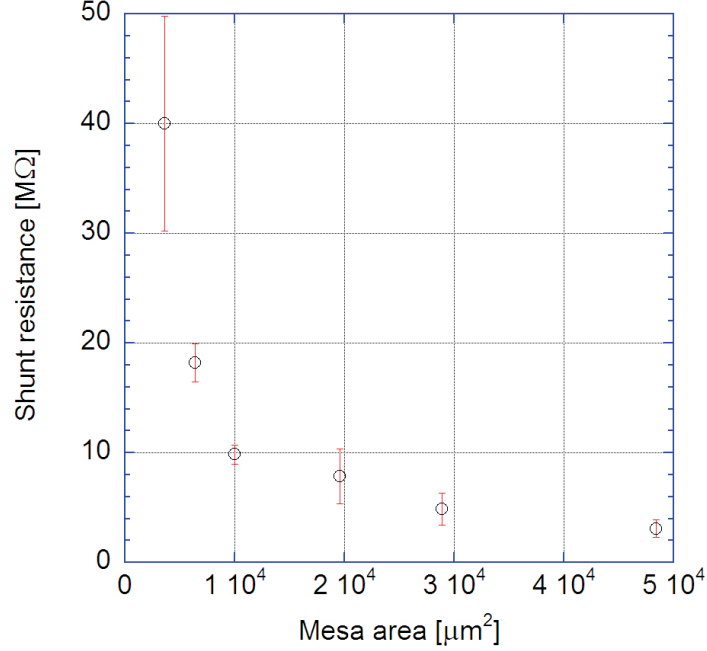
Figure 3.9: Shunt resistance of Ge-on-Si *pn* junctions - Shunt resistance versus mesa area

3.2.2 Responsivity

Responsivity is the figure of merit on conversion efficiency. It quantifies the photocurrent I_{ph} producted by a photodector when illuminated by a light signal of power $P_{in} = 1$ W. The photocurrent I_{ph} depends on the collected carriers generated within the space charge region and in a diffusion length near it. It is worth to note that, because of the unbalanced doping of Si with respect to evaporated Ge (10^{15} cm^{-3} versus 10^{17}-10^{18} cm^{-3}), the space-charge region extends entirely in Si, while the diffusion length of minority carriers in Ge depends on the highly defected structure and the consequent trapping phenomena. These deteriorate unavoidably the performance of normal incidence photodetctors through a low absorption efficiency.

The responsivity is evaluated by measuring the device photocurrent with a current-voltage converter and a lock-in amplifier to cancel the dark current contribution. A laser source at 1.55 μm produces the input light beam, focused by lenses on the top of the Ge mesa within the input window. The input beam is modulated by a chopper. The modulated photocurrent is collected by the GSG probe and converted in a photo-

voltage signal by an adjustable transimpedance amplifier (TIA), the latter capable of biasing the device with an external voltage. The TIA output is demodulated by the lock-in amplifier and acquired by a calculator for data acquisition.

Fig. 3.10 shows the measured responsivities versus reverse bias, with typical values ranging from 1 to 2 mA/W at 1 V reverse bias and 1.55 μm.
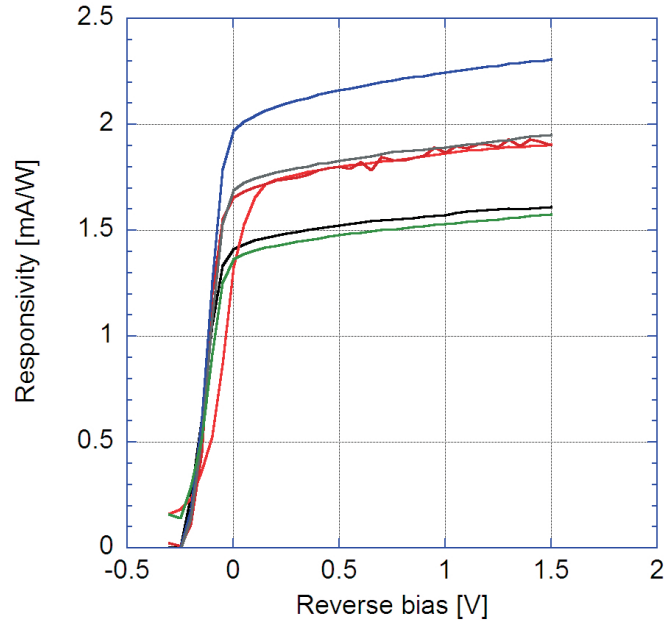
Figure 3.10: Normal incidence responsivitiy of Ge-on-Si *pn* junctions - Responsivities versus reverse bias

As expected, the responsivities are rather low because of the highly defected Ge. From eq. 1.2 and eq. 1.3, it is possible to estimate the active absorption layer:

$$R = \eta_c \frac{\lambda}{1.24} \left(1 - \Theta\right) \left(1 - e^{-\alpha(\lambda)d}\right) \tag{3.6}$$

where the $(1 - \Theta)$ term accounts for the reflection at Ge/air interface. The active absorption layer is:

$$d = -\frac{1}{\alpha} ln \left(1 - \frac{1.24R}{\eta_c \lambda \left(1 - \Theta\right)}\right) \tag{3.7}$$

assuming a typical absorption coefficient of Ge thin films (64), the active layer is estimated in the range 10-100 nm depending on the collection efficiency η_c. The devices exhibit large short-circuit photocurrents with a maximum responsivity at zero bias. This is commonly associated to efficient collection properties, therefore we can estimate a collection efficiency near unity.

With these collection conditions, the active layer can be estimated in about 25-30 nm; since the space-charge region in Ge is about 1 nm, the effective layer coincides with the diffusion length L_n of the minority carriers. These results are validated by studying the voltage dependence of responsivity. Fig. 3.11 shows an example of normalized responsivity compared with the absorption term $(1 - e^{(-\alpha d)})$, where d is the is the sum of the estimated diffusion length L_n and of the depletion region (voltage dependent) in Ge, α is the absorption coefficient at 1.55 μm (64).
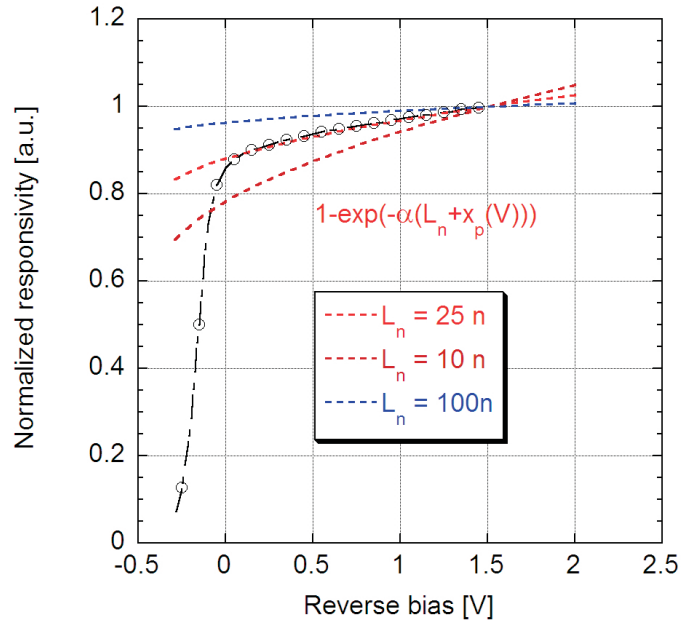
Figure 3.11: Normalized responsivity of Ge-on-Si pn junctions - Normalized responsivity (black line) compared to the absorption term (red dotted line) depending on the depletion region in Ge

The collection efficiency is taken equal to one and independent on the voltage. The figure shows different trends of the absorption term for different diffusion lengths. The normalized responsivity is well interpolated by the estimated diffusion length of 25 nm.

This confirms the good collection. The estimated L_n is rather short with respect to typical diffusion lengths of epitaxial Ge films grown by MBE or UH-CVD (typically tens of microns); this is ascribed to the highly defected interface between Ge and Si.

It is possible to conclude that evaporated Ge-on-Si detectors exhibit good detection properties but the high effective doping and short minority-carrier diffusion-length make these devices unsuitable for normal incidence. By adopting waveguide approaches however, it would be possible to exploit the good collection properties and avoid the limitations due to the short active layer (this will be discussed in the next chapter).

The NIR spectral response was investigated by illuminating the photodetectors with the light filtered by a monochromator. Fig. 3.12 shows the responsivity versus wavelength at zero and 5 V reverse bias.
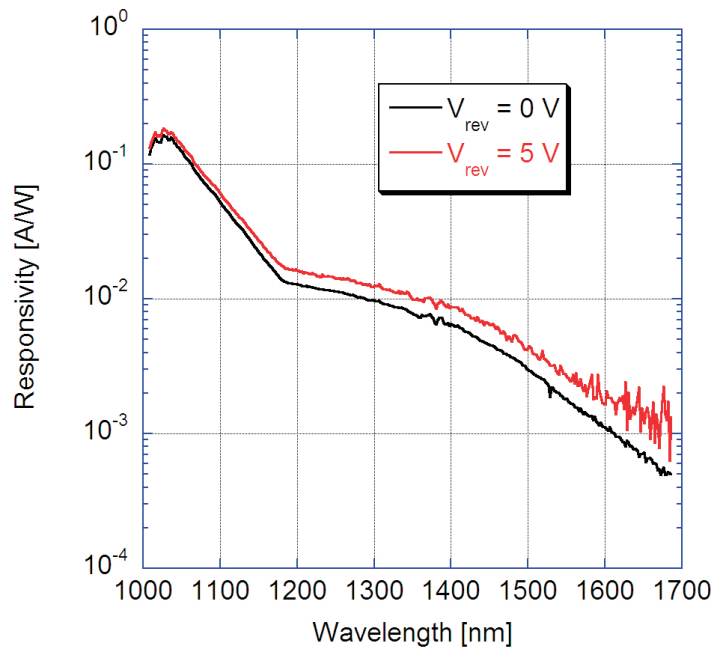
Figure 3.12: Spectral responsivity of Ge-on-Si *pn* junctions - Responsivity versus wavelength at different reverse biases for normal incidence Ge-on-Si *pn*-photodetectors

The spectral response follows the absorption spectrum of Ge (64). At wavelengths longer than the cutoff ($\approx 1.58 \ \mu m$), the responsivity does not decrease as sharply as the absorption, but exhibits a slow reduction. This is attibuted to multiple reflections within the air/Ge/Si/air system at those wavelength where Ge absorption is drastically

low. It is worth to observe the small difference between zero and 5 V reverse bias in the whole range of wavelengths, this confirm the near optimal collection properties of devices.

The responsivities of samples grown in different conditions were also investigated. Fig. 3.13 shows the responsivities of samples realized at different substrate temperatures and growth rates.
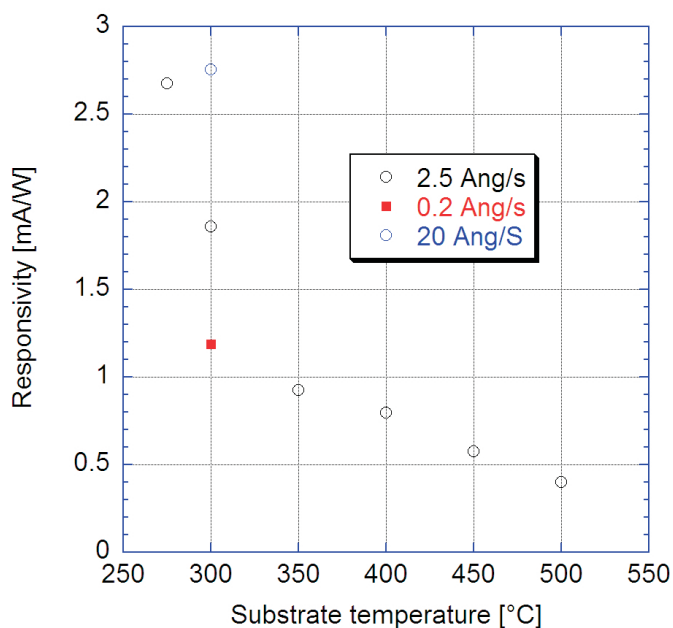
Figure 3.13: Responsivity versus growth parameters - Responsivity at 1 V reverse bias versus substrate temperature at different growth rates for normal incidence Ge-on-Si *pn* photodetectors

A decreasing trend can be observed, similar to dark currents (fig. 3.7) but less marked. This is probably associated to a slight change in the minority-carrier diffusion-length due to the band alignment and re-distribution of the defect energy levels. As described in the previous section, the band profile is expected to have a pinning at the conduction band acting as a barrier for the electrons. Since at increasing temperatures the unintentional (equivalent) doping increases (fig. 2.24), the barrier pinning is expected to be stronger and increase the barrier-height at the conduction band. At the same time, an increasing defect-density is associated to more interface defect states, the latter acting as traps for the photogenerated carriers. These phenomena probably

contribute to the reduction in responsivity versus temperature. Fig. 3.14 shows the photocurrent (fig. 3.13) versus dark current (fig. 3.7). Photocurrent increases linearly with the dark current, demonstrating that the photocurrent is limited by the same mechanisms affecting the dark current.
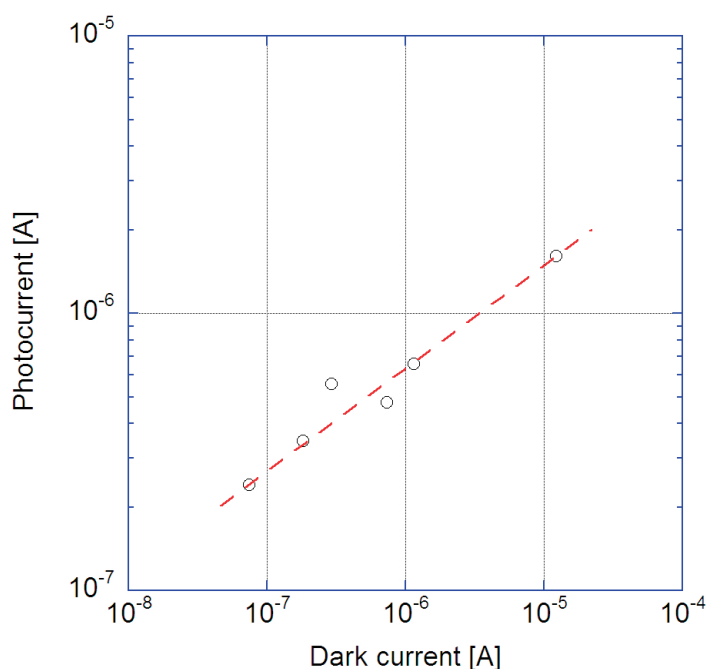
Figure 3.14: Photocurrent versus dark current - Photocurrent at 1 V reverse bias versus dark current in various normal-incidence Ge-on-Si *pn* photodetectors

In conclusion, reverse currents flowing across the junction (both photo and dark currents) are limited by transport mechanisms not associated to standard generation/recombination models. The main phenomenon is probably the trap-assisted tunneling due to interface states. These effects are strictly related to the Si/Ge interface quality and are relevant when the defect-density increases. This is not supported by morphological characterization, but is consistent with Hall measurements. In order to better understand such phenomena and how the structural properties affect carrier transport, we need to extensively study the electric properties of defects and their activation both versus temperature and voltage. These aspects are still under investigation.

3.2.3 Time response

This section is dedicated to the dynamic properties of the photodetectors. As discussed in the first chapter, the temporal response is affected by drift, diffusion (intrinsic response), junction capacitance and series resistance (extrinsic response). The first analysis was conducted on device capacitance to evaluate the extrinsic frequency cutoff. The capacitance-voltage (C-V) measurements were performed with the impedance analyzer *HP 4192A*. The measurement consists in the application of a small signal of frequency varying in the range $10Hz$-$1MHz$ superimposed on the bias voltage and in the extraction of the impedance characteristics. Fig. 3.15 shows the $C - V$ data at reverse bias for devices of different areas and the theoretical curves obtained from the expression of a *pn* abrupt heterojunction capacitance (2):

$$C = \sqrt{\frac{q\epsilon_{Si}\epsilon_{Ge}}{2} \frac{N_a N_d}{(\epsilon_{Si}N_d + \epsilon_{Ge}N_a)(\phi_i - V)}} \tag{3.8}$$

The experimental data are in good agreement with the calculations.

With the capacitance data, the equivalent small-signal circuit (fig. 1.5) is completed. By combining the resistance data extracted by $I-V$ characteristics, the extrinsic cutoff frequency is then calculated according to eq. 1.9, with a load resistance R_{load} of 50 Ω:

$$f_L = (2\pi(R_s + R_{load})C_j)^{-1} \tag{3.9}$$

where the large shunt resistance R_{sh} is not considered. Fig. 3.16 shows the calculated RC cutoff frequency versus reverse bias. The calculated cutoff frequencies range between the 100 MHz for larger device and the 800 MHz for smaller device at 1 V reverse bias, increasing with voltage towards a maximum of 2 GHz for the smallest detector at 10 V reverse.

The time response was investigated by illuminating the photodetectors with picosecond light pulses and registering the time-resolved response with a high-bandwidth digital oscilloscope (Tektronik CSA 803C).

The setup involves a Pritel picosecond fiber-laser at 1.55 μm, amplified by an optical fiber amplifier to provide a larger signal. The photocurrent is converted in a voltage by
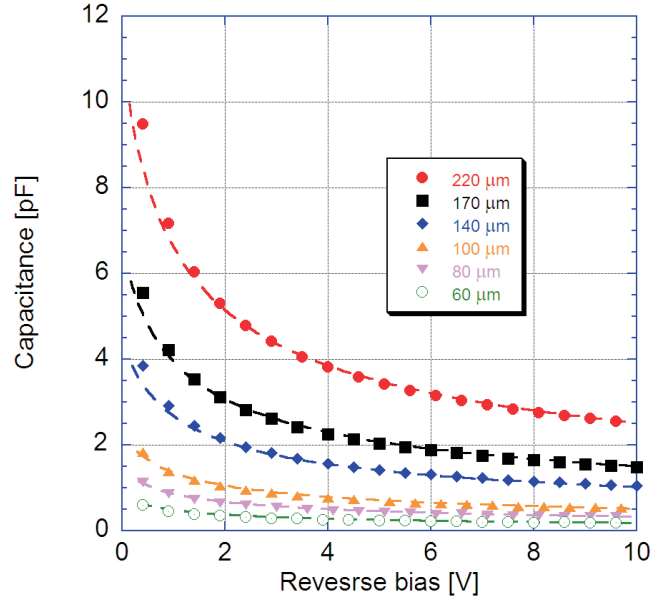
Figure 3.15: Capacitance versus reverse bias of Ge-on-Si *pn* junctions - Capacitance versus reverse bias. The dashed lines represent the estimated junction capacitance according to eq. 3.8
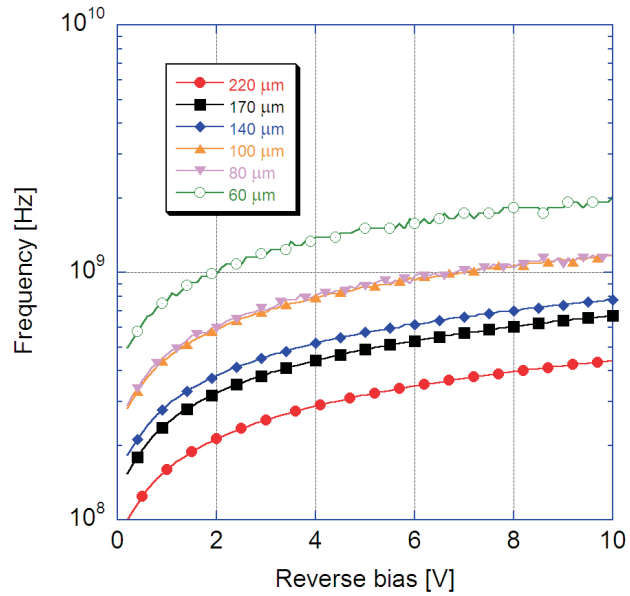

Figure 3.16: RC cutoff frequency of Ge-on-Si *pn*-junctions - Extrinsic RC cutoff frequency evaluated according to eq. 3.9 versus reverse bias

the low input resistance (50 Ω) of the digital oscilloscope. A bias-tee is inserted between the instrument and the photodetector to filter out the lowest frequencies, namely the constant dark current, and to provide an external reverse bias to monitor the temporal response versus bias. Fig. 3.17 shows the normalized pulse response of a 100 μm device at various reverse biases.
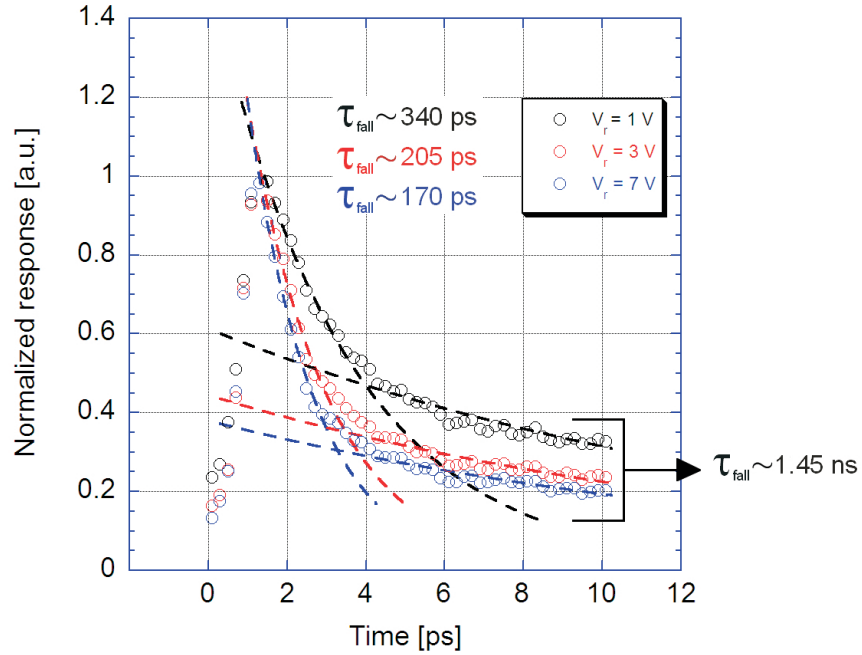
Figure 3.17: Pulse response of Ge-on-Si pn junctions at different biases - 100 μm Ge-on-Si pn-junction response to an incident fast pulse (1 ps) at different reverse biases. The response exhibits an exponential decay governed by two time constants: the slower (1.45 ns), bias independent, is due to diffusion in Ge; the faster, voltage dependent, is associated to the RC constant

The response is the superposition of different exponential decays with characteristic times extracted by a fit with two terms. The results are plotted in fig. 3.17: the faster response is clearly voltage-dependent and scales from 340 ps at 1 V reverse down to 168 ps at 7 V reverse, while the slower term seems not affected by the applied reverse bias and is about 1.45 ns. This is explained by the different dynamics of the photodetectors: the slower decay is associated to diffusion in Ge, not affected by the applied voltage; the faster response is related to the extrinsic RC of the pn junction. In fact, the extracted

time constants compare well with the calculated RC constants obtained for the 100 μm device. Fig. 3.18 displays the pulse response of a 220 μm device at 7 V reverse. The fast RC response compares well with the calculated values, while the slow diffusion term exhibits a time constant of 1.65 ns. Fig. 3.19 shows the fast Fourier transform (FFT) of the pulse response of fig. 3.18: the 3 dB frequency is limited to 110 MHz due to a diffusion limited frequency response. As carrier generation occurs only in Ge, the diffusion limitation is associated to the minority carrier lifetime in Ge, estimated in in the range 1÷2 ns. These value are comparable with previously reported results (4).

	Value	Error
m1	2.0645	0.034244
m2	3.9464e-10	1.1055e-11
m3	0.30771	0.026858
m4	1.644e-09	8.1876e-11
Chisq	0.5424	NA
R	0.99328	NA

$$y = m1*e^{(-t/m2)} + m3*e^{(-t/m4)}$$

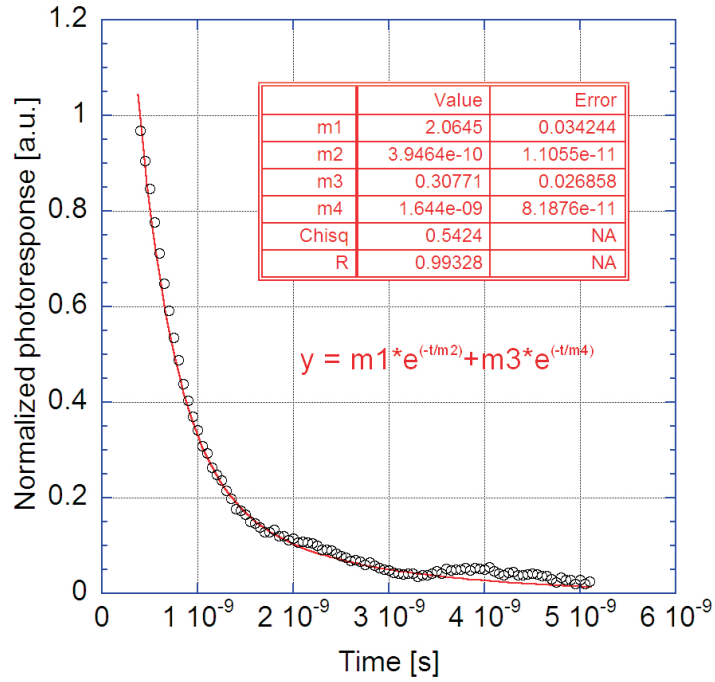**Figure 3.18: Pulse response of Ge-on-Si *pn* junctions** - 220 μm Ge-on-Si *pn* junction response
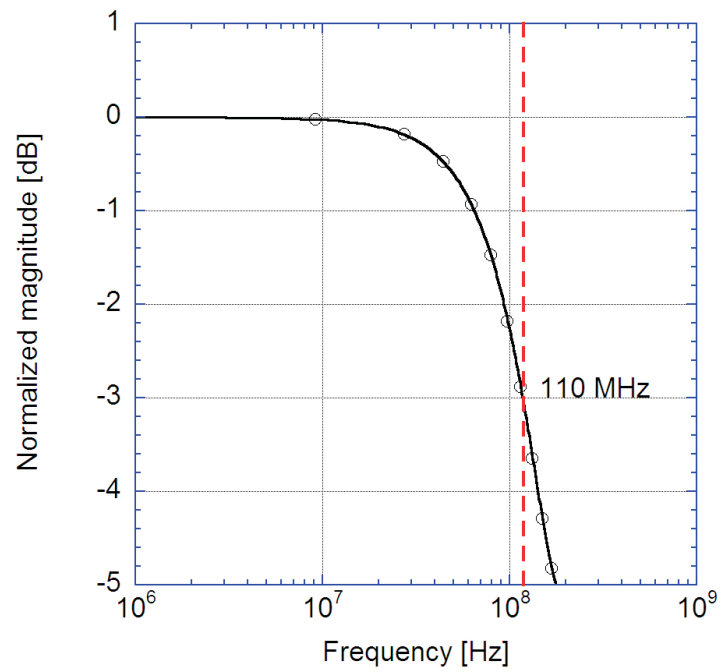
Figure 3.19: Fast Fourier transform of the pulse response - The pulse response FFT emphasizes a limited bandwidth not affected by reverse bias, associated to diffusion mechanisms in Ge

3.2.4 Conclusions

Evaporated Ge-on-Si heterojunctions were fabricated for normal incidence NIR detection. The photodetectors exhibited typical dark currents densities of 2 mA/cm^2, among the lowest reported in literature. The temperature analysis pointed out a trap-assisted tunneling current in the Ge film dominating the diffusion current of the Si side at room temperature. The analysis of the photodetectors demonstrated that the dark currents of devices fabricated at different temperatures decrease for increasing substrate temperatures, explained in terms of conduction band pinning and interface state distributions. In fact, more defected crystalline structures exhibit higher concentrations of acceptor-like levels, probably associated to a stronger pinning at the conduction band, and consequently to a higher barrier hindering the electron flow across the junction.

The optical response was investigated in terms of responsivity and speed. The photodetectors exhibit good collection properties manifested by short-circuit photocurrents approaching the maximum responsivity of 2 mA/W at 1.55 μm. The poor responsivity is explained in terms of short effective absorption length arising from the small extension of the space charge region in Ge and from the short diffusion length (25 nm). These properties encourage to adopt guided-wave detection approaches rather than normal incidence.

The dynamic properties of devices were studied in terms of $C-V$ characteristics and pulse response. The temporal response is limited to about 110 MHz by diffusion mechanisms associated to the short lifetime of Ge minority carriers.

4

Guided-wave Photodetectors in Germanium Deposited on Silicon-on-Insulator

The NIR detection and electronic properties of Ge evaporated on Si at low temperature stimulated interest towards this technique. The low cost and the good CMOS process compatibility make thermal evaporation of Ge a very promising solution for monolithic integration of near infrared detectors with standard Silicon technology for signal acquisition, amplification and processing. The viability of such approach was demonstrated in 2002 when our group began to investigate the post-process integration of an array of 8 evaporated Ge NIR photodectors on Si CMOS readout electronics (29). The results encouraged further developments until, in 2007, our group realized the first NIR digital camera based on the monolithic integration of a two-dimensional array of 512 Ge pixels on Si with A/D conversion, processing and readout. These demonstrate the effectiveness of thermal evaporation as a post-process deposition of Ge on pre-existing Si integrated-systems (both electronic and optic), encouraging towards the investigation of other applications (39). Among all, integration of evaporated Ge for optical fiber communications would represent a breakthrough towards a considerable knock-down of production costs. This challenging aim drove to the investigation of evaporated Ge photodetectors for NIR communications; in 2004 our group started a collaboration with an industrial partner, Pirelli Labs. Within a large industrial project, we aimed at fabricating NIR photodectors monolithically integrated on optical add/drop multiplexing

(OADM) chips for metropolitan communication networks, where evaporated Ge photodectors would serve as in-line power monitors on different communication channels. Power monitors are usually available as individual modules connected by patching fibers or as hybrid components locally bonded to optical terminations. Monolithic integration could naturally offer a compact, more inexpensive and more reliable solution.

Preliminary studies involved stand-alone detector design and fabrication on compatible substrates. The integration on an OADM chip, where signals travel on Si on Insulator (SOI) waveguides, suggested an easily integrable waveguide photodector (WPD) geometry. The first-generation devices gave promising results (38), with responsivities as high as 80 mA/W at 1.55 μm and demonstrated operation at 2.5 Gbit/s. These results encouraged new developments, in particular the adoption of more suitable substrates, because the electronic nature and the optical multimodality of the adopted SOI (Si overlayer of resistivity 12 Ωcm and thickness 3 μm) rendered the structures too lossy and unpractical for waveguiding. During my PhD I was involved in device design and optimization, performing accurate simulations of the optical and electronic properties as well as fabrication and characterization. The devices were finally tested on SOI optical chips with waveguides and tapers. I demonstrated the operation of power monitors obtained by a simple and low cost technique.

This chapter is divided into four main sections: the first is dedicated to the new design by simulations. Section two focuses on stand-alone devices fabricated on SOI as prototypes for the successive integration of power monitors on SOI chips. The third section regards the fabrication of WPDs on test chips consisting of several Si waveguides provided with bends and tapers. Finally, the last section is dedicated to the performance analysis of power monitors.

4.1   Device Design and Simulation

The device design was based on the geometry adopted in (38) and shown in fig. 4.1(a). It consists of a rib Ge waveguide on SOI in which the guided-mode is confined horizontally by the Ge ridge and vertically by the metal-Ge-Si heterostructure.

NIR detection stems from the leaky modes propagating in the lossy waveguides. The guided light overlaps with Si as well as Ge layers, being effectively absorbed only in the active Ge layer whose thickness depends on the thin depletion region (from the high
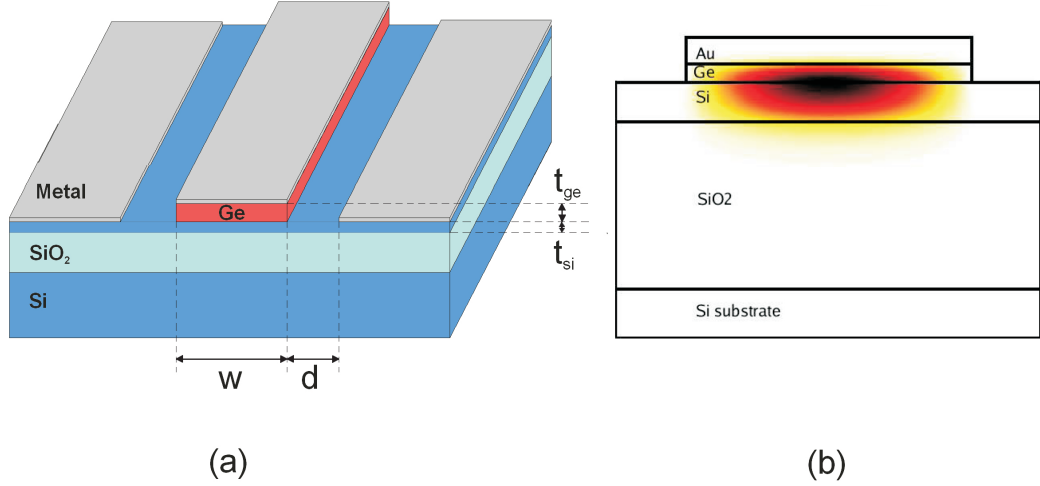
78

Figure 4.1: Guided-wave photodetector - (a) The guided-wave photodetector consists of a rib Ge waveguide on Silicon-on-Insulator provided with metal contacts for photocurrent collection.(b) Schematic cross section of the device with a sketch of the optical mode.

Ge equivalent doping) and on the short diffusion length of evaporated Ge. The carriers photogenerated outside the active layer recombine before reaching the metal contacts. The top metal introduces optical losses along the ridge waveguide. Fig. 4.1(b) shows a cross section of the guided-wave device with indication of the lowest-order optical mode.

The design spefications were imposed by the chip fabrication. In particular, to realize efficient Si waveguides it is crucial to employ semi-insulating SOI substrates to minimize the optical losses; moreover, the overlayer thickness should allow monomode propagation. Consequently, we employed lightly n-doped SOI substrates (resistivity 10-30 Ωcm) with a Si overlayer thickness of 220 nm. With respect to previous designs (38), the Si thin layer significantly changed the modal transverse profile and the absorption efficiency. Moreover, since the carriers must travel across a more resistive layer, the junction bias and the collection efficiency needed a careful analysis as the electric field distribution involves nonscalar effects. Thereby it was necessary to resort to simulations of the optical and electric properties to optimize both absorption as well as electric collection.

4.1.1 Simulation of the Electric Properties

Simulation of the electric properties were performed with ISE-TCAD, a 3D semiconductor simulation tool produced by Synopsys. The main tool of TCAD is DESSIS, a multidimensional, electrochemical, mixed mode device and circuit simulator for semiconductor devices. It incorporates advanced physical models and numerical methods for several semiconductor problems from sub-micron MOSFETS to large bipolar power structures. In addition, it supports heterostructure simulations, providing a large material library comprising Ge. This powerful tool was employed for simple electrostatic 2D simulations of WPD structures to evaluate the electric field distribution in the very thin Si layer under the Ge waveguide and the effects on collection efficiency.

The simulated heterostructure was as fig. 4.1 with default dimensions stemming from the available lithographic facilities (it is critical to define sub-2 μm details with adequate repeatability). The default dimensions were $w = d = 10$ μm and $t_{ge} = 100$ nm. The electric parameters were imposed by the materials: Si with high crystalline and electrical properties, resistivity 10-30 Ωcm corresponding to $N_d = 1.5\text{-}4 \cdot 10^{14}$ cm^{-3}, Ge highly defected with resistivity 0.2 Ωcm corresponding to an equivalent doping of $7 \cdot 10^{17}\text{-}1 \cdot 10^{18}$ cm^{-3}. The Ge mobility and minority carrier lifetime were set according to the material characterization.

As the Si layer was very thin and semi-insulating while the Ge was three times more conductive, a complete depletion of Si was expected at the heterojunction. Fig. 4.2 shows the majority carrier concentration of Si at zero and 10 V reverse biases. As anticipated, the Si underlayer is completely depleted and depletion extends laterally when reverse biasing the junction; this mechanism introduces a limitation when designing the distance between the cathode contacts and the waveguide. If d is too short, the depleted region could reach the cathode contacts and cause the junction punch-through. Hence, d was limited by the maximum applied reverse bias. Fig. 4.2 shows that at 10 V reverse the space-charge region extends laterally for 5 μm, so the contact distance d was conservatively fixed to a default of 10 μm.

The electric field distributions at zero bias in the space-charge region are shown in fig. 4.3. Fig. 4.3(a) is the electric field component parallel to the junction, while fig. 4.3(b) is the orthogonal component with corresponding intensities at 100 nm from the junction (about half thickness). The orthogonal component dominates under the Ge
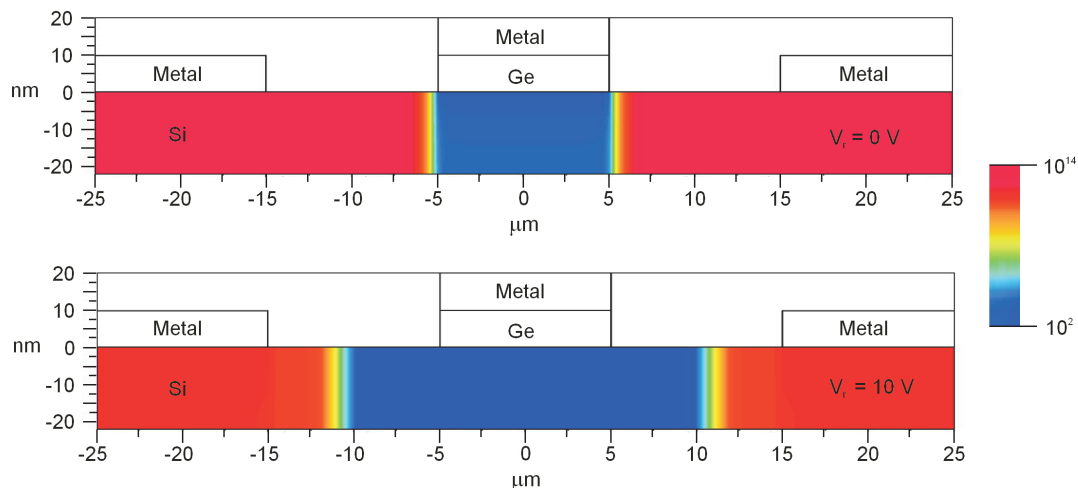
Figure 4.2: WPD space-charge region - Majority carrier concentration in Si at zero and $10V$ reverse bias

ridge, while the parallel electric field is near by zero. This field distribution implied difficulties in photocarrier collection, as photocarriers generated in the Ge film and vertically accelerated by the strong electric field in the Si underlayer will recombine in the space region if not rapidly swept away towards the Si neutral regions.

This mechanism affects the collection efficiency of the device considerably, the larger the Ge ridge (and consequently the region at zero electric field) the least the probability to efficiently collect the photocarriers generated at the waveguide center where the peak of the optical mode is located. Fig. 4.4 shows normalized collection efficiency versus waveguide width w at zero and 10 V reverse biases. The collection efficiency decreases with increasing w as expected but, unfortunately, an increase of the applied reverse bias does not significantly improve the efficiency. Therefore, the waveguide width should be minimized to improve collection. However, the available lithographic facilities did not allow to scale downwards the waveguide width below 2 μm, so we had to design WPD of 5 and 10 μm widths.

In conclusion, the simulations of the electric properties demonstrated that the geometry aspect ratio, as weel as the semi-insulating properties of Si, imposed crucial constraints on device design. The depletion region forced a minimum distance between contacts to avoid punch-through, the electric field distribution suggested to minimize the waveguide width in order to optimize the collection efficiency.
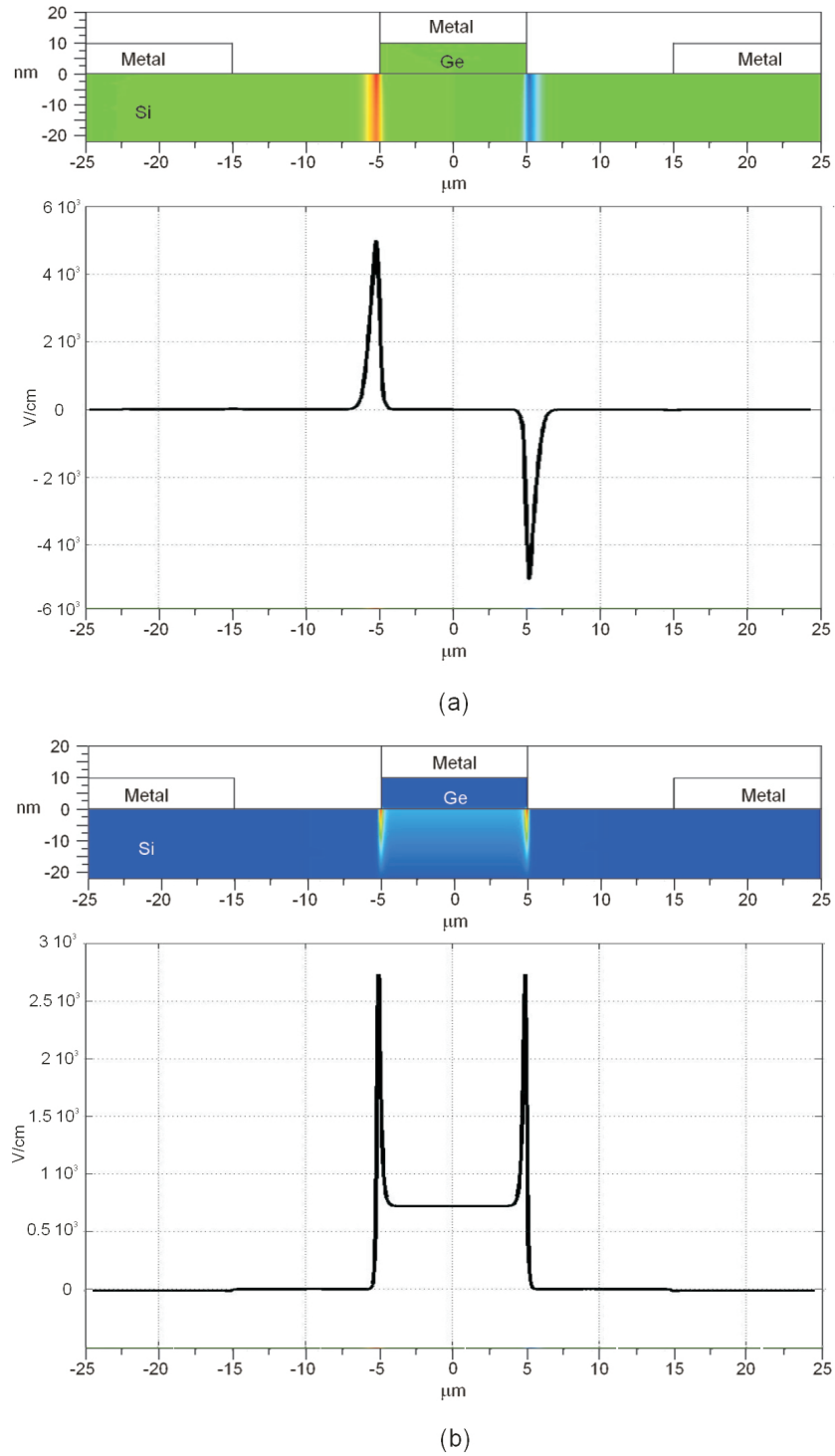
(a)

(b)

Figure 4.3: WPD electric field distribution - Electric field distribution in unbiased WPD: (a) field component in the direction parallel to the junction plane, (b) orthogonal component. Field intensity profiles are evaluated in Si at 100 nm below the junction.
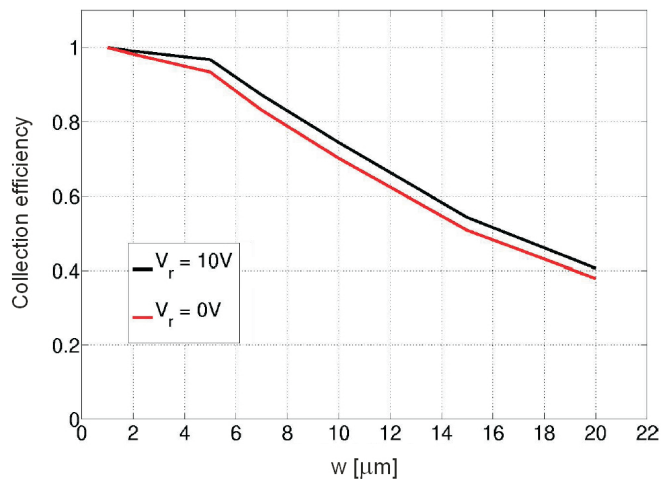
Figure 4.4: WPD collection efficiency - Normalized collection efficiency versus waveguide width at 0 and 10 V reverse bias.

4.1.2 Simulation of the Optical Properties

The waveguide optical properties were numerically studied using a vectorial eigen-mode solver for two-dimensional optical problems. We simulated two types of heterostructures as shown in fig. 4.5: (a) WPD1 the anode contact covering the Ge waveguide and ending on a pad for the external contact; (b) WPD2 similar to WPD1, but with the anode metal limited to the contact pad. The optical simulations were aimed at defining the best parameters for an optimum absorption efficiency.

The evaporated Ge exhibits high equivalent doping and a short depletion region at the junction (about 1 nm). Since Si does not absorb at wavelengths longer than 1 μm, the WPD active region coincides with the electron diffusion length in Ge (about 25 nm). The absorption efficiency is strictly related to a trade-off between absorption in the Ge active region and losses from the non-active Ge and the metal layer for the contacts. It can be expressed as:

$$\eta_{abs} = \frac{n_{Ge}k_{Ge} \int\int_{Ge_{active}} |E|^2 dxdy}{n_{Ge}k_{Ge} \int\int_{Ge_{tot}} |E|^2 dxdy + n_M k_M \int\int_{Metal} |E|^2 dxdy} \tag{4.1}$$

where n and k are the real and imaginary parts of the index of refraction, respectively, and E is the electric field distribution of the optical mode. The metal is of
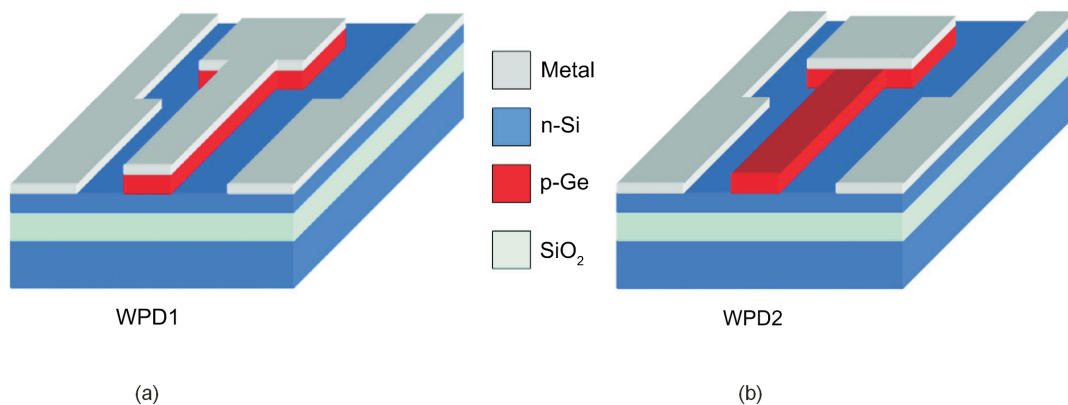
Figure 4.5: Schematics of simulated devices - Device schematic of WPD1 (a) and WPD2 (b)

big relevance in the evaluation of absorption efficiency: it is crucial to choose a low loss metal providing good contact ohmicity. Gold was identified as the best material. Fig. 4.6 shows the absorption efficiency of WPD1 and WPD2 versus the Ge thickness t_{Ge}. In WPD1 the efficiency exhibits a maximum due to the the presence of two competing mechanisms: for small Ge thicknesses the metal losses increase, limiting light absorption in the active Ge layer close to the heterojunction where the photo-carriers contribute to the current; for large Ge thicknesses the metal losses decrease, but more absorption takes place in the non-active Ge, where photo-charges rapidly recombine without contributing to the current.

In WPD2 the lack of metal contact on the waveguide improves the efficiency at smaller thicknesses and, for a Ge thickness of 100 nm, the absorption efficiency is nearly doubled; unfortunately, the absence of metal reduces the collection efficiency due to the reduced bias capability. Fig. 4.7 displays the normalized collection efficiency at 1 V reverse bias for a WPD2 versus metal film extension from the pad to the input facet: the efficiency nearly halves as the length of the metal contact tends to zero (i.e. as the device evolves from WPD1 to WPD2). Nevertheless, the responsivity of WPD2 could be increased and restored to WPD1 values by acting on the bias.

The last design parameter is the device length. It depends on absorption of the traveling optical wave along the waveguide and can be estimated from the characteristic length at $-10dB$, defined as the length at which the guided intensity reduces to 10%
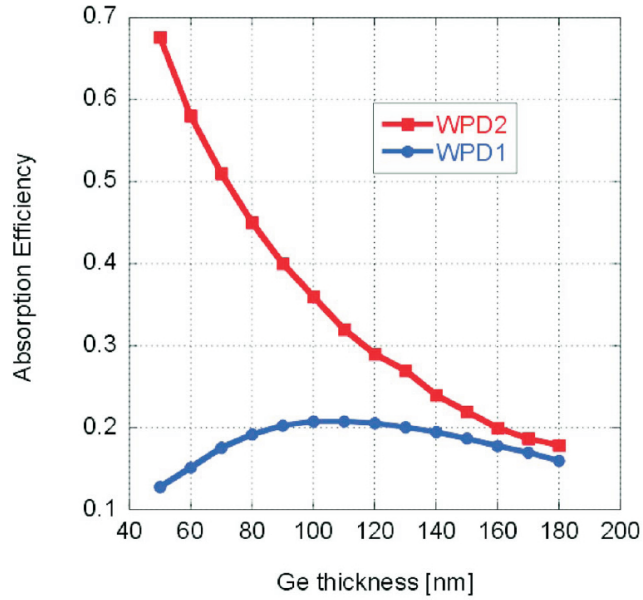
Figure 4.6: WPD absorption efficiency - Absorption efficiency versus Ge thickness of WPD1 and WPD2
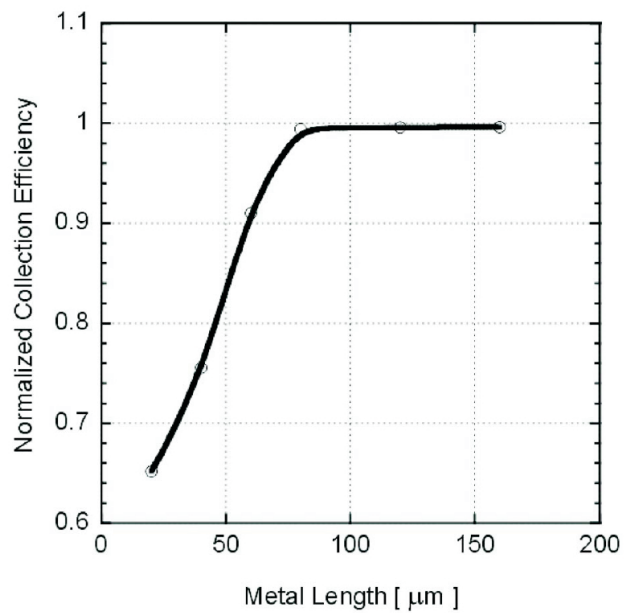

Figure 4.7: WPD2 collection efficiency - Normalized collection efficiency versus top contact length, for a 100 μm long waveguide ending in a $60 \times 60 \mu m^2$ pad and at 1 V reverse bias.

and expressed as:

$$L_{-10dB} = \frac{1}{2k_0 k} ln\,(10) \tag{4.2}$$

where $k_0 = \frac{2\pi}{\lambda}$ and k is the imaginary part of the modal effective index. The -10 dB length depends on t_{Ge}, the thicker is the Ge the shorter is the $-10dB$ length both for WPD1 and WPD2 because of the increasing absorption. Maximum -10 dB length of about 60 μm was estimated by simulations and the device length was conservatively set to 100 μm in order to achieve nearly complete light absorption.

In conclusion, the optical simulations allowed to define the proper design for absorption in the guiding structure. The evaluation of optical losses was fundamental in setting the optimum Ge thickness and the waveguide length.

4.2 Germanium Near Infrared Detectors on Silicon-on-Insulator

Tab.4.1 summarizes the design parameters derived from device simulations. With these parameters we defined a single photomask for WPD1, allowing self-alignment of the Ge waveguide and the anode electrodes after the etching of metal and Ge. WPD2 were fabricated by a standard two-step lithographic process with different mesa, and metal photo masks.

Parameter	symbol	value
Waveguide length	L	100, 200 μm
Waveguide width	W	5, 10 μm
Contacts distance	d	10 μm
Ge thickness	t_{Ge}	110 nm (WPD1)
		80 nm (WPD2)
Metal	-	Au
Si thickness	t_{Si}	220 nm
Si resistivity	ρ_{Si}	10-30 Ωcm
Oxide thickness	t_{ox}	3 μm
Anode contact pad	A_{pad}	60x60 μm^2
Device area	A	WL+$(L_{pad})^2$

Table 4.1: Design parameters - WPD1 and WPD2 design parameters, WPD2 differs for absence of metal upon the Ge waveguide

The fabrication began with the evaporation of Ge on SOI properly cleaned and passivated as described in the previous chapter. The evaporations were always performed at a substrate temperature of 300°C and growth rate of 2 $\mathring{A}/s$ in a constant vacuum of 10^{-7} $Torr$. The as-deposited Ge on SOI were immediately placed in the second vacuum chamber for metalization, evaporating gold to a final thickness of 100 nm. As the waveguide input facets were at the edge of the samples to allow end-fire light coupling, the samples were cleaved after Ge and metal deposition, in order to reduce the occurrence of Ge or metal residuals at the input facets. Ge mesas and metal contacts were defined by standard optical lithography and selective wet etching of metal and

Ge. All the samples, both WPD1 and WPD2, provided cathode contacts with Ge between Si and metal. This did not represent a drawback: in fact, when a WPD operates in reverse bias the metal/semiconductor junctions at the cathodes are forward biased, resulting in injecting contacts with reduced resistance with respect to the gold directly deposited on the low conductivity silicon. Fig. 4.8 shows some fabricated devices.
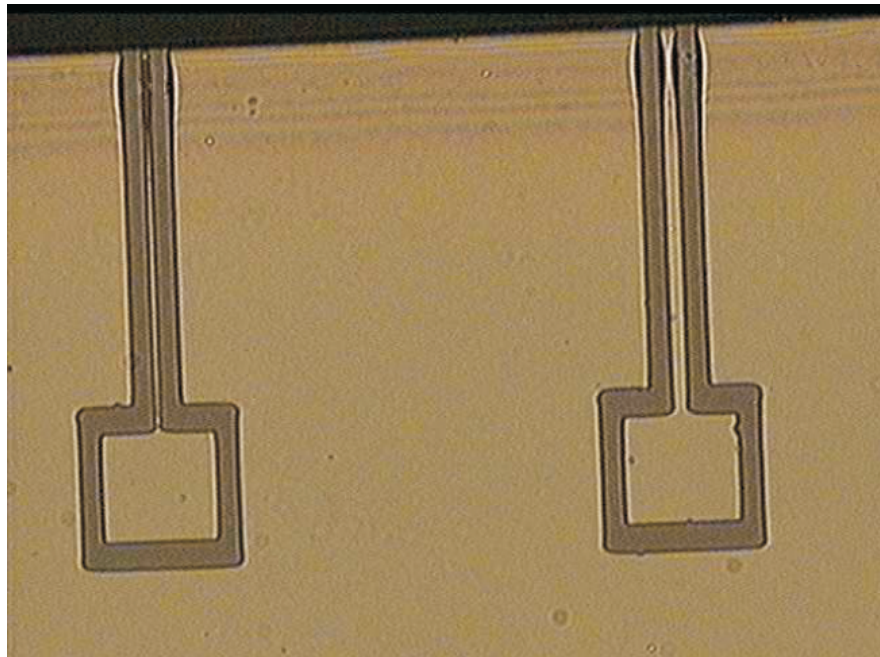

Figure 4.8: WPD1 fabricated devices - Optical microscope photograph of WPD1

The devices were characterized in terms of responsivity at a wavelength of 1.55 μm, dark current density at low bias and small-signal parameters. The current responsivity was measured by a lock-in amplifier using a cw semiconductor laser source butt-coupled to the input waveguide facet by tapered optical fibers or microscope objectives. The coupling introduced considerable losses arising from reflection at the air/device interface and modal mismatch between the input beam and the guided mode. The effective power traveling in the waveguide was estimated by measuring the optical power launched in air by the tapered fiber (or by the microscope objective) corrected by Fresnel losses and radiation-to-guided modal mismatch. The Fresnel reflection coefficient was estimated under normal incidence with the waveguide effective index of refraction evaluated by simulations: under these conditions about 70 % of the launched power was transmitted.

The overlap between the launched and the guided mode was numerically calculated by a convolution of the intensity profiles. The tapered fibers launched an input beam with overlap coefficient of 0.147, while for microscope objectives the overlap reduces to 0.116. In both cases the losses exceeded 90 % of the power. The best coupling was obtained using nanometric translation stages controlled with piezolectric controllers.

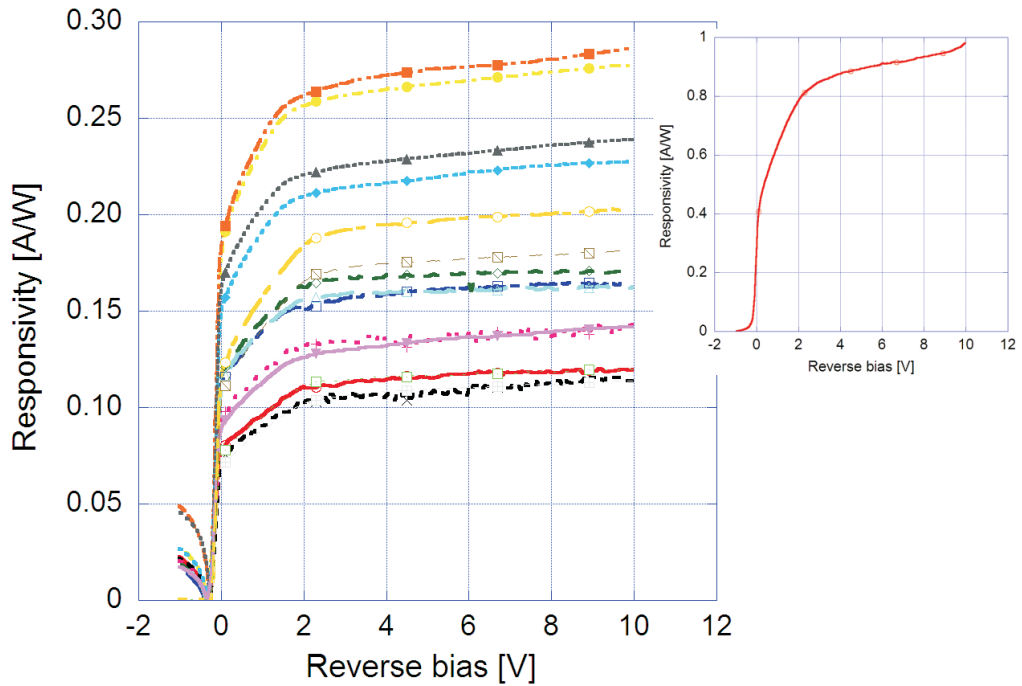Fig. 4.9 shows the typical responsivities of WPD1 versus reverse bias.

Figure 4.9: WPD1 responsivity - Typical responsivities versus reverse bias of WPD1 at 1.55 μm

The typical values were between 0.1 and 0.3 A/W at 1.55 μm. The highest measured value (inset) matched the largest reported value obtained from a butt-coupled photodiode with single-crystal Ge on Si (65). Unfortunately, we did not succeed in reproducing this result, that was probably associated to unintentional avalanche multiplication of photocurrent with increasing bias. This hypothesis was supported by the constant increase of photocurrent, while at zero bias the responsivity ($\approx$ 0.2 A/W) compared well with typical values. Despite the aforementioned collection problem arising from the thin high-resistivity Si layer, the responsivity was close to its maximum

at low bias and remained above 60 % in the photovoltaic mode, i.e., for $V_r = 0\ V$. The dispersion of the characteristics, visible in the figure, was attributed to the poor quality and repeatability of the cleaved (but unpolished) input facets.

The dark current versus reverse bias is displayed in fig. 4.10. WPD1 exhibited dark currents at a reverse bias of 1 V ranging between 40 and 500 nA, with moderate increases with voltage till 0.2 and 2 μA at $V_r = 10\ V$. The minimum dark current density at $V_r = 1\ V$ was 0.8 mA/cm^2. The dispersion in dark current was attributed to under-etching during the Ge mesa formation, as the presence of metal on Ge causes a little built-in potential at the interface, catalyzing the chemical etching. Under these conditions the Ge was etched faster near the metal interface, causing a strong Ge under-etching; hence, the devices exhibited mesa with random small geometrical differences responsible of data dispersion.
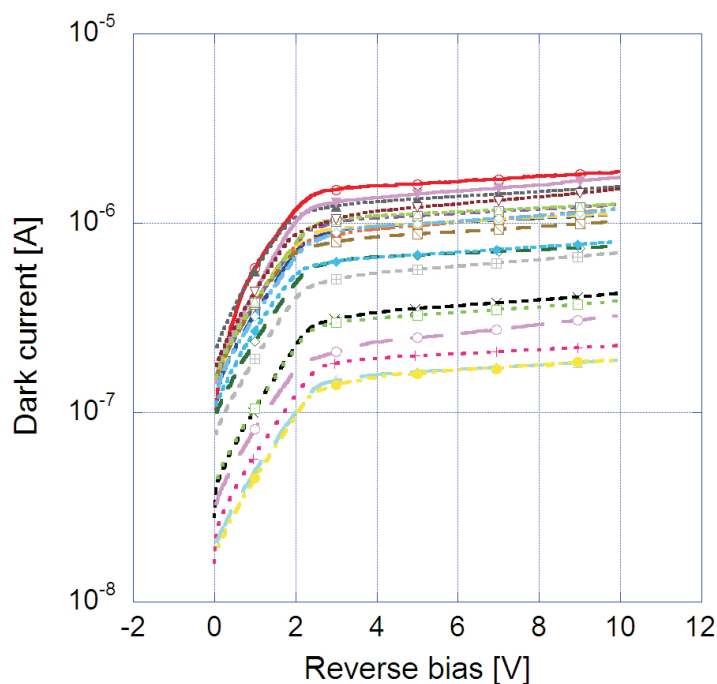

Figure 4.10: WPD1 dark current - Typical dark current versus reverse bias in WPD1

Since the prototypes were designed for channel monitor operations in optical chips, it is essential to characterize the SNR for this application. The optical channels can be monitored by a low frequency test signal derived from the optical bus and coupled

to the photodetector. The specifications for this require a test signal at 100 kHz and modulated at 1 % with a bandwidth of 1 kHz to allow coherent detection by a band-pass filter with sharp bandwidth to minimize the noise contribution. As discussed in a previous section, the main source of noise in NIR photodetctors is the shot-noise, ascribed to random fluctuations of the electric current in a junction. The shot-noise current is statistically described by its standard deviation:

$$\langle i_s \rangle = \sqrt{2q\Delta\nu I} \qquad (4.3)$$

where q is the electron charge, $\Delta\nu$ the bandwidth and I the current flow in the device. In our case, where the signal was detected by a selective band-pass transimpedance amplifier with 1 kHz bandwidth, the SNR can be expressed by:

$$SNR = 20log\frac{I_{ph}}{i_s} = 20log\frac{0.01P_{in}R}{\sqrt{2}}\frac{1}{\sqrt{2q\Delta\nu\left(I_d + I_{ph}\right)}} \qquad (4.4)$$

where P_{in} is the input optical power, R the responsivity, I_d the dark current and I_{ph} the photocurrent. Fig. 4.11 shows the calculated SNR (for WPD1) versus reverse bias for 0.1 μW input power. The results emphasized the optimal operations at low reverse bias with SNR ranging from 19 to 28 dB at $V_r = 0.1$ V. The best devices exhibited SNR above 20 dB in the full range of biases.

The characterization was completed by the evaluation of the small-signal equivalent-circuit parameters. Fig. 4.12 shows the measured junction capacitances C_j versus reverse bias. C_j is below 5 pF, decreasing down to 0.15 pF for $V_r > 6$ V. The series and shunt resistance were extracted from the I-V curves by derivation of forward and reverse characteristics. The series resistance was rather large, with typical values in the $k\Omega$ range (5 $k\Omega$); this was associated to carrier transport in the thin and lightly doped n-type neutral region. The shunt resistance was greater than 2 $M\Omega$ for any reverse bias and > 10 $M\Omega$ for $V_r > 2.5$ V, more than satisfactory for detector applications. Even if the low junction capacitance suggested possible multi-Gbit/s operation of these detectors, the semi-insulating Si layer restricted the device bandwidth to a few hundred megahertz, limiting the device to low frequency operation. Possible improvements would require a selective local doping of the Silicon to enhance its conduction properties
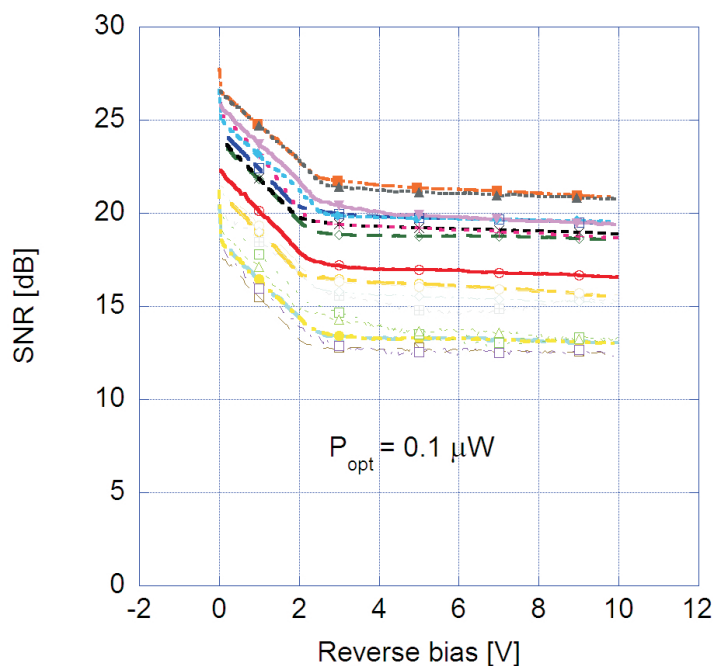
and, consequently, the bandwidth of the device.

Figure 4.11: WPD1 signal-to-noise ratio - Typical SNR versus reverse bias of WPD1 devices, calculated according to eq. 4.4

Finally, WPD2 characterization is discussed. The devices were fabricated with a Ge thickness of 80 nm to take advantage from the improved absorption efficiency displayed in fig. 4.6. Fig. 4.13 shows the typical measured dark currents versus reverse bias, and fig. 4.14 the observed responsivities. Unfortunately the WPD2 performance did not exhibit the expected improvements.

The typical responsivities were in the same range of WPD1, with best result of 0.4 A/W at 10 V reverse, but the expected worsening of the collection efficiency caused the drastic decrease of responsivity at low reverse bias. This aspect was crucial in the SNR calculations as the high dark currents, together with the low responsivities at low bias, affect the performance dramatically, with maximum SNR often below 10 dB, as visible in fig. 4.15. The mismatch between expected and observed performance was associated to technological problems. In the WPD2 process flow the metal was previ-
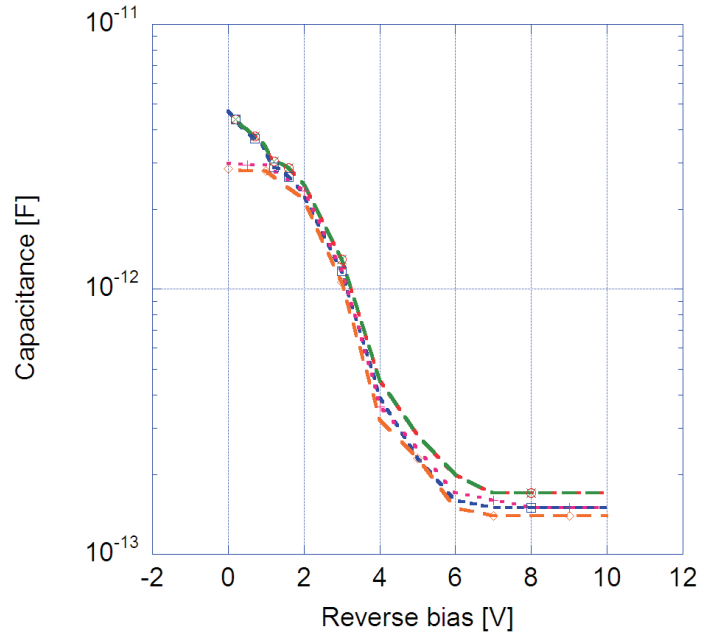
Figure 4.12: WPD1 capacitance versus reverse bias - Typical capacitance of WPD1 devices versus reverse bias
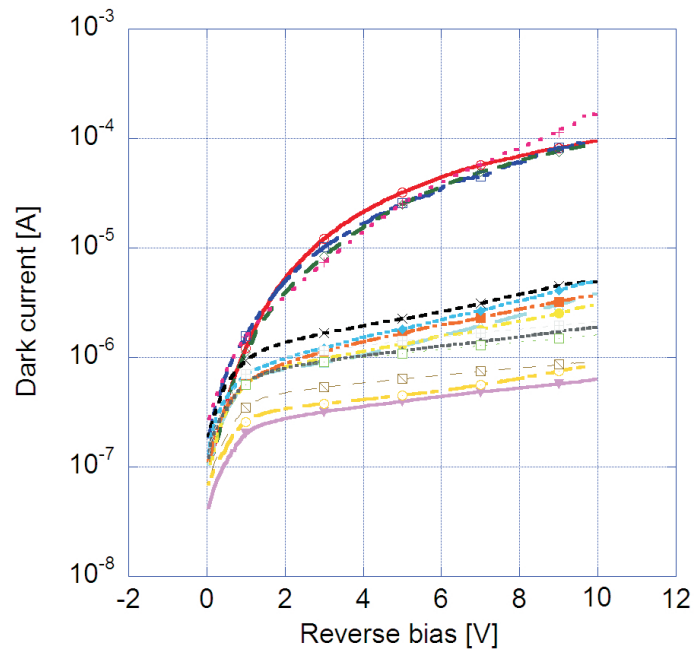

Figure 4.13: WPD2 dark current versus reverse bias - Typical WPD2 dark current versus reverse bias

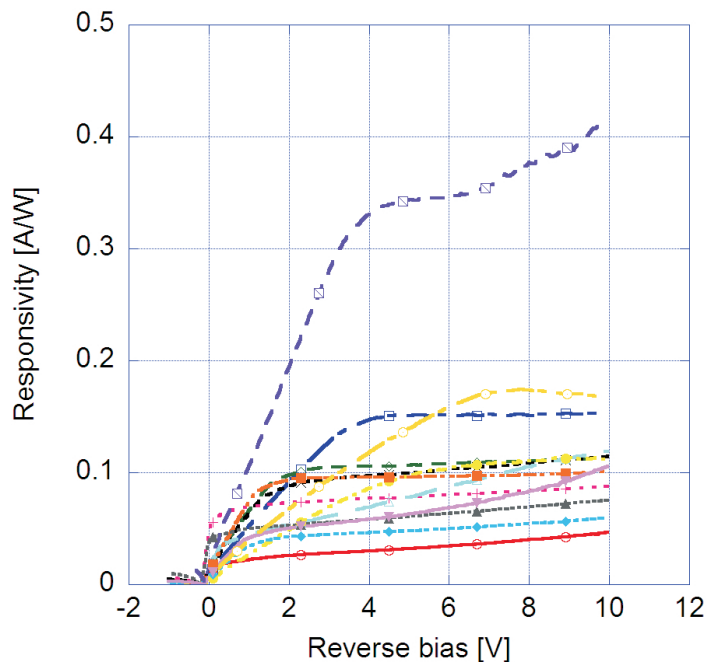ously deposited on the Ge waveguide and then removed by a chemical wet etch.

Figure 4.14: WPD2 responsivity versus reverse bias - Typical responsivity versus reverse bias at 1.55 μm

This process was probably responsible for a deterioration of the Ge surface, yielding a decreased responsivity due to increased optical losses (scattering), and for high surface recombination producing large surface leakage currents. Remarkable improvements are expected by the adoption of a lift-off process for contact definition, as employed in the subsequent integration stage (see next section).

In conclusion, we demonstrated that by adopting distributed absorption in waveguide structures it was possible to obtain high responsivity NIR photodetectors by thermal evaporation. WPD1 devices exhibited very promising responsivities with typical value of 0.2 A/W at 1.55 μm. The SNR performance suggested the capability of WPD1 devices to work as power monitors in optical channels. Unfortunately the employed semi-insulating substrate causes strong limitations to the device speed. These constraints could be overcome by local doping the Si regions involved in the transport mechanisms and pursuing increased bandwidths towards multi Gbit/s operation. Both photocurrent and dark current performance encouraged further developments and use
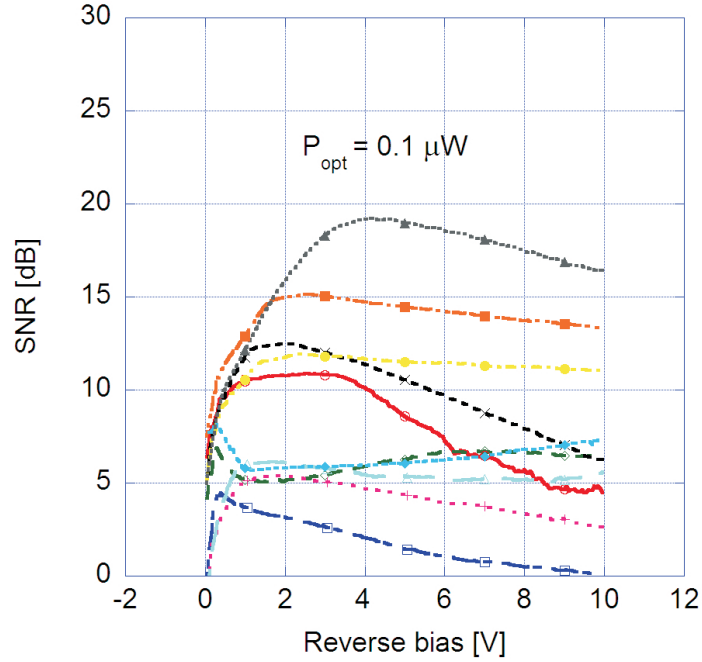
Figure 4.15: WPD2 signal-to-noise ratio - Typical SNR versus reverse bias of fabricated WPD1 devices calculated according to eq. 4.4

of this deposition technique towards monolithic integration on Si-based optical chips. The next section is dedicated to the integration of WPD1 and WPD2 on SOI optical chips for power monitor applications.

4.3 Guided-wave Photodetectors in Ge on SOI Optical Chips

In this section I present the integration of evaporated Germanium WPD on Silicon-on-Insulator optical chips to realize circuits with embedded signal power-monitors. The optical chip was a testbed for WPD detectors integrated on a SOI platform, it was designed in collaboration with Pirelli Labs and fabricated by Pirelli Labs. The SOI chip consisted of a set of monomode ridge waveguides of size $480 \times 220 \ nm^2$ with tapered endings (for modal matching with 5 and 10 μm WPD) towards Si sites where we could fabricate the photodetectors. The waveguides were about 5 mm long, while the tapers extended with linear or exponential profiles for 0.5, 1 and 1.5 mm. The chip contained a few through-waveguides provided with bends of different lengths to help estimating the coupling as well as the propagation losses. All the optical elements (waveguides, bends, tapers and silicon sites) were defined by e-beam lithography and the whole chip was covered by a TEOS cladding with vias on the silicon sites. Fig. 4.16 shows some details of the chips.
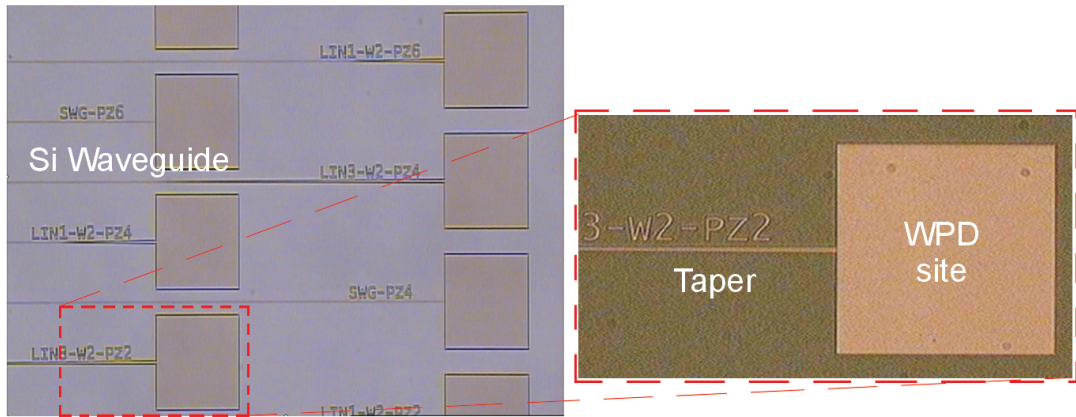
Figure 4.16: Optical chip - Details of the SOI optical chip. Si waveguides, tapers and detector sites are visible

We characterized the Si waveguides in terms of optical propagation and coupling losses to estimate the effective power at the input of the detectors. A cw semiconductor laser was butt-coupled to the waveguide by a tapered fiber, then the guided light was collected at the output facet by a microscope objective and measured with a lock-in

amplifier. The losses were evaluated from the input/output ratio and plotted versus waveguide length. Fig. 4.17 shows the typical results: the linear fit the of experimental data yielded the coupling (intercept) and the propagation losses of waveguides (slope), with typical values of 10 dB and 3 dB/cm, respectively.
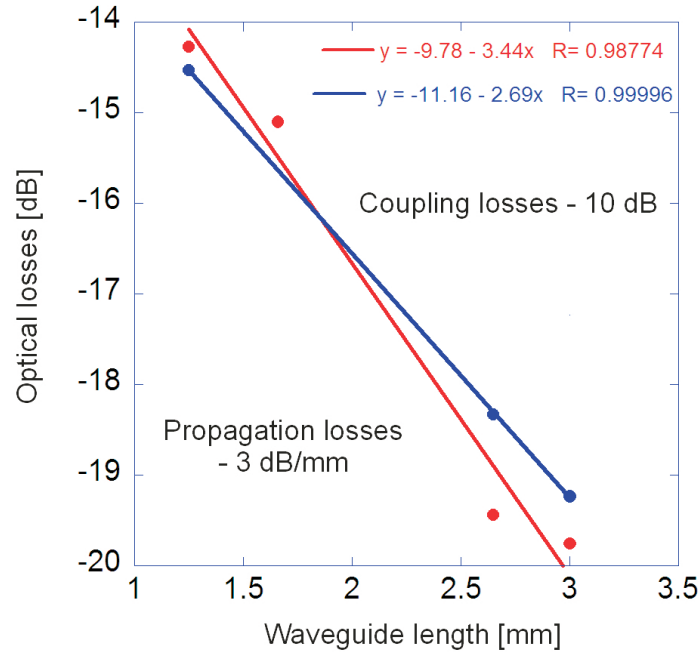

Figure 4.17: Waveguide losses - Evaluation of coupling and propagation losses of Si waveguides by linear fitting the optical attenuation versus waveguide length. The intercept corresponds to the coupling losses, while the slope gives the propagation losses.

We focused our attention on WPD1 because of a higher reliability and a simpler technological process (single self-aligned step). Unfortunately, the first results did not match the expectations. Fig. 4.18 shows the responsivities at 1.55 μm versus applied bias, obtained from the first generation of integrated devices. We observed zero short-circuit photocurrent with symmetric non-monotononic profile versus bias. These anomalous operation was explained by high losses at the taper/WPD interface.

After several SEM analyses we concluded that the strong under-etching already observed in the prototypes caused high mismatch between waveguides and tapers. Fig. 4.19 is a SEM picture of WPD1 5 and 10 μm waveguide details, clearly showing under-etching with an effective Ge width of about 1 and 6 μm, respectively.
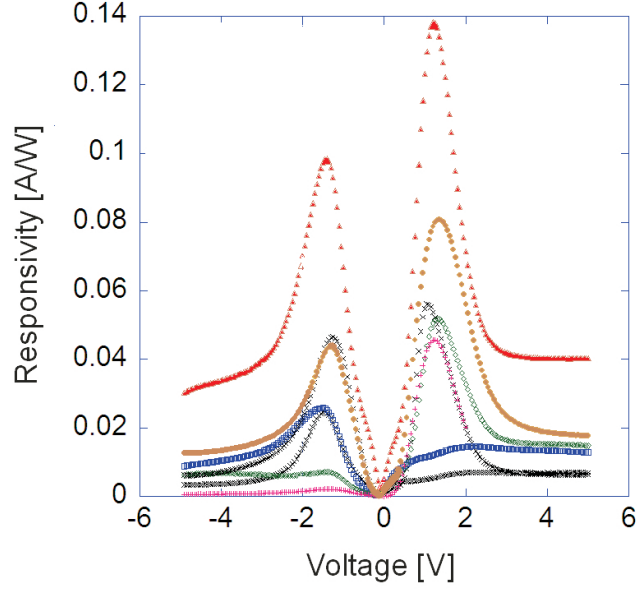
Figure 4.18: WPD1 on chip, preliminary results - Responsivity versus bias at 1.55 μm. The responsivity is higher in forward bias, demonstrating detection by the cathode Ge/Si junction.

The 4 μm mismatch between the taper and the Ge waveguide was responsible of light escaping the Si waveguide and diffracting in the Si site where was collected by the Ge waveguide and the Ge under-cathode contacts. This was responsible of the symmetric responsivity; in fact, when the Ge waveguide was forward biased, the junctions at the cathodes were reverse biased and collected the diffracted light. At zero bias the two photocurrents cancel out resulting in nearly zero responsivity. This problem could be solved by selective (anisotropic) plasma etching of Ge to ensure proper matching between tapers and waveguides. Since we could not employ this technique, the problem was bypassed by adapting the 5 μm tapers onto the 10 μm devices.

Fig. 4.20 shows the performance of WPD1 fabricated with the proposed approach. The characteristics exhibited the same profiles of the prototypes. The integrated WPD1 exhibited typical dark currents in the range 0.2-2 μA at 1 V reverse bias (fig. 4.20(a)), with corresponding densities of 440 mA/cm^2, about ten times larger than in stand-alone devices. This was attributed to both under-etching and poor quality of the passivated

silicon surface accessed through the via in the TEOS cladding. The last hypothesis also explained the responsivity profiles with the expected shape but lower values.
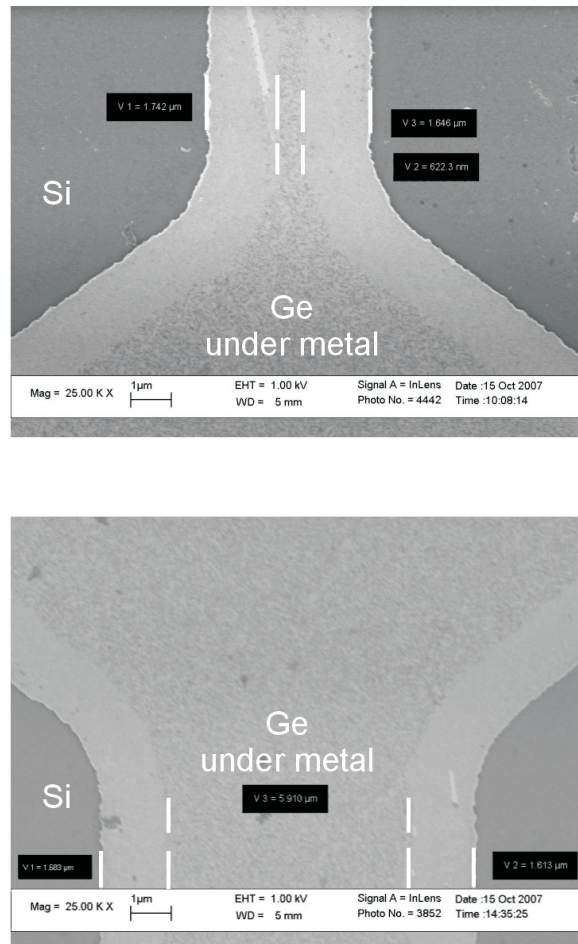
Figure 4.19: SEM acquisition on WPD1 samples - SEM acquisition on WPD1 devices with 5 and 10 μm waveguides. In both cases it is observed 4 μm under-etching.

Fig. 4.20(b) shows the maximum responsivity of 40 mA/W at 1.55 μm lower than the predicted best performance of about 280 mA/W. This discrepancy was attributed in part to the extra losses of about 3 dB due to mode mismatch between the Si taper and the multilayer metal-Ge-Si-insulator waveguide, as visible with the aid of a NIR camera. However, even accounting for these extra losses, the responsivity was lower than expected, possibly because of an insufficient passivation of the Si surface with the consequent creation of recombination centers in the heterojunction. To validate this

Figure 4.20: WPD1 on chip - Typical WPD1 on chip performance: (a) dark currents versus reverse bias, (b) responsivity versus reverse bias at 1.55 μm

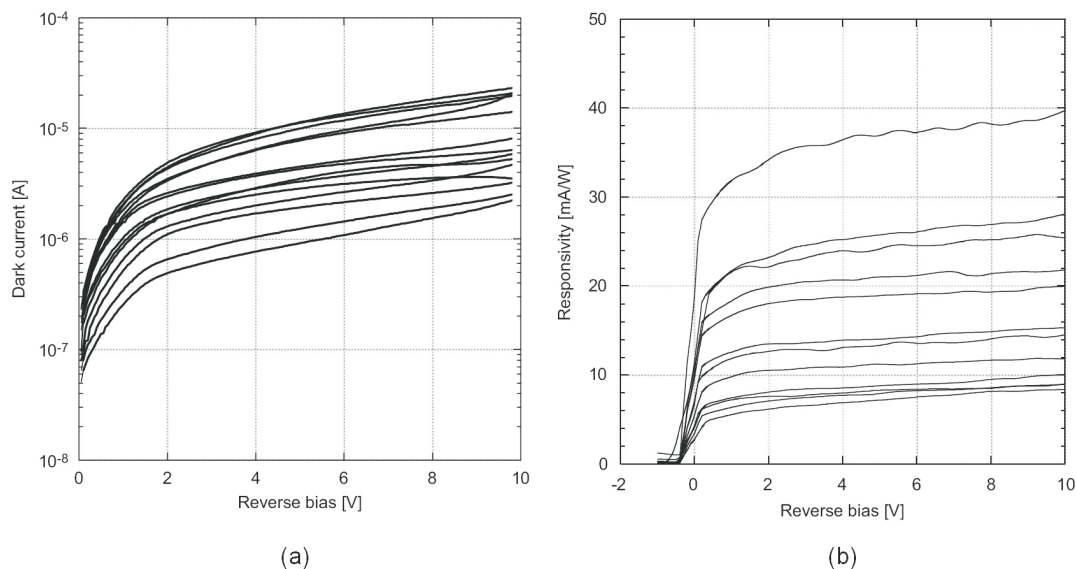hypothesis we performed an extensive characterization of Ge evaporated on chip. Fig. 4.21 shows an Atomic Force Microscopy (AFM) analysis of Ge grown on TEOS, Ge on Si sites and Ge on a bulk Si wafer. The figure shows similarities between Ge morphology on TEOS and on Si sites. In both the Ge exhibited a larger roughness with respect to Ge on bulk Si. The average dimension of the Ge crystallites on the Si sites was estimated in 50 nm, while the mosaicity of Ge on bulk Si (caused by threading dislocations) exceeds 100 nm. The average Ge roughness on bulk Si was about 0.8 nm, but increased towards 2.2 nm for Ge on TEOS and on Si sites. These results demonstrated that Ge on Si sites exhibited characteristics approaching the polycrystalline structure of Ge on insulator rather than the observed monocrystalline structure of Ge on Si.

This granular structure was ascribed to the passivation process, as a good passivation of the Si sites is crucial in determining the structural properties of Ge. While in bulk substrate it did not represent technological problem, the passivation of small Si sites in the presence of extended oxide introduces complications. In fact the employed BOE solution was extremely aggressive towards the cladding, as apparent in fig. 4.22 showing pre- ad post-fabrication SEM images of the edge of the TEOS via. TEOS etching was thought to product contaminants which hindered Si passivation and dete-

Ge on Si site

Ge on Si wafer
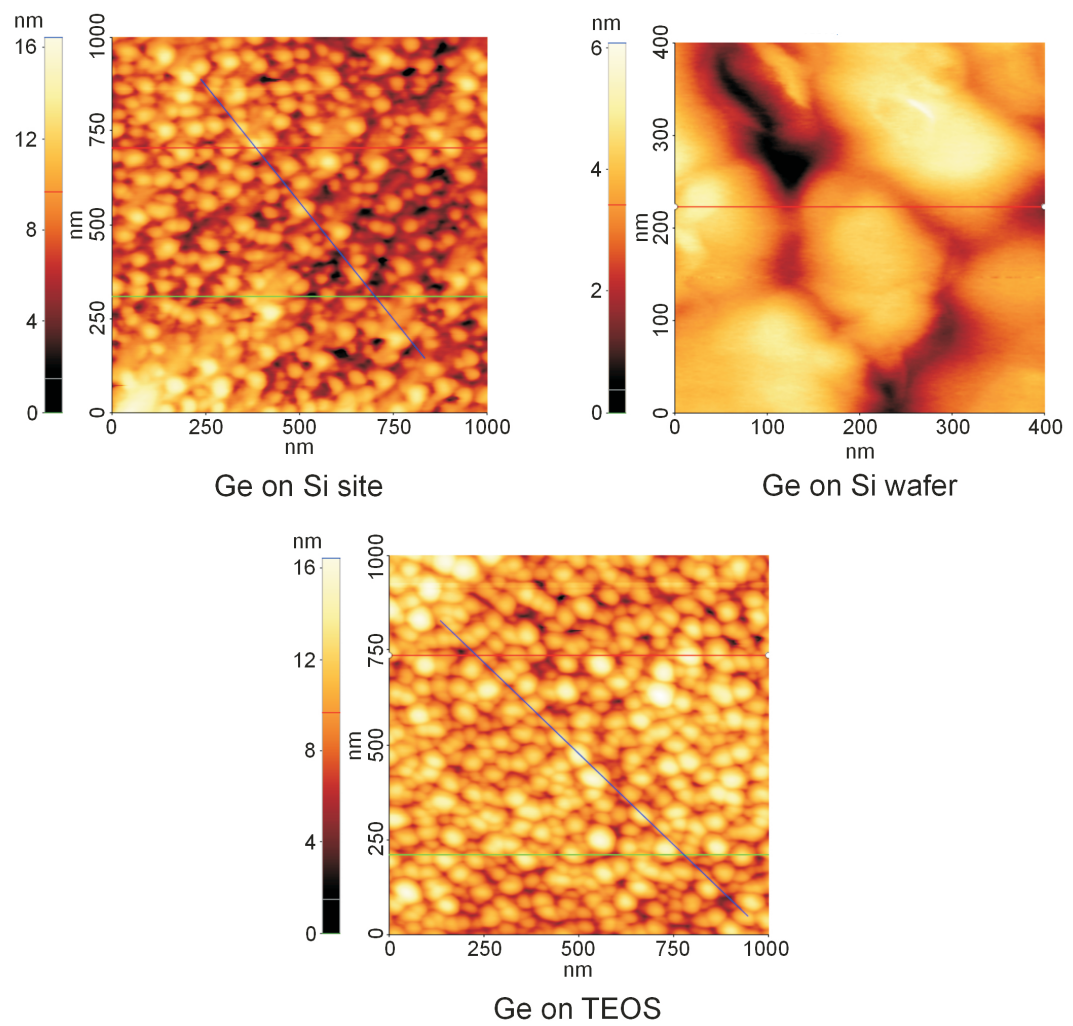
Ge on TEOS

Figure 4.21: AFM analysis of Ge surface - AFM analysis of Ge grown on Si sites, on bulk Si and on TEOS

riorated the properties of Ge. Possible improvements involve H-plasma passivation of Si to prevent the contamination of its surface.

<div align="center">Pre-process   Post-process</div>
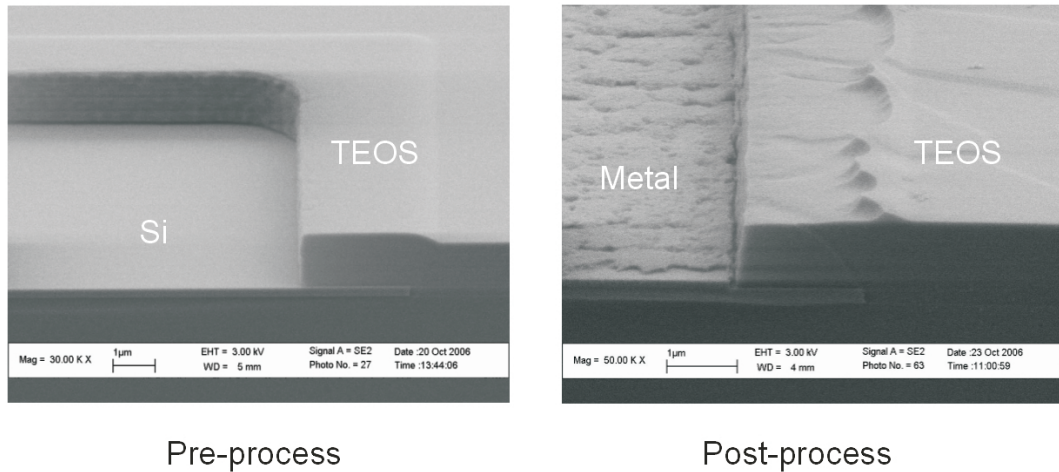
Figure 4.22: SEM images of TEOS cladding - SEM images of TEOS pre- and post-fabrication process.

We also fabricated and characterized WPD2 devices adopting the lift-off technique for contact definition. Fig. 4.23 shows the typical results for dark current (a) and responsivity (b) versus reverse bias. WPD2 exhibited typical dark currents in the same range of WPD1, the responsivity was definitely improved with a maximum responsivity of 0.11 A/W at 1.55 μm and 3 V reverse bias and a strong dependence on reverse bias owing to the limited collection of photocharges at lower voltages. This result agreed with the calculated improvements of the optical absorption, confirming that the performance of stand-alone WPD2 were affected, as anticipated, by the worse guiding properties of Ge waveguides due to the metal etch. WPD2 exhibited non-monotonic responsivities caused by the distribution of the electric potential along the waveguide. The waveguide had a distributed potential drop from the anode towards the input facet, due to Ge and Si resistivities. As most of the absorption took place near the input facet (where the electric field is minimum), the responsivity was more sensitive to the reverse bias with respect to WPD1. WPD2 worsen at increasing bias because of punch-trough at the cathode contact.
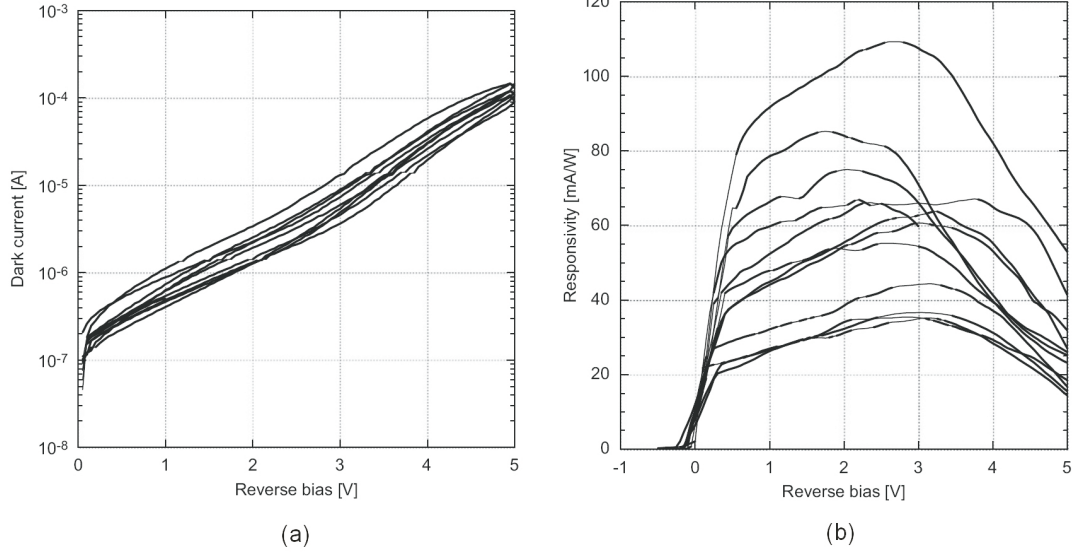
Figure 4.23: WPD2 on chip - Typical WPD2 on chip performance: (a) dark current versus reverse bias, (b) responsivity versus reverse bias at 1.55 μm

In fact, WPD2 were fabricated with a distance of about 5 μm between the contact and the Ge waveguide, i.e. short with respect to the extension of the depletion region in Si. Fig. 4.24 shows the calculated plot of the depletion region in Si versus reverse bias. When the reverse bias is about 3 V the calculated depletion region exceeds the 5 μm of the contact distance, compromising the correct operation of the photodetectors. This problem could be easily solved by re-designing a properly dimensioned photo-mask.

Beyond the problems discussed above, both WPD1 and WPD2 exhibited promising performance for power monitor operation. To complete the analysis, the signal-to-noise ratio was calculated. Because of the low responsivity, we decided to employ the devices as cw-power monitors; the SNR was calculated according to:

$$SNR = 20log\frac{I_{ph}}{i_s} = 20log\frac{P_{in}R}{\sqrt{2q\Delta\nu\left(I_d + I_{ph}\right)}} \tag{4.5}$$

Fig. 4.25 graphs the evaluated signal-to-noise ratio (SNR) for the best WPD1 and WPD2, a 1 μW optical signal and bandwidth 1 kHz. WPD2 had a larger SNR than WPD1, although the latter can operate with good SNR even in the photovoltaic mode (zero bias). The obtained SNR were more than appropriate the use of these photodetectors as power monitors in fully integrated optoelectronic chips.
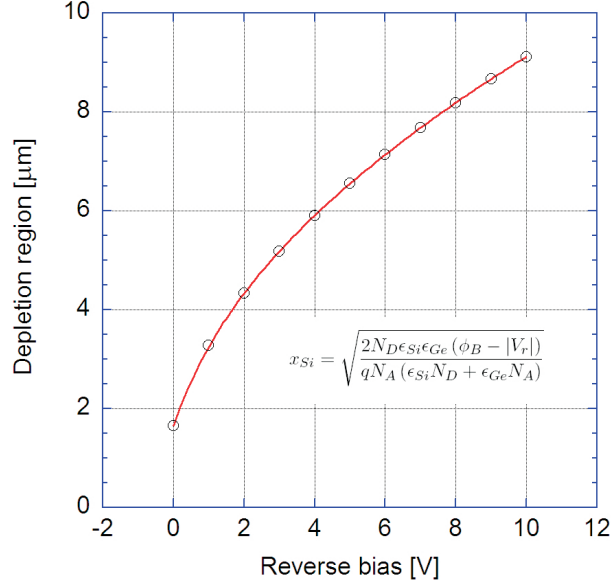
Figure 4.24: Depletion region of Si in WPD devices - Calculated extension of the depletion region in Si of WPD devices

In conclusion, the integration of Ge WPD on SOI optical chips incurred in a few technological difficulties. Nevertheless, by adopting some expedients it was possible to overcome most of them and reproduce the results obtained from the prototypes. WPD1 as well as WPD2 met the specifications for cw power monitor, as discussed in the next section. Better results are expected after optimizing the fabrication through the use of dry etch techniques for both Si passivation and waveguide definition.
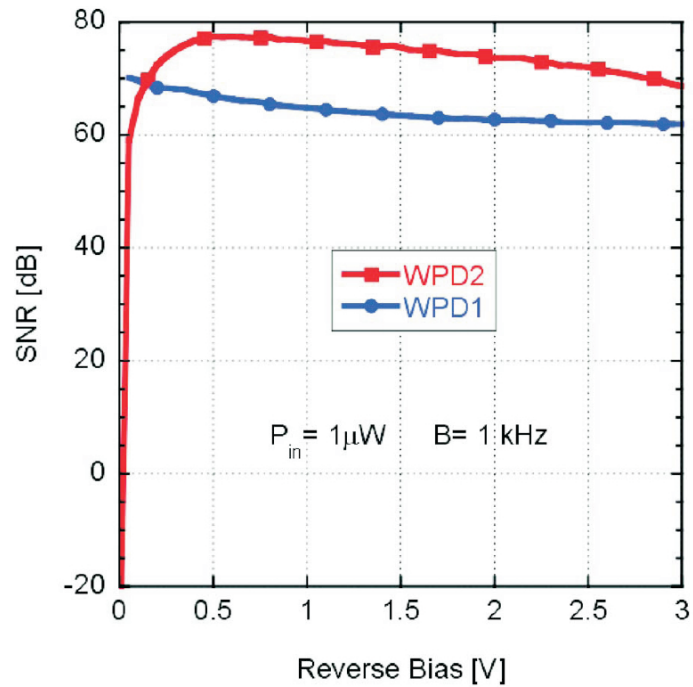
Figure 4.25: WPD1 and WPD2 on chip signal-to-noise ratio - Best SNR versus reverse bias of WPD1 and WPD2 calculated according to eq. 4.5

4.4   Near-Infrared Ge-on-Si Power Monitors Monolithically Integrated on SOI Chips

Monolithically integrated power monitors were fabricated based on WPD1 photodetectors integrated on SOI chips. To investigate the power monitor performance we designed a transimpedance amplifier (TIA) based on a commercially available operational amplifier. We adopted the OPA380, ideally suited for photodiode applications and with excellent long term stability, low offset voltage and drift and good noise characteristics. Fig. 4.26 shows the TIA configuration. Its design consisted in assigning proper values to the feedback impedance $R_F//C_F$. R_F affected the gain, and is defined by WPD1 responsivity and the maximum available output voltage.
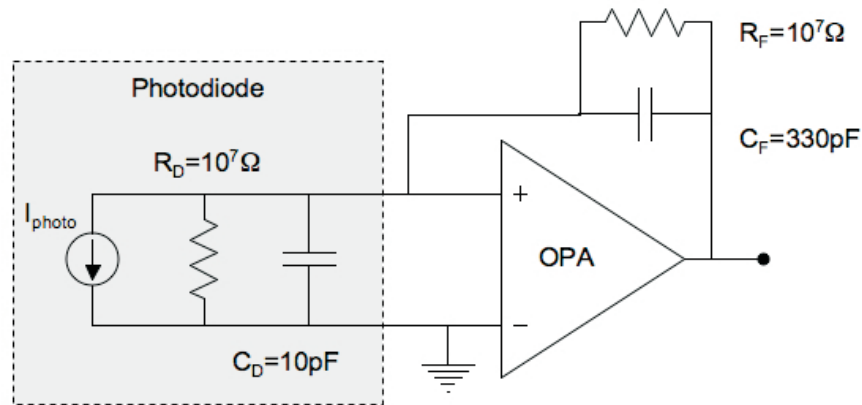
Figure 4.26: Transimpedance amplifier - TIA circuit: low-frequency Ge-on-Si photodetector (shaded area) and TIA based on OPA380

We considered a typical responsivity of 10 mA/W at zero reverse bias, while the maximum available output voltage was limited by the 5 V power supply of the OPA380. The value of R_F resulted from a trade off between signal-to-noise ratio (the signal is proportional to R_F, while the Johnson noise scales with R_F^2) and the dynamic range (we aimed at the range 10 nW-10 μW). To provide an output voltage of 1 V for a 10 μW optical input power, we needed $R_F = 10M\Omega$. C_F was set to 330 pf in order to minimize the noise with a 48 Hz cutoff frequency, while allowing several measurements per second.

The equivalent circuit in fig. 4.26 also shows the photodiode equivalent circuit, as the output noise includes the shot-noise from the photodiode. When the photodiodes operate at zero bias, the photocurrent shot-noise is negligible because of the zero contribution of dark current and low photocurrents, at least up to 100 μW (above the range of interest). Under these conditions the voltage noise at the output is dominated by the OPA380 (voltage noise about 80 V rms). At reverse bias, the dark current increases and the shot-noise is no longer negligible. Such noise, even if spectrally reduced by C_F, is amplified ten million times and strongly increases the output noise. Therefore, short-circuit operation was expected to provide the best sensitivity.

The power monitors characteristics were acquired in terms of output voltage versus input optical power, both in short-circuit and with small biases. Fig. 4.27 shows the typical characteristic of WPD1 power monitors in short-circuit. The photodiodes exhibited good linearity up to 5 V, i.e. the voltage of the OPA power supply. The rms voltage noise was about 200 μV and constant in the whole measured range. This higher than expected value was probably associated to external noise pick-up at the electric connection between the photodiode and the TIA.
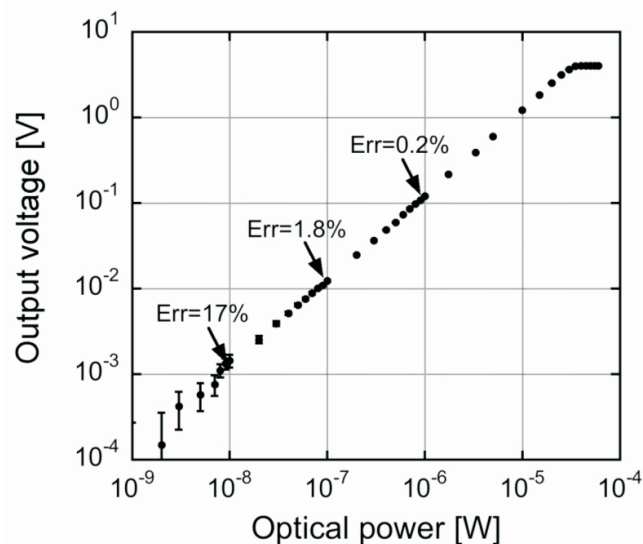

Figure 4.27: Short circuit power monitor performance - Typical characteristic of the power monitor at 1.55 μm in the absence of bias

Nevertheless, this noise did not affect the power measurements significantly, causing errors (standard deviations) of 0.2 %, 1.7% and 17% for signals of 1 μW, 0.1 μW and

10 nW, respectively. Hence, the system maintains good sensitivity in most practical situations.

Fig. 4.28 plots the typical characteristics measured at 0.1 V reverse with and without dark current cancellation. The dark current strongly affected the sensitivity of the device because of the high amplification; in fact, the 0.1 μA dark current exhibited by WPD1 resulted in a 1 V output offset not allowing an effective operation under 10 μW. In such cases it is necessary to implement a dark current cancellation circuit to restore the optimal operation as demonstrated.
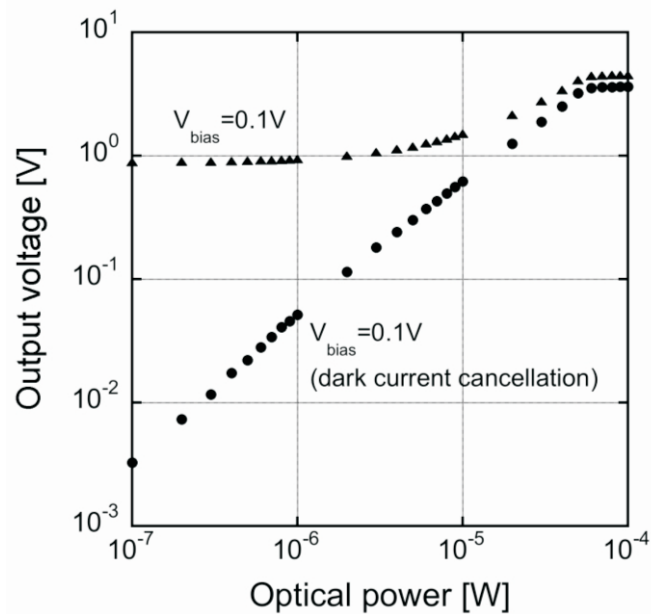
Figure 4.28: Biased power monitor performance - Characteristic of the power monitor at 0.1 V reverse bias with (circles) and without (triangles) cancellation of the dark current

This is commonly obtained by fabricating a twin blind photodiode with the same dark current characteristics. We simulated such operation by trimming a current source rather than employing the blind photodiode. Unfortunately, the extra circuitry increased the noise level, causing poor performance compared to the case of an unbiased detector.

The power monitors were also characterized versus temperature in the range 20-70°C. Fig. 4.29 shows the data for an input power of 0.1 μW. The output voltage

increased with temperature because of the increasing current associated to the temperature dependence of the Ge band gap. The rms noise increased as well, owing to the drift of the amplifier offset voltage, acting as a small bias applied to the photodiode and thereby generating a dark current. The finer (19-21 °C) measurements (inset) demonstrated that the correct operation of the power monitors can be achieved with a coarse temperature control and a $\pm 1°C$ accuracy.
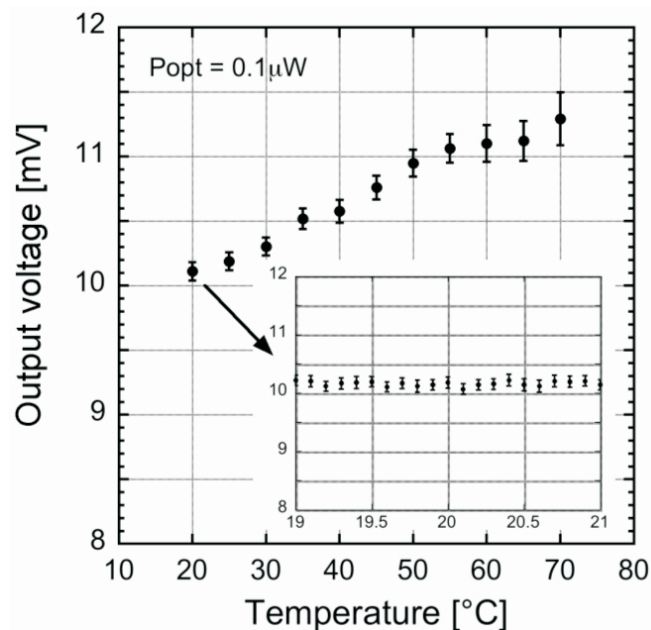
Figure 4.29: Power monitor performance versus temperature - Temperature dependence of the measured optical power (0.1 μW). The inset shows a fine measurement around 20°C

In conclusion, WPD1 were integrated on optical chips and equipped with a transimpedance amplifier to demonstrate power monitor operation. The integrated system exhibited a good sensitivity of 10 nW as well as an excellent linearity with and without bias. The marginal temperature dependence, low noise and small error make these monitors quite appealing for WDM photonic integrated circuits with several channels and ports.

4.5 Conclusions

The evaporated Ge-on-Si technology was investigated to demonstrate monolithic integration of NIR photodetctors with Si-based optical chips. Exploiting distributed light absorption in waveguiding structures, it is possible to improve evaporated Ge-on-Si detection properties. I reported on near infrared waveguide photodetectors fabricated on SOI substrates exhibiting peak responsivities of 1 A/W at 1.55 μm, with typical values above of 0.2 A/W and current densities below 4 mA/cm^2. Encouraged by these promising performance we integrated the WPD on SOI optical chips provided with waveguides, bends and tapers. Despite some technological problems, the detectors exhibit promising performance for the integration with silicon-based optical circuits and silicon electronics. This was demonstrated by the fabrication of power monitors monolithically integrated on SOI optical chips with good sensitivity of 10nW. Future developments concern the optimization of the fabrication process and the realization of integrated communication photodetectors by means of improved Ge crystalline quality and local doping of Si.

5

Conclusions

I investigated the approach of thermal evaporation to fabricate Ge-on-Si heterojunction devices towards NIR photodetectors. I performed Ge evaporation on Si and characterized the thin films in terms of both structural and electrical properties versus growth parameters. I demonstrated that Si temperature drastically affects the crystalline quality of Ge thin films, with best results in the range $300-400°C$. Ge evaporated at $300°C$ is epitaxial and its mono-crystalline structure is affected by high threading dislocation densities according to the large lattice mismatch between Si and Ge. The homogeneous defect distribution causes an unintentional high p-type doping ($10^{17} \div 10^{18}$ cm^{-3}) and a corresponding low mobility (≈ 80 cm^2/Vs) with an equivalent resistivity of $0.2\ \Omega/cm$. The results obtained by material characterization are of paramount importance as they allow developing models suitable for device design.

I also investigated conduction and NIR detection properties of evaporated Ge-on-Si heterojunctions. The results demonstrated a trap-assisted conduction mechanism explained by the energy band pinning at the Ge/Si interface. The high doping together with the short diffusion length limit the detection properties of normal incidence devices. Improvements can be achieved by employing waveguide detector (WPD) geometries. WPD exhibit promising performance approaching results obtained with sophisticated deposition techniques, i.e. typical responsivities exceeding $0.2\ A/W$ at $1.55\ \mu m$ at $1\ V$ reverse bias.

Finally, I studied monolithic integration of evaporated Ge devices on Si chips, demonstrating NIR Ge-on-Si power monitors monolithically integrated on SOI chips. The integrated systems exhibit a sensitivity of $10\ nW$ with good linearity over about

four orders of magnitude.

The results of this work encourage further studies of this approach. The process simplicity and the low temperature involved make this technique a real candidate for integration with standard CMOS process flows. Future perspective include intentional modulation of carrier type and conductivity.

6

List of Publications

Journal papers

L. Colace, V. Sorianello, M. Balbi and G. Assanto, **Germanium near infrared detector on Silicon-on-Insulator**, Appl. Phys. Lett. **91**, 021107 (2007)

L. Colace, M. Balbi, V. Sorianello, G. Assanto, **Temperature-dependence of Ge on Si p-i-n photodetectors**, J. Lightwave Techn. **26**, 2211-2214 (2008)

V. Sorianello, A. Perna, L. Colace, G. Assanto, H. C. Luan and L. C. Kimerling, **Near-infrared absorption of Germanium thin films on Silicon**, Appl. Phys. Lett. **93**, 111115 (2008)

M. Balbi, V. Sorianello, L. Colace and G. Assanto, **Analysis of Temperature-dependence of Ge on Si p-i-n photodetectors**, Physica E **41**, 1086-1089 (2009)

V. Sorianello, M. Balbi, L. Colace and G. Assanto, **Guided-wave photodetectors in Germanium on SOI optical chips**, Physica E **41**, 1090-1093 (2009)

V. Sorianello, M. Balbi, L. Colace, G. Assanto, L. Socci and M. Romagnoli, **Guided-wave photodetectors in Germanium on optical chips in Silicon-On-Insulator**, J. Europ. Opt. Soc. Rap. Publ. **4**, 09030 (2009)

L. Colace, V. Sorianello, A. De Iacovo, D. Fulgoni, J. Nash and G. Assanto, **Germanium-on-glass near-infrared detectors**, Electron. Lett. **45**, 994 (2009)

V. Sorianello, A. De Iacovo, L. Colace, G. Assanto, D. Fulgoni, L. Nash and M. Palmer, **Germanium on insulator near-infrared photodetectors fabricated by layer transfer**, Thin Solid Films **518**, 2501 (2010)

L. Colace, V. Sorianello, M. Romagnoli and G. Assanto, **Near-Infrared Ge-on-Si power monitors monolithically integrated on SOI chips**, Photon. Techn. Lett., in press

Conference papers

L. Colace, V. Sorianello, M. Balbi, G. Assanto, **Fotorivelatori in guida realizzati in germanio su silicio**, 10° Convegno Nazionale FOTONICA 2007, Rome (Italy), June 2007, Conference Proceedings p.103

L. Colace, M. Balbi, P. Ferrara, V. Sorianello, G. Assanto, **Ge-on-Si photodetectors for optical receivers**, Proc. of 11th International Symposium on Microwave and Optical Technology, Monte Porzio Catone (Italy) December 2007

V. Sorianello, M. Balbi, L. Colace, G. Assanto, **Guided-wave photodetectors in Germanium on SOI optical chips**, Europ. MRS Meeting, Strasbourg (France), May 2008

M. Balbi, V. Sorianello, L. Colace, G. Assanto, **Analysis of Temperature-dependence of Ge on Si p-i-n photodetectors**, Europ. MRS Meeting, Strasbourg (France), May 2008

V. Sorianello, M. Balbi, L. Colace, G. Assanto, **Fotorivelatori in germanio integrati su chip ottici SOI**, 10° Convegno Nazionale Elettroottica 2008, Milan (Italy), June 2008, Conference Proceedings p.97

V. Sorianello, M. Balbi, L. Colace, G. Assanto, G. Mutinati, S. Sardo, L. Socci and M. Romagnoli, **Guided-wave photodetectors in Germanium on SOI optical chips**, First Mediterranean Photonics Conference, Ischia (Italy), June 2008

V. Sorianello, A. Perna, L. Colace, G. Assanto, H. C. Luan and L. C. Kimerling, **Measurement of the Near Infrared Absorption of Ge on Si Films by Differential Spectroscopy**, The 5th Annual Conference on Group IV Photonics, Sorrento (Italy), September 2008

V. Sorianello, L. Colace, G. Assanto, D. Fulgoni and J. Nash, **Germanium solar cells by layer transfer**, Europ. MRS Meeting, Strasbourg (France), June 2009

V. Sorianello, L. Colace, G. Assanto, D. Fulgoni and J. Nash, **Germanium on insulator near infrared photodetectors fabricated by layer transfer**, Europ. MRS Meeting, Strasbourg (France) June 2009

References

[1] S. Donati. *Photodetectors: Devices, Circuits and Applications*. Prentice Hall PTR, first edition, 1999.

[2] S. M. Sze. *Physics of Semiconductor Devices*. Wiley, third edition, 2006.

[3] R. A. Soref. Silicon based optoelectronics. *Proc. IEEE*, 81:1687, 1993.

[4] G. Masini, L. Colace, and G. Assanto. Germanium thin films on Silicon for detection of near-infrared light. In *Handbook of Thin Film Materials*, volume 4, chapter 7. Academic Press, 2001.

[5] G. Masini, L. Colace, and G. Assanto. Si-based optoelectronics for communications. *Mater. Sci. Eng. B*, 89:2, 2002.

[6] H. C. Luan, D. R. Lim, K. K. Lee, K. M. Chen, J. G. Sandland, K. Wada, and L. C. Kimerling. High-quality Ge epilayers on Si with low threading-dislocation densities. *Appl. Phys. Lett.*, 75:2909, 1999.

[7] L. Colace, G. Masini, G. Assanto, H. C. Luan, K. Wada, and L. C. Kimerling. Efficient high-speed near-infrared Ge photodetectors integrated on Si substrates. *Appl. Phys. Lett.*, 76:1231, 2000.

[8] S. Famá, L. Colace, G. Masini, G. Assanto, and H. C. Luan. High performance germanium-on-silicon detectors for optical communications. *Appl. Phys. Lett.*, 81:586, 2002.

[9] I. Dosunmu, D. D. Cannon, M. K. Emsley, L. C. Kimerling, and M. S. Unlu. High-speed resonant cavity enhanced Ge photodetectors on reflecting Si substrates for 1550-nm operation. *IEEE Photon. Technol. Lett.*, 17:175, 2005.

[10] M. Jutzi, M. Berroth, G. Whol, M. Oheme, and E. Kasper. Ge-on-Si vertical incidence photodiodes with 39-GHz bandwidth. *IEEE Photon. Technol. Lett.*, 17:1510, 2005.

[11] M. Berroth, M. Kaschel, E. Kasper, S. Klinger, and M. Oheme. Ge on Si p-i-n photodiodes with a 3 dB bandwidth of 49 GHz. *IEEE Photon. Technol. Lett.*, 21:920, 2009.

[12] T. Yin, R. Cohen, M. M. Morse, G. Sarid, Y. Chetrit, D. Rubin, and M. J. Paniccia. 31 GHz Ge n-i-p waveguide photodetectors on Silicon-On-Insulator substrate. *Opt. Express*, 15:13965, 2007.

[13] Y. Kang, M. Morse H. Liu, M. J. Paniccia, M. Zadka, S. Litski, G. Sarid, A. Pauchard, Y. Kuo, H. Chen, W. S. Zaoui, J. E. Bowers, A. Beling, D. C. McIntosh, X. Zheng, and J. C. Campbell. Monolithic Germanium/Silicon avalanche photodiodes with 340 GHz gain-bandwidth product. *Nat. Photon.*, 3:59, 2008.

[14] E. Kasper, H. J. Herzog, and H. Kibbel. One-Dimensional SiGe superlattice grown by UHV epitaxy. *Appl. Phys.*, 8:199, 1975.

[15] R. Potter. In *Handbook of Optical Constant of Solids*. Academic Press, 1985.

[16] R. Braunstein, A. R. Moore, , and F. Herman. Intrinsic optical absorption in Germanium-Silicon alloys. *Phys. Rev.*, 109:695, 1958.

[17] K. Ito and K. Takahashi. Epitaxial growth of Ge layers on Si substrates by vacuum evaporation. *Jpn. J. Appl. Phys.*, 7:821, 1968.

[18] B. Y. Tsaur, J. C. C. Fan, and R. P. Gale. Solid-phase heteroepitaxy of Ge on (100) Si. *Appl. Phys. Lett.*, 38:176, 1981.

[19] B. Y. Tsaur, M. W. Geis, J. C. C. Fan, and R. P. Gale. Heteroepitaxy of vacuum-evaporated Ge films on single-crystal Si. *Appl. Phys. Lett.*, 38:779, 1981.

[20] T. F. Kuech and M. Maenpaa. Epitaxial growth of Ge on (100) Si by a simple chemical vapor deposition technique. *Appl. Phys. Lett.*, 39:245, 1981.

[21] M. Maenpaa, T. F. Kuech, M. A. Nicolet, and D. K. Sadana. The heteroepitaxy of Ge on Si: A comparison of chemical vapor and vacuum deposited layers. *J. Appl. Phys.*, 53:1076, 1982.

[22] R. People. Physics and applications of Ge_xSi_{1-x}/Si strained-layer heterostructures. *IEEE J. Quantum Electron.*, 22:1696, 1986.

[23] J. M. Baribeau, T. E. Jackman, D. C. Houghton, P. Maigne, and M. W. Denhoff. Growth and characterization of $Si_{1-x}Ge_x$ and Ge epilayers on (100) Si. *J. Appl. Phys.*, 63:5736, 1988.

[24] B. Cunningham, J. O. Chu, and S. Akbar. Heteroepitaxial growth of Ge on (100) Si by ultrahigh vacuum, chemical vapor deposition. *Appl. Phys. Lett.*, 59:3574, 1991.

[25] M. T. Currie, S. B. Samavedam, T. A. Langdo, C. W. Leitz, and E. A. Fitzgerald. Controlling threading dislocation densities in Ge on Si using graded SiGe layers and chemical-mechanical polishing. *Appl. Phys. Lett.*, 72:1718, 1998.

[26] L. Colace, G. Assanto, D. Fulgoni, and L. Nash. Near-infrared p-i-n Ge-on-Si photodiodes for silicon integrated receivers. *J. Lightwave Technol.*, 26:2954, 2008.

[27] V. A. Shah, A. Dobbie, M. Myronov, D. J. F. Fulgoni, L. J. Nash, and D. R. Leadley. Reverse graded relaxed buffers for high Ge content SiGe virtual substrates. *Appl. Phys. Lett.*, 93:192103, 2008.

[28] J. L. Liu, Z. Yang, and K. L. Wang. Sb surfactant-mediated SiGe graded layers for Ge photodiodes integrated on Si. *J. Appl. Phys.*, 99:24506, 2006.

[29] G. Masini, V. Cencelli, L. Colace, F. De Notaristefani, and G. Assanto. Monolithic integration of near-infrared Ge photodetectors with Si complementary metal-oxide-semiconductor readout electronics. *Appl. Phys. Lett.*, 80:3268, 2002.

[30] G. Masini, G. Capellini, J. Witzen, and C. Gunn. A 1550nm, 10Gb/s monolithic optical receiver in 130nm CMOS with integrated Ge waveguide photodetector. *IEEE Intl. Conf. Group IV Photonics*, page 1, 2007.

[31] M. Ohring. *Materials Science Of Thin Films: Deposition And Structure*. Academic Press, second edition, 2001.

[32] M. Faraday. The Bakerian Lecture: Experimental relations of Gold (and other metals) to light. *Phil. Trans.*, 147:145, 1857.

[33] M. Garozzo, G. Conte, F. Evangelisti, and G. Vitali. Heteroepitaxial growth of Ge on (111) Si by vacuum evaporation. *Appl. Phys. Lett.*, 41:1070, 1982.

[34] F. Evangelisti, M. Garozzo, and G. Conte. Structure of vapor-deposited Ge films as a function of substrate temperature. *J. Appl. Phys.*, 53:7390, 1982.

[35] L. Colace, G. Masini, F. Galluzzi, and G. Assanto. *Proc. of the MRS Fall Meeting*, 1998.

[36] G. Masini, L. Colace, , and G. Assanto. 2.5 Gb/s polycrystalline Germanium-on-Silicon photodetector operating from 1.3 to 1.55 μm. *Appl. Phys. Lett.*, 82:15, 2003.

[37] G. Masini, V. Cencelli, L. Colace, F. DeNotaristefani, and G. Assanto. Linear array of Si/Ge heterojunction photodetectors monolithically integrated with Silicon CMOS readout electronics. *IEEE J. Sel. Topics Quantum Electron.*, 10:811, 2004.

[38] L. Colace, G. Masini, and G. Assanto. Guided-wave near-infrared detector in polycrystalline Germanium on Silicon. *Appl. Phys. Lett.*, 87:203507, 2005.

[39] L. Colace, G. Masini, G. Assanto, F. DeNotaristefani, and V. Cencelli. Near-infrared camera in polycrystalline Germanium integrated on complimentary-metal-oxide-semiconductor electronics. *Appl. Phys. Lett.*, 90:11103, 2007.

[40] W. Kern. *Handbook of semiconductor wafer cleaning technology: science, technology and applications*. First edition, 1993.

[41] E. Yablonovitch, D. L. Allara, C. C. Chang, T. Gmitter, and T. B. Brigth. Mechanism of HF etching of Silicon surfaces: a theoretical understanding of Hydrogen passivation. *Phys. Rev. Lett.*, 57:249, 1986.

[42] G. W. Trucks, K. Raghavachari, G. S. Higashi, and Y. J. Chabal. Mechanism of HF etching of Silicon surfaces: a theoretical understanding of Hydrogen passivation. *Phys. Rev. Lett.*, 65:504, 1990.

[43] M. J. Pelletier. *Analytical applications of Raman spectroscopy*. Blackwall Science, first edition, 1999.

[44] W. H. Weber and R. Merlin. *Raman scattering in materials science*. Springer, 2000.

[45] I. H. Campbell and P. M. Fauchet. The effect of microcrystal size and shape on the phonon Raman spectra of crystalline semiconductors. *Solid State Comm.*, 58:739, 1986.

[46] J. H. Parker Jr., D. W. Feldman, and M. Ashkin. Raman scattering by Silicon and Germanium. *Phys. Rev.*, 155:712, 1967.

[47] J. Menendez and M. Cardona. Temperature dependence of the first-order Raman scattering by phonons in Si, Ge, and α-Sn: anharmonic effects. *Phys. Rev. B*, 29:2051, 1984.

[48] I.H. Campbell, P.M. Fauchet, E.H. Lee, and M.A. Awal. Raman microprobe study of silicon- and germanium- on-insulator structures. *Thin Solid Films*, 154:249, 1987.

[49] B. E. Warren. *X-Ray diffraction*. Addison-Wesley, first edition, 1990.

[50] C. R. Brundle, C. A. Evans, and S. Wilson. *Encyclopedia of materials characterization*. First edition, 1992.

[51] D. K. Schroder. *Semiconductor material and device characterization*. Wiley, third edition, 2006.

[52] W. J. Bartels. Characterization of thin layers on perfect crystals with a multipurpose high resolution x-ray diffractometer. *J. Vac. Sci. Technol. B*, 2:338, 1983.

[53] H. H. Berger. Models for contacts to planar devices. *Solid-State Electron.*, 15:145, 1972.

[54] E. H. Hall. On a new action of the magnet on elctric currents. *Amer. J. Math.*, 2:287, 1879.

[55] P. Blood and J. W. Orton. *The electrical characterization of semiconductors: majority carriers and electron states.* Academic Press, first edition, 1992.

[56] B. L. Sharma and R. K. Purohit. *Semiconductor heterojunctions.* Pergamon Press, first edition, 1974.

[57] R. L. Anderson. Experiments on Ge-GaAs heterojunctions. *Solid State Electron.*, 5:341, 1962.

[58] P. Durupt, J. Raynaud, and G. Mesnard. Heterojonctions ge p-si n obtenues par pitaxie sous vide. *Solid-State Electronics*, 12:469, 1969.

[59] S. S. Perlman and D. L. Feucht. *p-n* heterojunctions. *Solid State Electron.*, 7:911, 1964.

[60] R. H. Rediker, S. Stopek, and J. H. R. Ward. Interface-alloy epitaxial heterojunctions. *Solid State Electron.*, 7:621, 1964.

[61] J. P. Donnelly and A. G. Milnes. Current/voltage characteristics of p-n Ge-Si and Ge-GaAs heterojunctions. *Proc. IEEE*, 113:1468, 1966.

[62] L. Colace, P. Ferrara, and G. Assanto. Low dark-current Germanium-on-Silicon near-infrared detectors. *IEEE Photo. Tech. Lett.*, 19:1813, 2007.

[63] L. M. Giovane, H. C. Luan, A. M. Agarwal, and L. C. Kimerling. Correlation between leakage current density and threading dislocation density in SiGe p-i-n diodes grown on relaxed graded buffer layers. *Appl. Phys. Lett.*, 78:541, 2001.

[64] V. Sorianello, A. Perna, L. Colace, G. Assanto, H. C. Luan, and L. C. Kimerling. Near-infrared absorption of germanium thin films on silicon. *Appl. Phys. Lett.*, 93:111115, 2008.

[65] D. Ahn, C. Hong, J. Liu, W. Giziewicz, M. Beals, L. C. Kimerling, J. Michel, J. Chen, and F. X. Kartner. High performance, waveguide integrated ge photodetectors. *Opt. Express*, 15:3916, 2007.